Spring 2018

Atomic Structure Studies of 2D Materials and Advancement of Dynamical LEEM/uLEED-IV Analysis

Zhongwei Dai
University of New Hampshire, Durham

Recommended Citation

Dai, Zhongwei, "Atomic Structure Studies of 2D Materials and Advancement of Dynamical LEEM/uLEED-IV Analysis" (2018). *Doctoral Dissertations*. 2404.
https://scholars.unh.edu/dissertation/2404

ATOMIC STRUCTURE STUDIES OF 2D MATERIALS AND ADVANCEMENT OF DYNAMICAL LEEM/μLEED-IV ANALYSIS

BY

ZHONGWEI DAI

B.S. in Physics, Wuhan University, 2010

DISSERTATION

Submitted to the University of New Hampshire
in partial fulfillment of
the requirements for the degree of

Doctor of Philosophy

in

Physics

May, 2018

This dissertation has been examined and approved in partial fulfillment of the requirements for the degree of Doctor of Philosophy in Physics by:

Dissertation Director, Karsten Pohl
Professor of Physics

Olof Echt
Professor of Physics

Kai Germaschewski
Associate Professor of Physics

Shawna Hollen
Assistant Professor of Physics

Jiadong Zang
Assistant Professor of Physics

On April 19, 2018

Original approval signatures are on file with the University of New Hampshire Graduate School.

DEDICATION

To my parents and my family.

ACKNOWLEDGMENTS

There are numerous people who offered their help through my journey to becoming a doctor in physics. Without their help, this work would not have been possible. Hereby I would like to express my sincere gratitude to all of them.

First and foremost, I would like to thank my advisor, Professor Karsten Pohl, for his guidance and support. His critique scientific virtue inspired and motivated me to complete rigorous research work. His advising style gave me freedom to explore in the physics world and grow as a scientist. His generous support helped me to build collaborations with other renowned research groups.

I thank Dr. Wencan Jin for his invaluable contributions to various projects we worked on together. He was a fellow graduate student at Prof. Richard M. Osgood Jr.'s research group in Columbia University, when we started collaborating. I also want to thank him for introducing me to his collaboration network, which made a few more projects possible after the success of our first collaborated work on MoS_2. Wencan conducted all the ARPES measurements mentioned in this thesis and he helped to prepare most of the samples used in this thesis. He also helped to collect most of the LEEM/μLEED data used in this thesis.

I would like to thank Prof. Richard M. Osgood Jr., from Columbia University. His encouragement and applause of my research work have greatly helped me to build confidence as a researcher. His recognition kept me going in the darkest hours in my PhD journey.

I thank Dr. Jerzy (Jurek) Sadowski from Brookhaven National Lab (BNL). Thanks to him, I was able to use the state-of-art facilities in BNL for my research. Most of the LEEM/μLEED experiments were conducted with his full support and guidance. His unconditional support is highly appreciated.

I thank Dr. Jie-Xiang Yu and his advisor Prof. Jiadong Zang, at UNH, for their excellent theoretical contributions in our collaborated work.

I want to thank all the research groups who generously supplied the samples. Prof. James Hone's group from Columbia University supplied the MoS_2 and black phosphorus samples. Prof. Huili Xing's group from Cornell University supplied the MBE-grown SnSe and $SnSe_2$ samples. Prof. Luis Balicas' group from Florida State University supplied the tungsten doped $MoTe_2$ samples.

There are a lot of friends, colleagues and professors here at UNH I would like to thank. I thank my lab colleague and friend, Dr. Maxwell Grady for help in extracting some of the experimental LEED-IV data. I want to thank my former office-mate and friend, Dr. John McClain, for discussions about physics and many other fun topics. I thank Kris Maynard for his generous help in coding and debugging. I thank my friends, Fathima Muzamil, Nick Lajoie and Ben MacDonald for their friendship and good times. I thank Prof. Kai Germaschewski for help in writing the calculation package described in this thesis.

I thank the financial support from the National Science Foundation, under the grant number NSF DMR 1006863. And I thank the UNH graduate school travel grant for supporting my trips to conferences.

Finally, my deepest appreciation goes to my mom, Zai-Xiu Sun and my dad, Zai-Bin Dai for raising me up. We had no money growing up, but they worked almost seven days a week and they successfully sent three of their kids to college. I thank my sisters for their full support through my college and PhD years.

TABLE OF CONTENTS

List of Tables

List of Figures

ABSTRACT

Atomic Structure Studies of 2D Materials and Advancement of Dynamical LEEM/μLEED-IV Analysis

by

Zhongwei Dai

University of New Hampshire, May, 2018

Two-dimensional (2D) materials have attracted much attention as an emerging group of materials over the past decade due to their novel mechanical, optical and electronic properties with many potential applications in photovoltaics, photo-catalysts, and modern electronics. However, the detailed atomic structural information has been rarely experimentally investigated due to the following difficulties: (i) the limited sample size of 2D materials prepared through mechanical exfoliation of a few μm, and (ii) the easy oxidation and surface instability of various 2D materials under high energy probing techniques. Selected area low-energy electron diffraction analysis (μLEED-IV) performed in a low-energy electron microscopy (LEEM) system, is a modern surface sensitive and non-intrusive surface characterization technique, which has the advantage of μm sampling size selectivity. I present, for the first time, detailed experimental characterizations of atomic crystal structures of a series of technologically promising 2D materials: MoS_2, black phosphorus (BP), the topological crystalline insulator (TCI) SnSe, 1T phase $SnSe_2$ and tungsten doped $MoTe_2$. I have found a slight asymmetry of the relaxation of the interlayer spacing of a suspended single S-Mo-S sandwich layer, which is most likely caused by a small amount of warping or strain. To my knowledge, this is the first atomic crystal structure characterization of the single layer form of a 2D material. In the case of both bulk BP and exfoliated few layer phosphorene (FLP), with a thickness of about 10 nm, I have found that the surface undergoes a significant dis-

tortion in the form of buckling of 0.2 Å, an order of magnitude larger than two previously reported theoretical values. Using first-principles calculations, my collaborators and I are proposing a vacancy defect driven mechanism as cause of this surface distortion. Vacancy defects are also found to be not only the origin of a previously reported impurity state within the monolayer phosphorene bandgap, but also very likely the origin of the previously reported intrinsic p-type behavior of phosphorene materials. The topological properties of the rock-salt TCI SnSe are strongly related to its surface structure. The Sn-terminated surface and Se-terminated surface have been previously shown to have distinctively different electronic properties. Using μLEED-IV, I have shown that our SnSe (111) thin films have a Sn-terminated surface without surface reconstruction. Furthermore, I have revealed an oscillatory, contraction-expansion-contraction pattern for the structural relaxation in the top few layers of SnSe. I have found that the 1T $SnSe_2$ thin film surface is similar to other 2D materials and it remains mostly like the bulk crystal structure while undergoing slight surface relaxation. Using μLEED-IV, I have also confirmed the phase transition in the W-doped $MoTe_2$. I show that μLEED-IV in a high spatial resolution LEEM system is a powerful tool for study of atomic crystal structure of 2D materials. I believe the detailed surface structural information is of fundamental importance and provides crucial input for better understanding of the intriguing electronic properties of various 2D materials and a more solid guidance for engineering 2D materials based devices.

CHAPTER 1

INTRODUCTION

1.1 Brief history of 2D materials

The intensive interest in two-dimensional (2D) materials was ignited by one of the most common materials in daily life, graphite, which is the main component of pencils. Graphite has a layered honeycomb structure with individual atomic layers bonded by weak van der Waals (vdW) forces, depicted in Fig. 1-1. As Richard P. Feyman said, 'There's plenty of room at the bottom. [7]' Theorists predicted that if graphite is thinned down to monolayer, denoted as graphene, novel quantum properties and rich physics could be observed and manipulated for intriguing applications in numerous types of electronics and optronics [8, 1]. But many scientists, such as, Landau and Peierls, believed that materials would not stay stable in such an atomically thin form at finite temperature [9, 10]. The argument was later extended by Mermin and is strongly supported by various experimental observations [11]. The graphene sheet was expected to either curl up or get wrinkled due to thermal and surface strain effects. However, this does not stop curious physicists' attempts to defy the impossible. Countless efforts have been made to achieve single-layer graphene, including chemical exfoliation [12], epitaxial growth of graphene on metal substrate [13, 14] and thermal decomposition of SiC [15, 16]. None were successful until 2003, when Geim and Novoselov spotted a piece of used scotch tape in the trash bin [17]. Scotch tape was

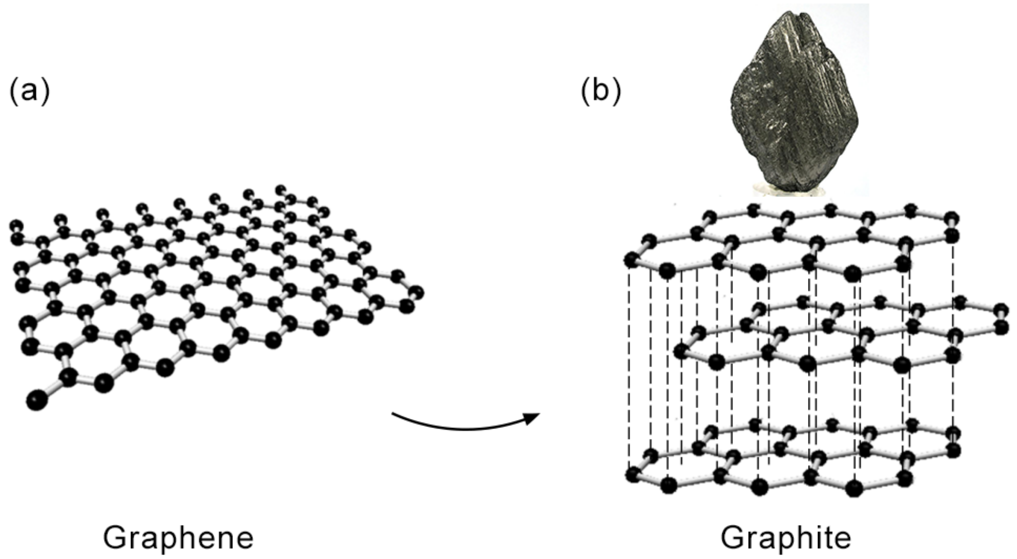

Figure 1-1: (a) Single layer of graphene; (b) stacking of layers of graphene sheets forms bulk graphite. Natural appearance of graphite shown on the top in (b).

commonly used to exfoliate graphite in order to get a clean graphite surface for scanning tunneling microscopy (STM) calibration. When Geim spotted the scotch tape with graphite residue, some of which looked transparent and thin, an idea came to his mind. Could it be very thin layers of crystalline graphite? And could we repeat peeling off one scotch tape from another to thin down the graphite to even single atomic layer form? After months of trials, Geim and his group indeed successfully realized the isolation of single-layer graphene using this so called 'scotch-tape method'. Their work was published in Science [18] in 2004 and won Geim and Novoselov the Nobel Prize in 2010, 'for their groudbreaking experiments regarding the two-dimensional material graphene'.

The success in graphene triggered tremendous interests in this newly discovered material form as well as opened research for a new whole category of two-dimensional (2D) materials. A 2D material is defined as a material in which the atomic organization and bond strength along two dimensions are similar and much stronger than along a third dimension [19]. In the past decade, following the success of graphene research, other layered materials were explored for their 2D form, such as transition metal dichalchogenides (TMDs, MX_2, most commonly, M=Mo, W, X=S, Te, Se); elemental layered materials such as black phosphorus and its monolayer form, phosphorene; and other potential elemental 2D materials such as silicene, germanene, brophene. The study of properties and potential novel applications of heterostructure materials that consist of layers of different 2D materials stacked together is on the rise too.

1.2 Why study 2D materials

Graphene, as the first discovered 2D material, has attracted the most attention since its first isolation in 2004. Graphene consists of a single atomic layer of carbon atoms bonded in the honeycomb structure, as shown in Fig. 1-1(a). The sp^2 hybridization in graphene between s orbitals and p_x and p_y orbitals leads to a trigonal planar structure. The $pp\pi$ bonding/antibonding states of p_z orbitals in this unique structure gives rise to its peculiar electronic structures, as shown in Fig. 1-2 [1]. The electrons in graphene behave like massless Dirac fermions. The bands disperse linearly at K and K' points in reciprocal space, which leads to very high carrier mobility in graphene [20]. Also due to the special honeycomb structure, the bonds between atoms are very strong and free of defects in regions of up to hundreds of square nanometers [21]. Graphene sheets are very flexible and can be stretched up to 20% without significant crystal structure deformation. Graphene is not only the thinnest but also the strongest material [22]. Composite materials utilizing graphene are super strong, thin and lightweight [23]. These types of composite materials are highly desired for use in satellite, airplane and automobile manufacturing. Graphene is also impermeable to gases, which makes it useful in sensors for air pollution [24] and biomedical applications [25]. Graphene is transparent and conductive at the same time, so it can be used as transparent electrodes in solar cells [26, 27], high-efficiency batteries [28, 29] and flexible electronic displays [30]. These amazing properties and potential applications of

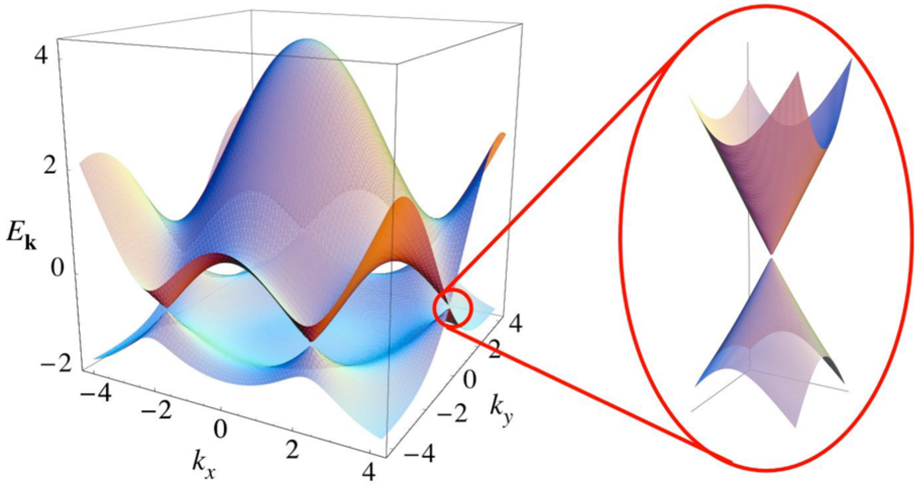

Figure 1-2: Band structure of graphene [1].

graphene make it a true ‘wonder’ material.

Even though graphene has numerous foreseeable intriguing applications, the zero bandgap is one of the major issues that hinders its further advancement in the semiconductor industry [1]. In order to overcome this issue, other 2D materials such as TMDs (MX_2, M=Mo, W, Sn; X=S, Te, Se) and black phosphorus (BP) have been explored and studied extensively in the past decade. In contrast to graphene, TMDs and BP have non-zero bandgaps that can be utilized in various applications in the semiconductor industry. One of the most studied TMDs is MoS_2. Similar to graphite, bulk MoS_2 layers are bonded by weak van der Waals forces, thus can be exfoliated into few-layer or single-layer form. When thinned down to monolayer, MoS_2 shows a dramatic transition from an indirect bandgap to a direct bandgap of about 1.8 eV. This direct bandgap can be utilized in logical electronic devices, such as field effect transistors (FETs). Transistors fabricated with single-layer MoS_2 have been reported to have high on/off ratio and much lower power consumption compared to classical Si-based transistors [31]. The large bandgap can also be utilized in photovoltaic devices for energy harvesting [32]. Ultrathin few-layer (3-5 layers) MoS_2 nanosheets have also been demonstrated to significantly improve the performance of photoelectrochemical

(PEC) solar cells, when used as photoanode [33].

Different from graphene or TMDs, BP has an intrinsically tunable, layer-dependent bandgap, ranging from 0.3 eV (bulk) to 2 eV (single-layer) [34]. This bandgap range bridges the energy gap between graphene and TMDs, thus presents the potential for various integrated devices on a single supporting platform. Promising applications of BP in modern electronics [35, 36, 37, 38] and photonics [39, 40] have been widely explored.

1.3 Thesis motivation

The electronic properties, optic properties, and potential applications of 2D materials have been studied extensively. However, one of the most fundamental properties, the experimental surface atomic structure has not been well understood. Most commonly, the surface structure was simply assumed to be the same as bulk, based on its van der Waals bonded layered structure. Density functional theory (DFT) was also commonly used as a theoretical approach to better understand or approximate the surface structure of 2D materials. But as any other theory, DFT has its limitations and sometimes may not present the realistic world well due to these limitations. The experimental input of the surface structure of 2D materials has been sparse, mostly due to the difficulty of measurement. Most of the recently studied 2D materials are prepared with the mechanical exfoliation method or the so called 'scotch-tape method', which are in a common sample size in the range of few μm. This provides very limited sampling area for characterization techniques. Furthermore, some of the 2D materials such as black phosphorus, are not structurally stable when facing elevated temperature treatment or high energy probing technique, such as the few 100 keV e-beam in transmission electron microscope (TEM). This requires that the probing technique to be non-destructive. A highly surface sensitive and non-destructive characterization technique with required sampling area as low as few μm is thus crucial and highly desirable for a more comprehensive understanding of the fundamental properties of 2D materials.

1.4 Content arrangement

One of the two main goals of this thesis work is to use the high surface sensitive and non-destructive micro-spot low energy electron diffraction (μLEED) in a high spatial resolution low energy electron microscopy (LEEM) system, combined with dynamical diffracted electron beam intensity *vs.* incident electron energy (LEED-IV) analysis to study the surface structure of various 2D materials with sub-Å resolution. Another goal of this thesis is the advancement of the traditional LEED-IV calculation programs including: angle resolved analysis for accuracy improvement and parallelization for high performance computing capability. In Chapter 2, I will describe the experimental techniques of LEEM and μLEED. In Chapter 3, I will introduce the multiple scattering theory in dynamical LEED-IV analysis and show my work of parallelization of the main calculation codes to enable high performance computing of the calculation package. In Chapter 4 and 5, I will present my published work on surface structures of MoS_2 [41] and black phosphorus [42]. In Chapter 6, I will present my published work on a topological crystalline insulator SnSe [43] and 1T phase $SnSe_2$. A publication is in preparation [44]. In Chapter 7, I will present my work on phase transition of 2H-$MoTe_2$ to T_d-$MoTe_2$ and their respective surface structures. A publication is in preparation [45]. In Chapter 8, I summarize the main results of this thesis and draw conclusions.

CHAPTER 2

EXPERIMENTAL TECHNIQUE: LEEM/μLEED-IV

2.1 Electron Diffraction

The wave-particle duality of matter was proposed by de Broglie in 1924 [46]. In his Nobel laureated work, de Broglie postulated that the wavelength λ of a particle with linear momentum p is given by the following equation 2.1, where h is Planck's constant.

$$\lambda = \frac{h}{p} \tag{2.1}$$

Electrons with kinetic energy of 100 eV correspond to a wavelength of approximately 1 Å. As a result, these electrons should diffract from a grating with a periodicity on the order of atomic dimensions, such as crystals. de Broglie's prediction was soon confirmed experimentally by Davisson and Germer in 1927, who observed the diffraction of low-energy electrons (tens of eV) from a nickel crystal [47, 48]. One month later, Thompson and Reid published their own experimental work of diffraction of high-energy electrons (tens of keV) from celluloid [49], which also revealed the wave nature of electrons. Davisson and Thompson shared the Nobel Prize for Physics in 1937, 'for their experimental discovery of the diffraction of electrons by crystals'. The discovery of electron diffraction by crystals set the foundation for low energy electron diffraction as a technique for surface crystal structure characterization.

2.1.1 Bravis Lattice and Reciprocal Space Lattice

The atoms in any crystalline solids are arranged in a periodic manner: atoms repeat themselves endlessly to form a macroscopic solid. In three dimensions, the different ways of periodic atom arrangement can be described using fourteen different types of Bravis Lattices, which can be categorized into seven distinct crystal types: triclinic, monoclinic, orthorhombic, tetragonal, rhombohedral, hexagonal, and cubic. Surfaces, interfaces of crystals, or the newly discovered 2D materials can be more easily described using 2D lattices. The periodic atom arrangement in two dimensions can be categorized by a total of five distinct types of 2D Bravis lattices: square, hexagonal, primitive rectangular, centered rectangular and oblique, as shown in Fig. 2-1. The atom positions in 2D can be described in the form

$$\vec{R} = n_1\vec{a}_1 + n_2\vec{a}_2, \tag{2.2}$$

where n_1 and n_2 are integers, and the vectors $\vec{a}_1$ and $\vec{a}_2$ are called the base vectors. Another concept that is associated with 2D bravis lattices is the unit cell in reciprocal space, which we shall see in the next section is extremely useful in LEED. The lattice bases, $\vec{b_i}$ in the reciprocal space is defined as:

$$\vec{b_i} \cdot \vec{a}_j = 2\pi\delta_{ij}. \tag{2.3}$$

Using the base vectors $\vec{b_i}$ defined in Eq. 2.3, we can construct the so called reciprocal space lattice, with lattice points defined as the following:

$$\vec{g}_{hk} = h \cdot \vec{b}_1 + k \cdot \vec{b}_2, \tag{2.4}$$

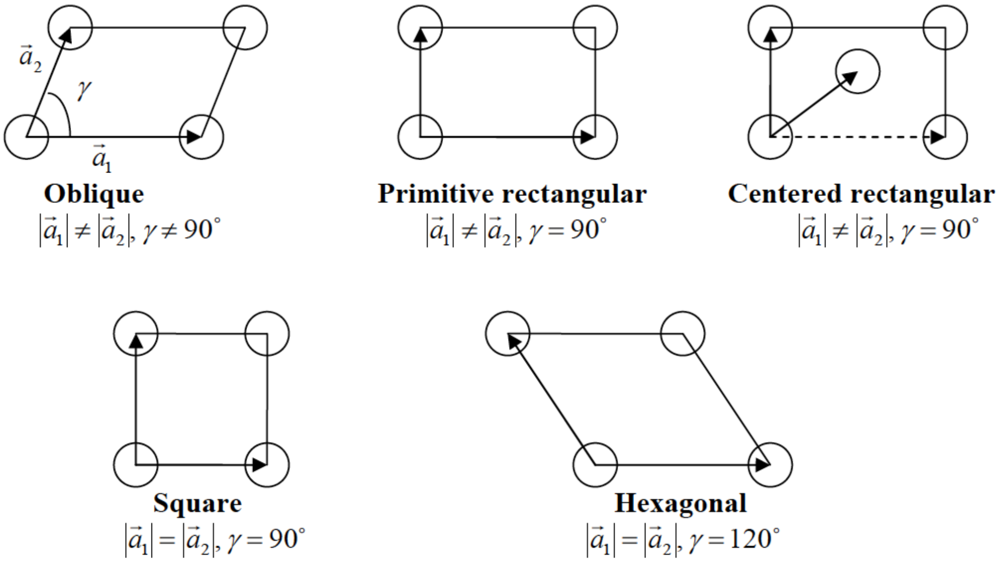

Figure 2-1: Unit cell of five types of 2D Bravis lattices. $\vec{a}_1$ and $\vec{a}_2$ are lattice vectors and γ is the angle between $\vec{a}_1$ and $\vec{a}_2$. Adopted from Ref. [2]

where h and k are integers, and (hk) are called the Miller indices.

2.1.2 Interpretation of Diffraction Pattern and Laue Equation

The principle of electron diffraction is analogous to that of X-ray diffraction. The angular dependence of the backscattered electrons can be explained using the Laue Equation:

$$\Delta\vec{K}^{||} = \vec{K_s}^{||} - \vec{K_i}^{||} = \vec{g}_{hk}, \tag{2.5}$$

where $\vec{K_s}^{||}$ and $\vec{K_i}^{||}$ are the surface-parallel components of the incident and scattering wave vector $\vec{K}_s$ and $\vec{K}_i$, respectively; $\vec{g}_{hk}$ is the vector of a surface reciprocal space lattice point (hk) defined in Eq. 2.4, and $\Delta\vec{K}^{||}$ is the surface-parallel component of the momentum transfer. The Laue diffraction condition can be conveniently visualized using an Ewald sphere, as shown in Fig. 2-2.

The Laue Equation was originally derived using the principle of constructive interference

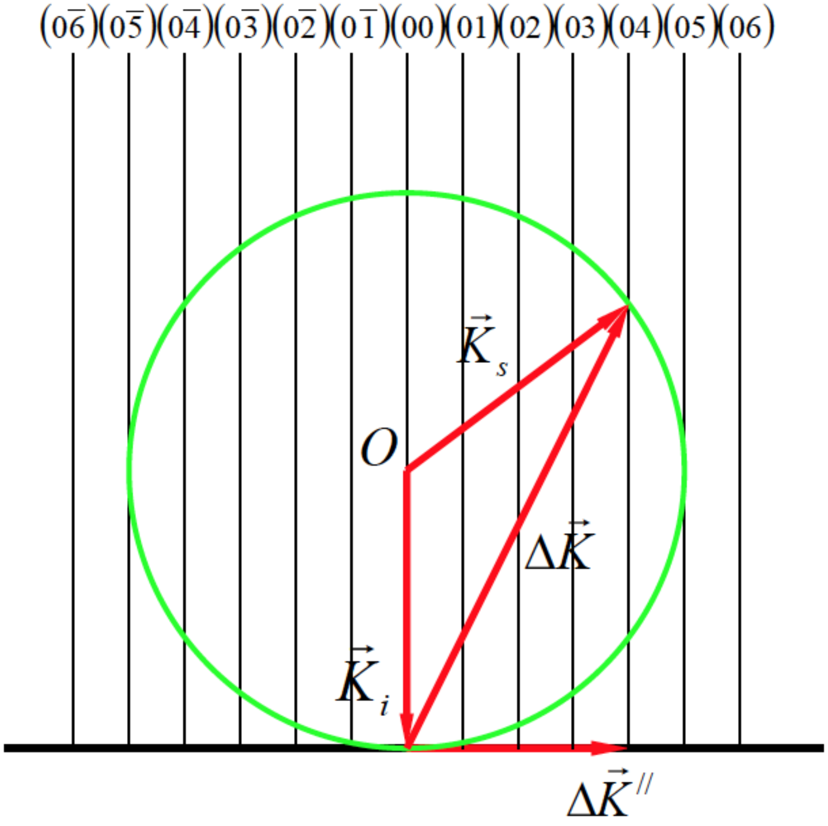

Figure 2-2: Ewald sphere for elastic electron diffraction from crystals. Indices (hk) of reciprocal space points are labeled on the top of the figure. The crossing points of the sphere and the diffraction rods indicate the relative position of the diffracted electron beam peak spots in the reciprocal space, *i.e.*, the diffraction spots.

of waves, which states that sharp peaks will be observed only in directions and at wavelengths for which the path difference between different rays of waves is an integral number of wavelengths.

$$\Delta d = n\lambda \tag{2.6}$$

In von Laue's approach, one regards the crystal as composed of identical microscopic objects (sets of ions or atoms), each of which are considered as scatterer of incident waves. We first consider just two scatterers, separated by a displacement vector $\vec{R}_{12}$, as shown in Fig. 2-3. We find that:

$$\Delta d = (\vec{R}_{12} \cdot \vec{K}_i - \vec{R}_{12} \cdot \vec{K}_s) \cdot \frac{\lambda}{2\pi} = n\lambda. \tag{2.7}$$

Thus we have,

$$\vec{R}_{12} \cdot (\vec{K}_i - \vec{K}_s) = n2\pi. \tag{2.8}$$

Comparing to the definition of the reciprocal space lattice vector $\vec{g}$, Eq. 2.4, we arrive at the Laue condition:

$$\Delta K = \vec{K}_s - \vec{K}_i = \vec{g}. \tag{2.9}$$

The Laue condition states that sharp diffraction peak will be observed when the momentum transfer between the scattered wave and the incident wave is a reciprocal lattice vector. In the 2D situation, the Laue condition reduces to Eq. 2.5.

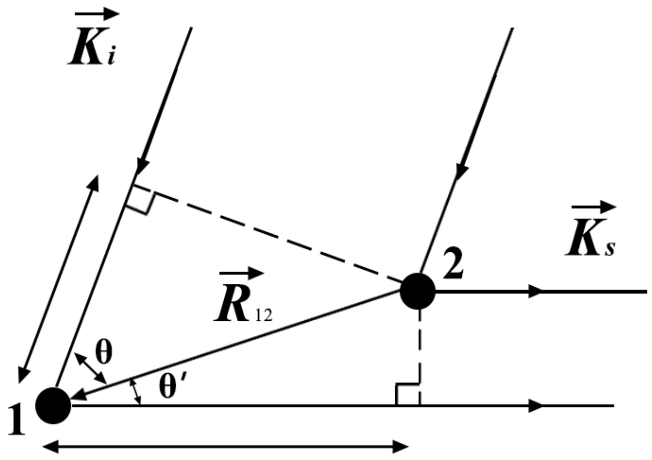

Figure 2-3: The scattering of waves by two atoms in crystal.

2.1.3 Relation to Bragg Law

If we use d as the distance between the successive planes that are perpendicular to $\Delta\vec{K}$, based on the definition of reciprocal space lattice vector we can derive:

$$\left|\Delta\vec{K}\right| = |\vec{g}| = \frac{2n\pi}{d}. \tag{2.10}$$

Let θ be the angle between the $\vec{K}_i$ and the reflection plane, geometry gives us:

$$\begin{aligned} \left|\Delta\vec{K}\right| &= 2\cdot\left|\vec{K}_i\right|\cdot\sin\theta = 2\cdot\left|\vec{K}_s\right|\cdot\sin\theta \\ &= 2\cdot\tfrac{2\pi}{\lambda}\cdot\sin\theta = \tfrac{2n\pi}{d} \end{aligned} \tag{2.11}$$

$$\Rightarrow 2d\cdot\sin\theta = n\lambda \tag{2.12}$$

Thus we have reduced the Laue equation 2.9 to the Bragg diffraction condition 2.12.

The Bragg diffraction condition considers only single scattering, which is not suitable for fully explaining the LEED process. A more sophisticated treatment of multiple scattering, which will be explained in the next chapter, is needed for fully understanding LEED process.

2.1.4 General Derivation of Laue Equation Using Schrödinger Equation

Here I show the same results given above can be derived in a more general fashion, based on the Schrödinger equation for the scattering of electrons by a surface. This has the advantage of not making any kinematic assumption (single scattering) and thereby proves the previous results are both general and of fundamental value for the case of multiple scattering in LEED as well.

The diffraction patterns are formed almost all by the elastically scattered electrons. The motions of these electrons should be determined by the Schrödinger equation of the time-independent form

$$-\frac{\hbar^2}{2m_e}\nabla^2\psi(\vec{r}) + V(\vec{r})\psi(\vec{r}) = E\psi(\vec{r}). \tag{2.13}$$

For convenience of calculation, atomic units in which

$$\hbar^2 = m_e = e^2 = 1, \tag{2.14}$$

will be used in the following derivations. Hartree will be used as the unit of energy,

$$1\ H = 27.2\ \text{eV}. \tag{2.15}$$

The unit for the length is Bohr radius,

$$1\ B.r.(\text{a.u.}) = 0.5292\ \text{Å}. \tag{2.16}$$

The Schrödinger equation then can be simplified to

$$-\frac{1}{2}\nabla^2\psi(\vec{r}) + V(\vec{r})\psi(\vec{r}) = E\psi(\vec{r}). \tag{2.17}$$

We assume the incident electrons are mono-energetic and the wave functions of the incident electron can be represented simply by the plane wave with wavevector $\vec{k}_0$,

$$\psi_i(\vec{r}) = A_0 \cdot \exp\Big(i\vec{k}_0 \cdot \vec{r}\Big), \tag{2.18}$$

where $|k_0| = (2mE)^{1/2}/\hbar$ and A_0 is a constant. And we can write the total wave function $\psi(\vec{r})$ as

$$\psi(\vec{r}) = \psi_i(\vec{r}) + \psi_s(\vec{r}). \tag{2.19}$$

Thus the Schrödinger equation for the total wave field can be written as:

$$-\frac{1}{2}\nabla^2[\psi_i(\vec{r}) + \psi_s(\vec{r})] + V(\vec{r})[\psi_i(\vec{r}) + \psi_s(\vec{r})] = E[\psi_i(\vec{r}) + \psi_s(\vec{r})]. \tag{2.20}$$

The surface has two-dimensional periodicity, *i.e.*,

$$\vec{r} = \vec{r'} + l\vec{a} + m\vec{b}. \tag{2.21}$$

Here, l and m are integers, $\vec{a}$ and $\vec{b}$ are the basis of the surface Bravis lattice. Since the potential $V(\vec{r})$ acting on the elcetron is due to the crystal, it should have the same translational symmetry,

$$V(\vec{r} + l\vec{a} + m\vec{b}) = V(\vec{r}). \tag{2.22}$$

The same argument can be applied to,

$$\nabla^2\psi = \frac{\partial^2\psi}{\partial x^2} + \frac{\partial^2\psi}{\partial y^2} + \frac{\partial^2\psi}{\partial z^2} = \frac{\partial^2\psi}{\partial x'^2} + \frac{\partial^2\psi}{\partial y'^2} + \frac{\partial^2\psi}{\partial z'^2} = \nabla'^2\psi. \tag{2.23}$$

Substitute equation (2.21) in $\psi_i(\vec{r})$, we can get,

$$\psi_i(\vec{r'} + l\vec{a} + m\vec{b}) = \psi_i(\vec{r'}) \cdot \exp\Big(il\vec{k}_0 \cdot \vec{a} + im\vec{k}_0 \cdot \vec{b}\Big). \tag{2.24}$$

Since $\vec{a}$ and $\vec{b}$ are in the plane parallel to the surface, we can reduce the above equation to,

$$\psi_i(\vec{r'} + l\vec{a} + m\vec{b}) = \psi_i(\vec{r'}) \cdot \exp\Big(il\vec{k}_{0\|} \cdot \vec{a} + im\vec{k}_{0\|} \cdot \vec{b}\Big), \tag{2.25}$$

where $\vec{k}_{0\|}$ denotes the component of $\vec{k_0}$ that is parallel to the surface. The amplitude of the scattered wave is always proportional to that of the incident wave, therefore the relationship between $\psi_s(\vec{r'} + l\vec{a} + m\vec{b})$ and $\psi_s(\vec{r'})$ must have the same form as equation (2.25),

$$\psi_s(\vec{r'} + l\vec{a} + m\vec{b}) = \psi_s(\vec{r'}) \exp\Big(il\vec{k}_{0\|} \cdot \vec{a} + im\vec{k}_{0\|} \cdot \vec{b}\Big). \tag{2.26}$$

We can assume that the scattered wave within the surface takes the form of a product of the incoming free electron plane wave, $\exp(i\vec{k}_{0\|})$, and a position dependent term $\chi_s(\vec{r})$,

$$\psi_s(\vec{r}) = \exp\Big(i\vec{k}_{0\|} \cdot \vec{r}_{\|}\Big)\chi_s(\vec{r}), \tag{2.27}$$

and substitute into equation (2.26),

$$\begin{aligned}\psi_s(\vec{r'}+l\vec{a}+m\vec{b}) &= \exp\Big[i\vec{k}_{0\|}\cdot(\vec{r'}_{\|}+l\vec{a}+m\vec{b})\Big]\cdot\chi_s(\vec{r'}+l\vec{a}+m\vec{b})\\ &= \exp\Big(il\vec{k}_{0\|}\cdot\vec{a}+im\vec{k}_{0\|}\cdot\vec{b}\Big)\cdot\exp\Big(i\vec{k}_{0\|}\cdot\vec{r'}_{\|}\Big)\cdot\chi_s(\vec{r'}+l\vec{a}+m\vec{b})\\ &= \exp\Big(i\vec{k}_{0\|}\cdot\vec{r'}_{\|}\Big)\cdot\chi_s(\vec{r'})\cdot\exp\Big(il\vec{k}_{0\|}\cdot\vec{a}+im\vec{k}_{0\|}\cdot\vec{b}\Big)\\ &\Rightarrow\ \chi_s(\vec{r'}+l\vec{a}+m\vec{b})=\chi_s(\vec{r'})\end{aligned} \tag{2.28}$$

Here, equation (2.27) and equation (2.28) are known as the Bloch theorem. In other words, the wave function of the electrons within the surface can be expressed as the product of a plane wave and a Bloch function which has the same periodicity of the crystal surface.

Now we perform Fourier expansion of the Bloch function $\chi_s(\vec{r})$,

$$\chi_s(\vec{r})=\sum_{\vec{g}}\alpha_{\vec{g}}(z)\exp\Big(i\vec{g}\cdot\vec{r}_{\|}\Big). \tag{2.29}$$

Due to the translation symmetry equation (2.28), we can find $\vec{g}$ needs to satisfy,

$$\vec{g}\cdot\vec{a}=h\cdot 2\pi, and \tag{2.30}$$

$$\vec{g}\cdot\vec{b}=k\cdot 2\pi. \tag{2.31}$$

In other words, $\vec{g}$ needs to be the reciprocal lattice vector. Substitute equation (2.29) into equation (2.27),

$$\psi_s(\vec{r})=\sum_{\vec{g}}\alpha_{\vec{g}}(z)\exp\Big[(i(\vec{g}+\vec{k}_{0\|})\cdot\vec{r}_{\|}\Big]. \tag{2.32}$$

The diffraction pattern are formed by the back scattered electron, so for $\vec{r}$ outside of the crystal, where $V(\vec{r})=0$, the Schrödinger equation (2.20) is further simplified,

$$-\frac{1}{2}\nabla^2[\psi_i(\vec{r})+\psi_s(\vec{r})]=E[\psi_i(\vec{r})+\psi_s(\vec{r})], \tag{2.33}$$

substitute equation (2.18), we can get,

$$-\frac{1}{2}\nabla^2\psi_s(\vec{r}) = E\psi_s(\vec{r}). \tag{2.34}$$

Now substitute the Fourier expansion of the scattered wave (2.32) into above equation, we can get

$$\sum_{\vec{g}}[(2E - \left|\vec{k}_{0\|} + \vec{g}\right|^2)\alpha_g + \frac{\mathrm{d}^2\alpha_g}{\mathrm{d}z^2}]\exp\left[i(\vec{k}_{0\|} + \vec{g})\cdot\vec{r}_\|\right] = 0. \tag{2.35}$$

Multiply both sides by $\exp\left[-i(\vec{k}_{0\|} + \vec{g}')\cdot\vec{r}_\|\right]$ and integrating over two dimensional unit cell, we can show that each Fourier component must equal to 0, *i.e.*,

$$(2E - \left|\vec{k}_{0\|} + \vec{g}\right|^2)\alpha_g + \frac{\mathrm{d}^2\alpha_g}{\mathrm{d}z^2} = 0, \tag{2.36}$$

$$\Rightarrow \alpha_g(z) = \beta_g \exp\left[\pm\, i(2E - \left|\vec{k}_{0\|} + \vec{g}\right|^2)^{\frac{1}{2}} z\right], \tag{2.37}$$

where β_g is a constant. And the minus sign in the solution above must be chosen since we are dealing with the back scattered electrons. Now we can write the scattered electron wave,

$$\begin{aligned}
\psi_s(\vec{r}) &= \sum_{\vec{g}}\beta_{\vec{g}}\exp\left[(i(\vec{g} + \vec{k}_{0\|})\cdot\vec{r}_\| - i(2E - \left|\vec{k}_{0\|} + \vec{g}\right|^2)z\right] \\
\Rightarrow \psi_s(\vec{r}) &= \sum_{\vec{g}}\beta_{\vec{g}}\exp\left(i\vec{K}_{\vec{g}}^{-}\cdot\vec{r}\right)
\end{aligned} \tag{2.38}$$

$$\text{where, } \vec{K}_{\vec{g}}^{-} = [\vec{k}_{0x} + \vec{g_x}, \vec{k}_{0y} + \vec{g_y}, -(2E - \left|\vec{k}_{0\|} + \vec{g}\right|^2)^{\frac{1}{2}}] \tag{2.39}$$

The superscript in $\vec{K}_{\vec{g}}^{-}$ indicates the back-scattering direction of the wave vector. Now we have decomposed the scattered wave to a series of discrete beams each with a parallel component of momentum, $(\vec{k}_{0\|} + \vec{g})$. And the component of momentum in the direction normal to the surface,

$$\vec{K}_z^- = -(2E - \left|\vec{k}_{0\|} + \vec{g}\right|^2)^{\frac{1}{2}}. \tag{2.40}$$

As shown in Eq. 2.39, $\vec{K}_{\vec{g}}^-$ is the back-scattered wave vector. The above Eq. 2.40 is also a result of the conversation of energy for elastically scattered electrons, which has the same energy as the incident electron,

$$E = \frac{1}{2}(\vec{K}_{\|}^- + \vec{K^-}_z)^2, \tag{2.41}$$

where, $\vec{K}_{\|}^- = \vec{k}_{0\|} + \vec{g}$. Equation (2.38) also shows that given a incident beam of electrons at finite energy, only finite number of beams emerge from the crystal, thus will be observed in the diffraction pattern. This is because for equation (2.36) to have real solutions, $\vec{g}$ need to satisfy,

$$\left|\vec{k}_{0\|} + \vec{g}\right|^2 \leqslant 2E. \tag{2.42}$$

When $(\vec{k}_{0\|} + \vec{g})$ is larger than this critical value, the z-component of the scattered waves become complex which means that the beam amplitude will exponentially damp, thus will never reach the screen. In another point of view, the finite diffraction beam at given incident electron energy is the result of the conservation of energy, equation (2.41). When increasing the incident electron energy E, a larger number of diffraction beams will be allowed, as can be seen in Fig. 2-4, the diffraction pattern will contract to allow more diffracted beams to be present on the screen.

Low energy electron diffraction (LEED) is now a well established surface atomic structure characterization technique. The energy range of the probing electrons is usually around 20 to 500 eV. The electron inelastic mean-free-path (eMFP) for this energy range is between 5 to 10 Å, as shown in the plots of the universal eMFP against electron kinetic energy in many solids, Fig. 2-5 [3]. The short eMFP makes LEED extremely sensitive to the surface

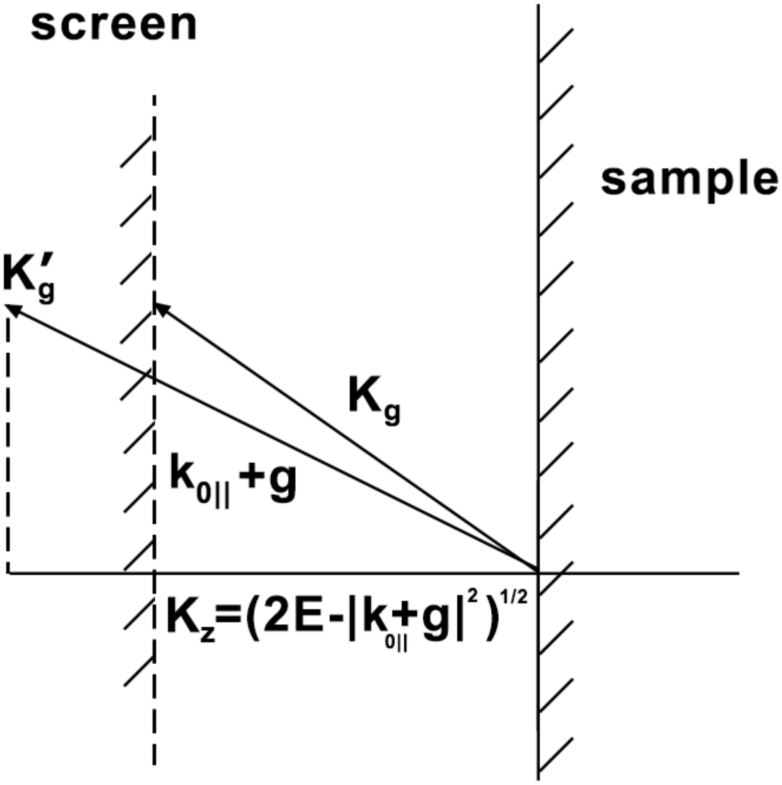

Figure 2-4: Relationship between the elastically back scattered wave vector $\vec{K_g}$ and incident electron energy E.

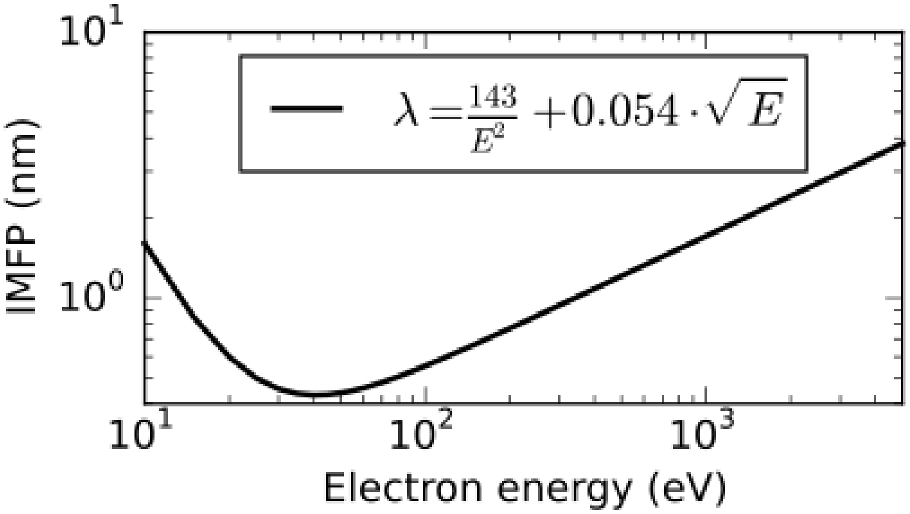

Figure 2-5: Universal curve for the electron inelastic mean free path (IMFP) in elements based on equation (5) in [3].

atomic structure of materials. At higher energies, the electrons behave more like particles, so the higher energy the electrons possess, the deeper they will penetrate the solid. At lower energies, the electrons behave more like waves, and the lower energy they possess, the larger their wavelengths are, so it will travel further in the solids as well.

2.2 LEEM and μLEED-IV

The primary experimental techniques used for the work presented in this thesis are low energy electron microscopy (LEEM) and its complementary selected area micro-spot low energy electron diffraction (μLEED). Since its invention in 1962 by Bauer [50], LEEM has developed into one of the premier experimental techniques for surface and interfaces studies [51, 52, 53, 54, 55]. Commercialized LEEM facilities are only available from two companies, ELMITEC (since 1997) and SPECS (since 2007). There are about 30 LEEM facilities in operation throughout the world, at present. Figure 2-6 shows the schematic abberation-corrected LEEM (AC-LEEM) setup at the Brookhaven National Laboratory (BNL). The AC-LEEM system consists of an entrance chamber with a load-lock (ECh) for transferring samples to the vacuum chamber, a preparation chamber (PCh) for sample preparation, main sample chamber (MCh) where the sample is placed and electron optics column (COL) where electron beam is created, collimated, directed onto sample surface and redirected to imaging plane after diffracted by sample surface.

2.3 LEEM Optics and Imaging Principles

Figure 2-7 shows the electron-optical path of the LEEM system. Electrons are emitted by an electron gun and accelerated by a high voltage of 20 kV. The electron beam is then collimated by a series of electro-magnetic lenses (condenser lenses) and deflected by the magnetic prism in the sector field, onto the projective lens. The objective lens acts on the incident and reflected electron beams together and serves a dual purpose in both cases. It focuses the incident beam to a parallel beam or plane wave projected perpendicular to the sample. A bias of -20 kV between the objective lens and the sample decelerates the electrons to the low energy range of 0-500 eV. After interacting with the sample surface, the diffracted electrons go through the objective lens again. Different orders of diffracted electron beams are focused onto the back focal plane (BFP) forming diffraction pattern. The image of the sample surface is formed on the image plane behind the BFP. The reflected electrons are also reaccelerated to microscope potential by the objective lens bias voltage and then deflected by the magnetic prism to the imaging column. All the electric-magnetic lenses and magnetic prisms are computer-controlled and adjustable by user. One can choose to project the image plane onto the detector screen, in which way, one can obtain the real-space, real-time image of the sample surface. Usually, an aperture is utilized in the electron-optical path to only allow the diffracted (00) beam to go through, which is the so-called bright-field imaging mode. One can also choose to project the diffraction pattern to the detector screen, from which, one can extract the detailed surface lattice structural information with

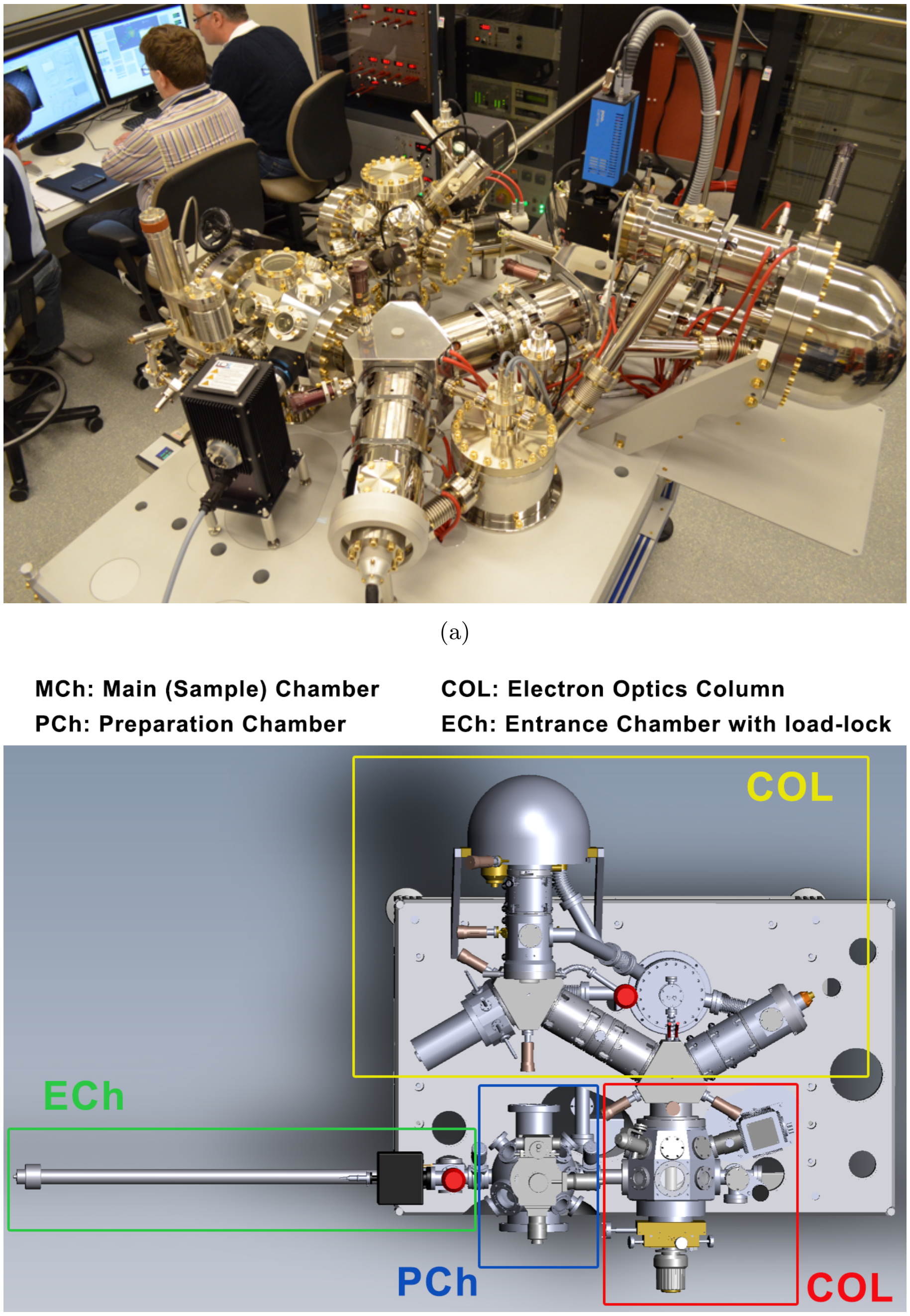

(a)

(b)

Figure 2-6: Schematic of AC-LEEM at BNL: (a) AC-LEEM in operation at the Center for Functional Nanomaterials (CFN) at BNL; (b) Top view of the AC-LEEM set-up at BNL.

the help of dynamical analysis. This is the so-called diffraction mode. Due to the low energy of the interacting electrons, one can achieve real-time in situ imaging of the sample surface with minimum disturbance of the material surface structure. The AC-LEEM system in BNL has a high spatial resolution of about 2 nm. Even though it can not compete with other scanning probing microscopy such as scanning tunneling microscopy (STM) regarding spatial resolution, it has the advantage of faster and real-time imaging with a temporal resolution as high as 15 ms. At the same time, it has the unique combined surface structure investigation ability in both real and reciprocal spaces with its complementary diffraction mode.

In the diffraction mode, one can choose different aperture to limit the illumination area to a few μm. This is the so-called selected area μLEED mode. By tuning the incident electron energy, and recording the corresponding diffracted beam intensities, we can obtain the so-called LEED-IV curves. Combined with dynamical analysis, one can extract the local surface structural information in 3D with the μLEED-IV technique.

When the illumination source is switched from electrons to ultra-violet (UV) light, the LEEM facility is working in the photo-emission electron microscopy (PEEM) mode. PEEM utilizes local variations in photon-excited electron emission to generate image contrast. The resolution is not as good as in LEEM, but at lower magnification, differences in the work function of different materials are easily visible. This mode is often used to align the sample position to get a normal electron incidence and to find the target area for further imaging and investigation.

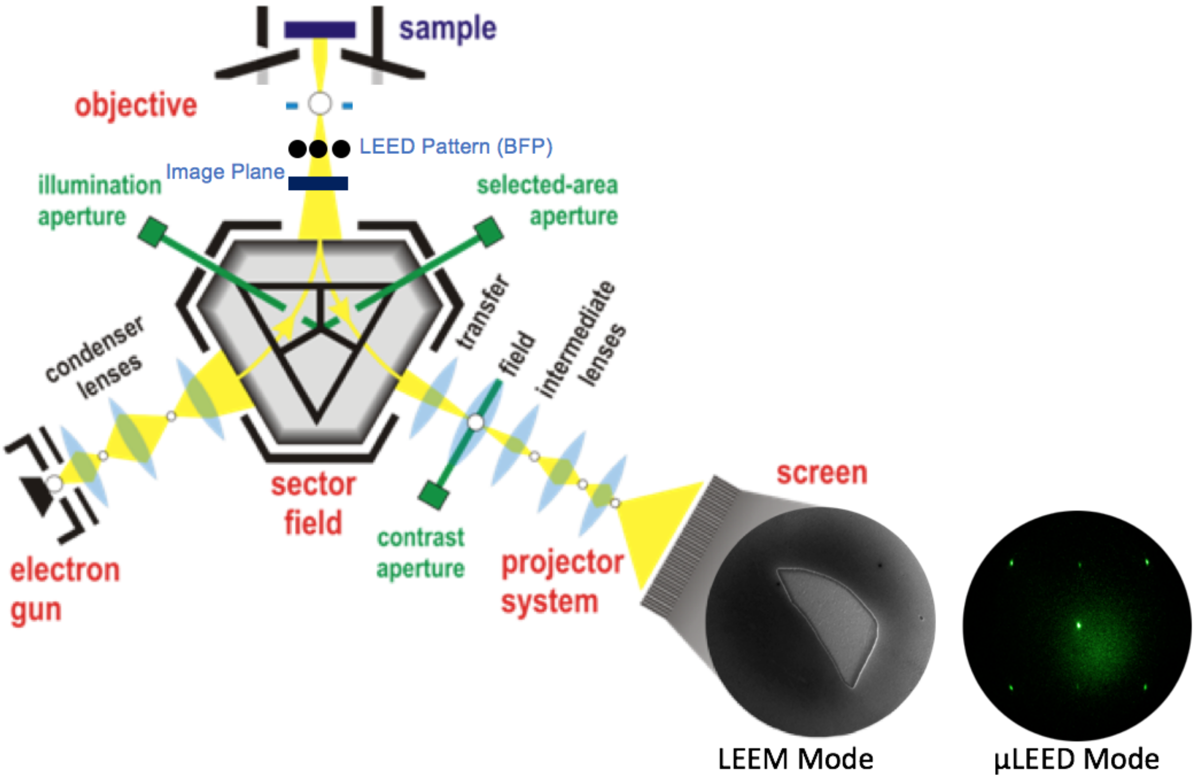

Figure 2-7: Schematic of the electron-optical path of LEEM.

CHAPTER 3

ADVANCEMENT OF DYNAMICAL LEEM/μLEED-IV ANALYSIS

3.1 Introduction to Dynamical LEED-IV Analysis Theory

The kinematic theory of electron diffraction, introduced in Sec. 2.1, is sufficient to explain the LEED pattern. Some of the surface layers structural information can be obtained from the LEED pattern, such as the surface two-dimensional symmetry, surface ordered reconstruction or super-lattice structure. However, if one wants to access the structural information in the out-of-plane direction, i.e., the interlayer spacings or the surface termination elements, the LEED-IV data can be used. Due to the low electron energy used in the LEED experiments, electrons experience multiple scattering from the atoms in the solids, unlike X-rays. A complete understanding of the LEED process is essential for interpreting the LEED-IV data and extracting the above said surface structural information. This is known as the dynamical LEED-IV analysis, which involves the electron scattering by atoms in each atomic layer, multiple scattering by the atoms in the surface layers, and a dynamical search process for a most probable surface structure that would reproduce the measured LEED-IV curves with the best agreement. This section will present the main ingredients of the multiple scattering theory, detailed derivation can be found in books by Pendry [56], Van Hove *et. al.,* [57] and our former group member Jiebing Sun's Ph.D thesis [2], more details about the main programs can be found in Van Hove and Tong's book [58].

3.1.1 Atom Scattering and Phase Shifts

- Muffin-tin Model

Most of the inelastically scattered electrons are screened out experimentally by the energy filter employed in the LEED apparatus. Thus, the elastic scattering of the electrons by atoms in the solids is of main concern of the LEED theory. There are two main interacting potentials responsible for the elastic scattering of electrons in the surface. First, there is an electrostatic force between the diffracting electrons and all the point charges present at the surface. This is presented by a periodic potential in the form of $-Ze/|\vec{r}-\vec{r_n}|$ near each nucleus $\vec{r_n}$, where Z is the nuclear charge at $\vec{r_n}$. The core electrons manage to screen the nuclei completely only outside of the atomic radius. The second part of the interacting potential is due to the Pauli exclusion principle, which tends to keep electrons away from each other. Based on above assumption, the relevant Schrödinger equation can be written as following:

$$
\begin{aligned}
&\Bigg[-\frac{\hbar^2}{2m}\vec{\nabla}_j^{\,2}-\sum_j\frac{Z_je^2}{|\vec{r}-\vec{r}_{nj}|}+V_{sc}(\vec{r})+\sum_i\int\frac{e^2\big|\Psi_i(\vec{r_i})\big|^2}{|\vec{r}-\vec{r_i}|}d^3r_i\Bigg]\psi(\vec{r})\\
&-\sum_i\Bigg[\int\frac{e^2\Psi_i^*(\vec{r_i})\psi(\vec{r_i})}{|\vec{r}-\vec{r_i}|}d^3r_i\Bigg]\Psi_i(\vec{r})=E\psi(\vec{r})
\end{aligned}
\tag{3.1}
$$

Here $\Psi_i(\vec{r_i})$ (i=1,...,N) are the wave functions for the system of all N electrons of the surface; $\psi(\vec{r})$ is a LEED electron; Z_j is the nuclear charge at position $\vec{r}_{nj}$ and $V_{sc}(\vec{r})$ is the potential due to core electrons that screens the LEED electron (usually neglected); the term in the second set of square brackets are the exchange terms. The computation of Eq. 3.1 can be substantially reduced by making the exchange local through the Slater approximation

[4.16]:

$$V_{ex}(\vec{r}) = -3\alpha\Big[\frac{3\rho(\vec{r})}{8\pi}\Big]^{1/3}, \tag{3.2}$$

where $\rho(\vec{r})$ is the local density of bound electrons:

$$\rho(\vec{r}) = e\sum_i \left|\Psi_i(\vec{r})\right|^2. \tag{3.3}$$

The factor α adopt values varies between 2/3 and 1, depending on the situation and on the author's choice [56].

However, the Schrödinger equation 3.1 for LEED electrons still can not be solved computationally even with the Slater approximation 3.2. This is due to the surface electrons wave functions Ψ_i and charge distribution ρ are still unknown. But if we make the assumption that the potential within a radius around each atom is spherically symmetric, and the spheres surrounding the neighboring atoms do not overlap with each other. Equation 3.1 can then be further reduced to a one-dimensional differential equation when solved in terms of partial waves. The solutions then would be written as the product of a radial function $R_l(r)$ and a spherical harmonic $Y_{lm}(\theta, \varphi)$, where $R_l(r)$ satisfies the following radial differential equation:

$$-\frac{\hbar^2}{2m}\left[\frac{1}{r^2}\right]\frac{d}{dr}\left[\frac{dR_l(r)}{dr}\right]+\frac{\hbar^2 l(l+1)}{2mr^2}R_l(r)+\left[-\frac{Ze^2}{r}+V_{sc}(r)+V_{ex}(r)\right]R_l(r) = ER_l(r). \tag{3.4}$$

We have now arrived at the well know 'muffin-tin' model for solving the LEED problem, as shown in Fig. 3-1. Each atom on the surface is described by a spherical potential within a sphere that does not overlap the other spheres surrounding the neighboring atoms. The idea is to solve the partial wave Schrödinger equation 3.4 within each sphere and then match these solutions to the local solutions to the other parts of space. These other parts of space include the interstitial regions between the muffin-tin spheres and the region between

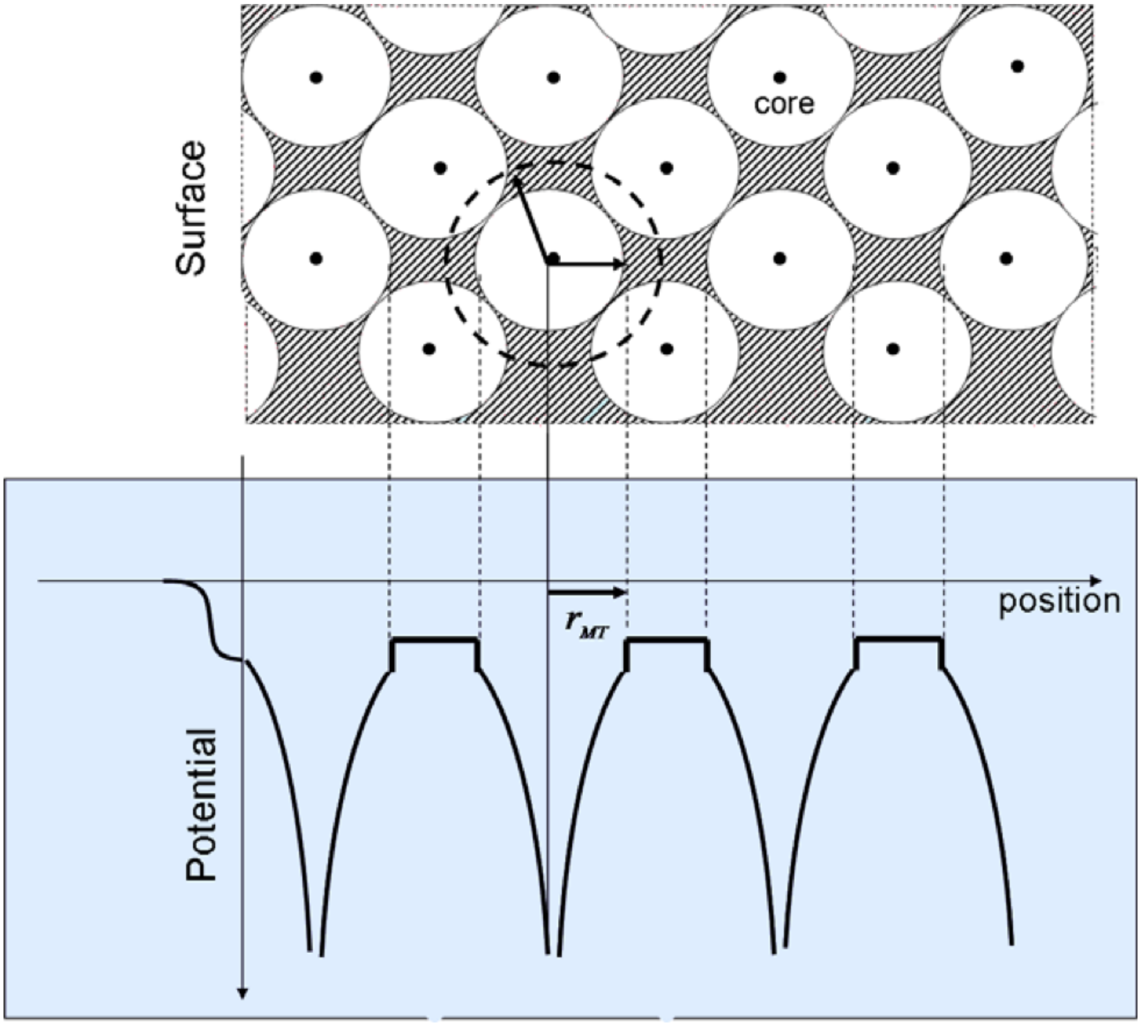

Figure 3-1: Muffin-tin model for electron scattering on the surface. Top panel shows the spheres surrounding atoms with spherical potential; bottom panel shows the function of the spherical potential within the muffin-tin radius $\vec{r}_{MT}$ and the constant potential in the interstitial region, indicated as the shaded region in the top panel. [4]

different surface layers or the surface and vacuum.

- Inelastic Scattering

Now we turn to the interstitial region, which is indicated as the shaded region in the top panel of Fig. 3-1. The interstitial regions have potential variations (usually within a few eV) that are relatively small compared to electron energies used in LEED. Thus, the potential is usually assumed constant in the LEED calculations. This potential is known as the muffin-tin constant or inner potential. The muffin-tin constant influences the calculated *IV* curve by a rigid shift along the energy axis. Present theories are not capable of calculating this potential accurately for input in the LEED calculations. Alternatively, it is treated as an adjustable parameter that is fit to the experiment during a structural optimization. In the interstitial region, the interactions between LEED electrons and plasmon excitation or phonons that introduces small energy losses would contribute to the inelastic scattering and can not be filtered out by the LEED apparatus. This part of the inelastic scattering is described by introducing an imaginary part of the inner potential, which is often referred to as the damping potential.

- Temperature Effect

The temperature, which induces atomic vibration, will decrease the reflected beam intensity as,

$$I = I_0 \exp(-2M), \tag{3.5}$$

where $\exp(-2M)$ is the Debye-Waller factor and it has the form,

$$\exp(-2M) = \exp\Big[-|\vec{s}|^2 < (\Delta\vec{r})^2 >\Big] \exp\big[\frac{3\hbar^2 |\vec{s}|^2 T}{m_a k_B \theta_D^2}\big] \tag{3.6}$$

Here $\vec{s}$ is the three-dimensional momentum transfer of the beam under consideration, $\sqrt{(\Delta\vec{r})^2}$ is the root-mean-square atomic vibrational amplitude, and θ_D is the Debye temperature. In the LEEDopt package, the temperature effect is input as the mean-square atomic vibrational displacements $\langle u^2 \rangle_T$ for individual atomic layers. $\langle u^2 \rangle_T$ can be optimized and used to derive the Debye temperature of individual atomic layers using the following equation [56]:

$$\langle u^2 \rangle_T = \frac{9\hbar^2}{m_a k_B \theta_D} \Big\{ \frac{T^2}{\theta_D^2} \int_0^{\frac{\theta_D}{T}} \frac{x dx}{e^x - 1} + \frac{1}{4} \Big\}, \tag{3.7}$$

where m_a is the atomic mass, $\hbar$ is the Planck's constant and k_B is the Boltzmann constant.

3.1.2 Introduction to Multiple Scattering Theory

- Atomic Scattering and Phase Shifts

First we consider the spherical-wave presentation of the atomic scattering in the interstitial region. With a constant potential throughout the interstitial region, the solution for Eq. 3.4 is the Bessel function j_l for any positive integer l:

$$R_l(kr) = j_l(kr) = \alpha_l h_l^{(1)}(kr) + \beta_l h_l^{(2)}(kr), \tag{3.8}$$

where α_l and β_l are constants, $h_l^{(1)}$ and $h_l^{(2)}$ are the spherical Hankel functions of the first and second kind, respectively. The expansion of $h_l^{(1)}$ and $h_l^{(2)}$ can be found in [56]. $h_l^{(2)}(kr)$ behaves for large r as,

$$h_l^{(2)}(kr)_{r\to\infty} = i^{(l+1)}\frac{\exp(-ikr)}{kr}, \tag{3.9}$$

which can be identified as the incoming wave. On the other hand

$$h_l^{(1)}(kr)_{r\to\infty} = i^{-(l+1)}\frac{\exp(+ikr)}{kr}, \tag{3.10}$$

can be identified as the outgoing wave. Since the above described ion-core potential is considered as elastic and thus conserves the current of the electron beams, the outgoing wave should have the same magnitude as the incoming wave, but may differ in phase. Therefore, outside the muffin tin radius, the total wave should take the form:

$$R_l(kr) = \beta_l\big[\exp(2i\delta_l)h_l^{(1)}(kr) + h_l^{(2)}(kr)\big]. \tag{3.11}$$

Here δ_l is known as the phase shift for angular momentum l. δ_l can be obtained by getting the logarithmic derivative of $R_l(kr)$ at the boundary of the muffin tin sphere, r_m:

$$L_l(R) = \frac{R_l'(r_m)}{R_l(r_m)} = \frac{\exp(2i\delta_l)h_l^{(1)'}(kr) + h_l^{(2)'}(kr)}{\exp(2i\delta_l)h_l^{(1)}(kr) + h_l^{(2)}(kr)}. \tag{3.12}$$

Then we can derive,

$$\exp(2i\delta_l) = \frac{L_l h_l^{(2)} - h_l^{(2)'}}{h_l^{(1)'} - L_l h_l^{(1)}}. \tag{3.13}$$

$L_l(r_m)$ can be calculated through integrating over Eq. 3.4, given atomic number, electron configuration of the atom and muffin tin radius r_m.

We can decompose radial wave solution Eq. 3.11 into unscattered $R_l^{(0)}$ and scattered $R_l^{(s)}$ components:

$$R_l = R_l^{(0)} + R_l^{(s)} \tag{3.14}$$

$$R_l^{(0)} = \beta_l[h_l^{(1)} + h_l^{(2)}] = \beta_l \cdot 2j_l \tag{3.15}$$

$$R_l^{(s)} = \beta_l[\exp(2i\delta_l) - 1]h_l^{(1)} \tag{3.16}$$

Now we turn back to the plane wave presentation of an incoming and unperturbed wave and expand it in the spherical wave form:

$$\exp\left(i\vec{k}\vec{r}\right) = \sum_{l=0}^{\infty} \sum_{m=-l}^{+l} 4\pi * i^l j_l(kr) Y_{lm}^*(\Omega(\vec{k})) Y_{lm}(\Omega(\vec{r})) = R_l^{(0)} \cdot Y_{lm}. \tag{3.17}$$

From the above equation we can get,

$$R_l^{(0)} = 2\pi i^l Y_{lm}^*(\Omega(\vec{k})) \cdot 2j_l(kr). \tag{3.18}$$

And,

$$\beta_l = 2\pi i^l Y_{lm}^*(\Omega(\vec{k})) \tag{3.19}$$

Now with β_l known we can write the explicit form of the scattered wave $R_l^{(s)}$. And by adding the $R_l^{(s)}$ that is corresponding to different angular momentum l, we can get the total scattered wave:

$$\begin{aligned} R^{(s)} &= \sum_{lm} 2\pi i^l [\exp(2i\delta_l) - 1] Y_{lm}^*(\Omega(\vec{k})) \times Y_{lm}(\Omega(\vec{r})) h_l^{(1)}(kr) \\ &= \sum_l i^{l+1} \sin(\delta_l) \exp(i\delta_l)(2l+1) \times P_l(\cos\left(\theta^{(s)}\right)) h_l^{(l)}(kr), \end{aligned} \tag{3.20}$$

where $\theta^{(s)}$ is the angle between scattered direction $\vec{r}$ incident wave direction $\vec{k}$. Here we utilized the relationship between the Legendre polynomials and the spherical harmonics:

$$\sum_{m=-l}^{+l} Y_{lm}^*(\Omega) Y_{lm}(\Omega') = \frac{2l+1}{4\pi} P_l(\cos(\theta)). \tag{3.21}$$

The above scattered radial wave takes the asymptotic form at large distance:

$$R^{(s)}(\vec{r})_{r\to\infty} = t(E, \theta^{(s)}) \left[-\frac{\exp(ikr)}{2\pi r} \right], \tag{3.22}$$

where,

$$t(E, \theta^{(s)}) = \frac{-2\pi}{k} \sum_l (2l+1) \sin(\delta_l) \exp(i\delta_l) P_l(\cos\theta^{(s)}). \tag{3.23}$$

And the total wave, after scattered by the atomic spherical symmetry potential, can be written as:

$$\psi(\vec{r}) = \exp\left(i\vec{k_0} \cdot \vec{r}\right) + t(E, \theta) \frac{\exp\left(i\vec{k_0} \cdot \vec{r}\right)}{r}. \tag{3.24}$$

The above solution indicates that the back scattered wave takes the asymptotic form for $r \to \infty$, which is consist of the incident electron wave and scattered wave. The scattered wave takes the Bloch wave form. Here $t(E, \theta)$ is the angular distribution of the scattered wave and it is usually referred to as the 't-matrix'.

- Intralayer Multiple Scattering

Now we consider a layer of atoms arranged in the form of a Bravais lattice. Based on Bloch's theorem, we can assume the waves incident on the plane can be written as a set of plane waves with momentum of $\vec{K}_g$,

$$\sum_{\vec{g}} U_{\vec{g}}^{+} \exp\Big(i\vec{K}_{\vec{g}}^{+} \cdot \vec{r}\Big), \tag{3.25}$$

where $U_{\vec{g}}$ is a periodic function that has the same periodicity as the Bravais lattice. The plane wave form can be rewritten in terms of the spherical wave expansion about the kth ion core in the unit cell at the origin,

$$\begin{aligned}
&\sum_{\vec{g}} U_{\vec{g}}^{+} \exp\Big(i\vec{K}_{\vec{g}}^{+} \cdot \vec{r}\Big) \\
&= \sum_{lm} A_{lmk}^{(0)} j_l(k\Big|\vec{r} - \vec{R}_{0k}\Big|) Y_{lm}(\Omega(\vec{r} - \vec{R}_{0k})) \qquad (3.26) \\
&= \sum_{lm} A_{lmk}^{(0)} \frac{1}{2}[h_l^{(1)}(k\Big|\vec{r} - \vec{R}_{0k}\Big|) + h_l^{(2)}(k\Big|\vec{r} - \vec{R}_{0k}\Big|)] \cdot Y_{lm}(\Omega(\vec{r} - \vec{R}_{0k}))
\end{aligned}$$

Here, $k = \Big|\vec{K}_{\vec{g}}^{+}\Big|$; $\Omega(\vec{r} - \vec{R}_{0k})$ stands for the angular coordinates of $(\vec{r} - \vec{R}_{0k})$; $h_l^{(1)}$ and $h_l^{(2)}$ are outgoing and incoming partial waves, as described in the previous section; the constant $A_{lmk}^{(0)}$ is given by

$$A_{lmk}^{(0)} = \sum_{\vec{g}} U_{\vec{g}}^{+} \exp\Big(i\vec{K}_{\vec{g}}^{+} \cdot \vec{R}_{0k}\Big) 4\pi i^l (-1)^m Y_{l-m}(\Omega(\vec{K}_{\vec{g}}^{+})). \tag{3.27}$$

The distance between the kth atom in the jth unit cell and kth atom in the unit cell at origin is,

$$\vec{R}_{jk} - \vec{R}_{0k} = \vec{R}_j, \tag{3.28}$$

R_j is a lattice vector of the plane, so

$$\vec{R_j} \cdot \vec{g} = 2\pi \cdot integer. \tag{3.29}$$

Then we have,

$$\begin{aligned}\vec{K_g^+} \cdot (\vec{R}_{jk} - \vec{R}_{0k}) &= (\vec{k_{0||}} + \vec{g}) \cdot (\vec{R}_{jk} - \vec{R}_{0k}) \\ &= \vec{k}_{0||} \cdot (\vec{R}_{jk} - \vec{R}_{0k}) + 2\pi \cdot integer.\end{aligned} \tag{3.30}$$

So the wave function at $\vec{R}_{jk}$ should have the similar form as at $\vec{R}_{0k}$ (3.26), but with a phase factor

$$\exp\Big[i\vec{k}_{0||} \cdot \vec{R_j}\Big]. \tag{3.31}$$

And the amplitudes in the spherical wave expansion form should differ by the same factor, i.e.,

$$A^{(0)}_{lmk}(j\text{th cell}) = A^{(0)}_{lmk}(0\text{th cell}) \cdot \exp\Big[i\vec{k}_{0||} \cdot \vec{R_j}\Big]. \tag{3.32}$$

The total amplitude of waves incident on any ion core in any unit cell should have the following form,

$$A_{lmk} = A^{(s)}_{lmk} + A^{(0)}_{lmk}. \tag{3.33}$$

Here $A^{(s)}_{lmk}$ is the amplitude of the scattered waves from all the other ion cores and itself depends on A_{lmk} too.

From the previous section we know that, after atomic scattering, the scattered or outgoing part of the wave, $h^{(1)}_l$, must have a phase shift factor $(\exp\big[2i\delta_l(k)\big] - 1)$. Thus, the scattered wave from the kth atom in the jth unit cell must have the following form:

$$\sum_{lm} A^{(0)}_{lmk} \frac{1}{2}(\exp\big[2i\delta_l(k)\big] - 1) h^{(1)}_l(k\Big|\vec{r} - \vec{R}_{jk}\Big|) \cdot Y_{lm}(\Omega(\vec{r} - \vec{R}_{jk})) \cdot \exp\Big[i\vec{k}_{0||} \cdot \vec{R_j}\Big]. \tag{3.34}$$

Here $\delta_l(k)$ is the phase shift due to atomic scattering at the kth atom in any unit cell. The summation of the above equation over j and k will give us the total scattered wave. Now let's consider the sth ion core in the unite cell at the origin. The formula for transferring an expansion about the (jk)th site to the (0s)th site can be conveniætly found in the literature [56]. The total wave should have the form,

$$\begin{aligned}\sum_{jk}{}' \sum_{lm} A_{lmk} \frac{1}{2}(\exp\left[2i\delta_l(k)\right] - 1)\exp\left[i\vec{k}_{0||}\cdot\vec{R}_j\right] \\ \times \sum_{l''m''} G_{lm,l''m''}(\vec{R}_{0s} - \vec{R}_{jk}) j_{l''}(k\left|\vec{r} - \vec{R}_{0s}\right|) Y_{lm}(\Omega(\vec{r} - \vec{R}_{0s}))\end{aligned} \tag{3.35}$$

The prime on the second summation denotes that the sth ion core in the unit cell at the origin is omitted. Then we expand the above Eq. 3.35 in the spherical wave presentation about the sth ion core. Comparing the above Eq. 3.35 and the spherical wave expansion of the plane wave incident on the $(0s)$th site, we can get that,

$$A^{(s)}_{l''m''s} = \sum_{lmk} A_{lmk} \cdot X_{lmk,l''m''s} \tag{3.36}$$

$$X_{lmk,l''m''s} = \sum_{j}{}' \frac{1}{2}(\exp\left[2i\delta_l(k)\right] - 1)\exp\left[i\vec{k}_{0||}\cdot\vec{R}_j\right] G_{lm,l''m''}(\vec{R}_{0s} - \vec{R}_{jk}) \tag{3.37}$$

Using Eq. 3.36 and 3.33, we can solve for A_{lmk},

$$A_{lmk} = \sum_{l'm'k'} A^{(0)}_{l'm'k'} \cdot (1 - X)^{-1}_{l'm'k',lmk}. \tag{3.38}$$

If we express the wave incident on the plane as:

$$\psi = \sum_{\vec{g'}} V_{\vec{g'}} \exp\left(i\vec{K}_{g'}\cdot\vec{r}\right). \tag{3.39}$$

And we can get,

$$V^{\pm}_{\vec{g}'} = \sum_{\vec{g}} M^{\pm\pm}_{\vec{g}'\vec{g}} U^{+}_{\vec{g}}. \tag{3.40}$$

After substitution of all the relevant variables, we can get,

$$\begin{aligned} M^{\pm\pm}_{\vec{g}'\vec{g}} = & \frac{8\pi^2 i}{\left|\vec{K}^{\pm}_{\vec{g}}\right| A K^{+}_{\vec{g}'z}} \sum_{l'm'k',lmk} \exp\left(i\vec{K}^{\pm}_{\vec{g}} \cdot \vec{r_k} - i\vec{K}^{\pm}_{\vec{g}'} \cdot \vec{r'_k}\right) \\ & \times [i^l(-1)^m Y_{l-m}(\Omega(\vec{K}^{\pm}_{\vec{g}}))](1-X)^{-1}_{lmk,l'm'k'}[i^{-l'} Y_{l'm'}(\Omega(\vec{K}^{\pm}_{\vec{g}'}))] \\ & \times \exp\left[i\delta_l(k')\right] \sin[\delta_{l'}(k')] \end{aligned} \tag{3.41}$$

Equation 3.41 is the formula used in the LEED calculation programs for the scattering matrix for a single Bravais lattice layer.

- Layer stacking

Once we get the scattering matrix for the single layer, we can stack these layers together to get scattering matrices for multiple surface layers or bulk. There are mainly two approaches for stacking layers, layer doubling method and renormalized forward scattering (RFS) perturbation method.

The layer doubling method stacks two identical layers to get a new layer (slab). Then the new slab will be stacked with another slab. This double layer stacking is repeated until the reflected beam converges. The RFS method assumes that the reflection by layers is weak and only limited number of layers needed to be considered in the multiple scattering. The result is achieved through perturbation based on an expansion of the total reflectivity in terms of the number of time the waves get reflected. For example, the 1st order perturbation considers all the scattering paths that the waves have been reflected once, the 2nd order includes only triple-reflection paths, and so on. In general, the RFS method is more efficient. However it converges poorly for closely spaced layers. For the RFS method to converge properly, the interlayer spacing larger than ∼0.9 Å. On the other hand, the layer doubling method requires the interlayer spacing to be larger than ~0.5 Å. In the situation that some layer spacings are small while others are large, multiple methods are utilized for stacking layers. This method is the so-called combined-space method.

3.1.3 Adams' LEEDopt Calculation Package

The main calculation package used in this thesis, LEEDopt was originally written by David Adams *et. al.* [5], which were developed from programs by Pendry [56] and Van Hove and Tong [58]. Here I present the main aspects of the LEEDopt package.

- Reliability Factor

The agreement between the calculated and experimental LEED-IV curves is quantified and assessed by the reliability factor (R-factor). There are various types of reliability factors adopted by different calculation packages [58]. The reliability factor used in the Adams' codes and throughout this thesis is a normalized χ^2 function, R_2, defined as following.

$$R_2 = \sum_{hk,i} \left(\frac{I^{exp}_{hk,i} - cI^{cal}_{hk,i}}{\sigma_{hk}} \right)^2 / \sum_{hk,i} (\frac{I^{exp}_{hk,i}}{\sigma_{hk}})^2 \tag{3.42}$$

Here $I^{exp}_{hk,i}$ and $I^{cal}_{hk,i}$ are experimental and calculated beam intensities, respectively. (hk) are indexes for different diffracted beams and i is the index for different incident electron energies. σ_{hk} is the root-mean-square experimental uncertainty of the beam (hk), obtained via comparison of measured symmetry-equivalent diffracted beams. c is a scaling constant which can be determined by the requirement that $\partial R_2/\partial c = 0$ and has the form:

$$c = \sum_{hk,i} \left(\frac{I^{exp}_{hk,i} I^{cal}_{hk,i}}{\sigma^2_{hk}} \right) / \sum_{hk,i} \left(\frac{I^{cal}_{hk,i}}{\sigma_{hk}} \right)^2 . \tag{3.43}$$

The R_2 used here considers all the information contained in the variation of intensity as a function of energy for a given diffracted beam, and the relative intensities from beam to beam. This has the advantage over other types of R-factors that neglects the relative intensity between different beams. It is thus more suitable for experiments with smaller data set, such as the μLEED-IV collected on the small sampling area of various 2D materials presented in this thesis.

- Program Algorithm

LEEDopt is an automated surface structural parameter optimization package. It includes two practically independent parts. One of the two parts is the set of Fortran programs for calculating LEED-IV curves based on input structural parameters. The second part of the LEEDopt package is a parameter optimization or iteration program, also referred to as LEEDopt, that is written in Visual Basic (not supported anymore), and can be only run on Windows OS. This part calls a set of Fortran Codes that calculates the LEED-IV with a set of input structural parameters. The parameters optimization part of the LEEDopt package utilizes the quadratic tensor model (QTM) algorithm. The details of this algorithm can be found in [5, 59]. This algorithm has the advantage of rapid convergence while optimizing multiple parameters simultaneously.

In the QTM method, the following residual function is used to optimize the parameters.

$$f_i = \frac{I^{exp}_{hk,i} - I^{cal}_{hk,i}}{K^{\frac{1}{2}}\sigma_{hk}}, \tag{3.44}$$

where,

$$K = \sum_{hk,i} (I^{ex}_{hk,i}/\sigma_{hk})^2, \tag{3.45}$$

and index i runs over the energy range. The residual function f_i is related to the R-factor in the following way:

$$R = \left\| f(x) \right\|^2 = \sum_{i=1}^{m} f_i^2(x). \tag{3.46}$$

Here m is the number of the total data points. The goal of the QTM optimization method is to find a set of input parameters, $x_1, ..., x_N$, that minimize the R-factor.

A set of initial structural and non-structural parameters are written into input files and read into the program. LEED intensities are calculated using the dynamical theory of LEED as described in section 3.1. The atomic scattering phase shifts are calculated by programs developed by Van Hove [60]. The flow chart of the whole run of the LEED-*IV* calculations is shown in Fig. 3-3. The program *leedlay* calculates the reflection and transmission matrices for layers that consist of a single Bravis lattice. Composite layers, that have more than one subplanes, are calculated by the program *leedcs*. The scattering matrices created by *leedlay* or *leedcs* are stored on the disk so that they can be used for the next steps. The reflection matrices for the bulk crystal is calculated by *leedbulo* using the scattering matrices calculated by *leedlay* for bulk layers, via Pendry's layer-doubling method [56]. The diffracted beam intensities are calculated by *leedselo*, using the scattering matrices for surface layers that were calculated either by *leedlay* or *leedcs*. Then the R-factor, that quantifies the disagreement between the calculated and experimental *IV* curves, are calculated by the program *rgrad*. The R-factor is then read-in by LEEDopt and passed to a fortran program *drivopt*, which in turn calls individual LEED fortran programs to calculate the partial derivatives relative of the residue function (defined in Eq. 3.44) with respect to each input parameter. Then the R-factor and partial derivates are passed to the QTM program *dqed*. *dqed* will judge if a minimum R-factor has been reached or not. If convergence is not reached, *dqed* will predict a new set of input parameters based on the derivatives information. Then the second and further iterations are carried out until the R-factor minimum is reached. The flow chart of the LEEDopt package is shown in Fig. 3-2.

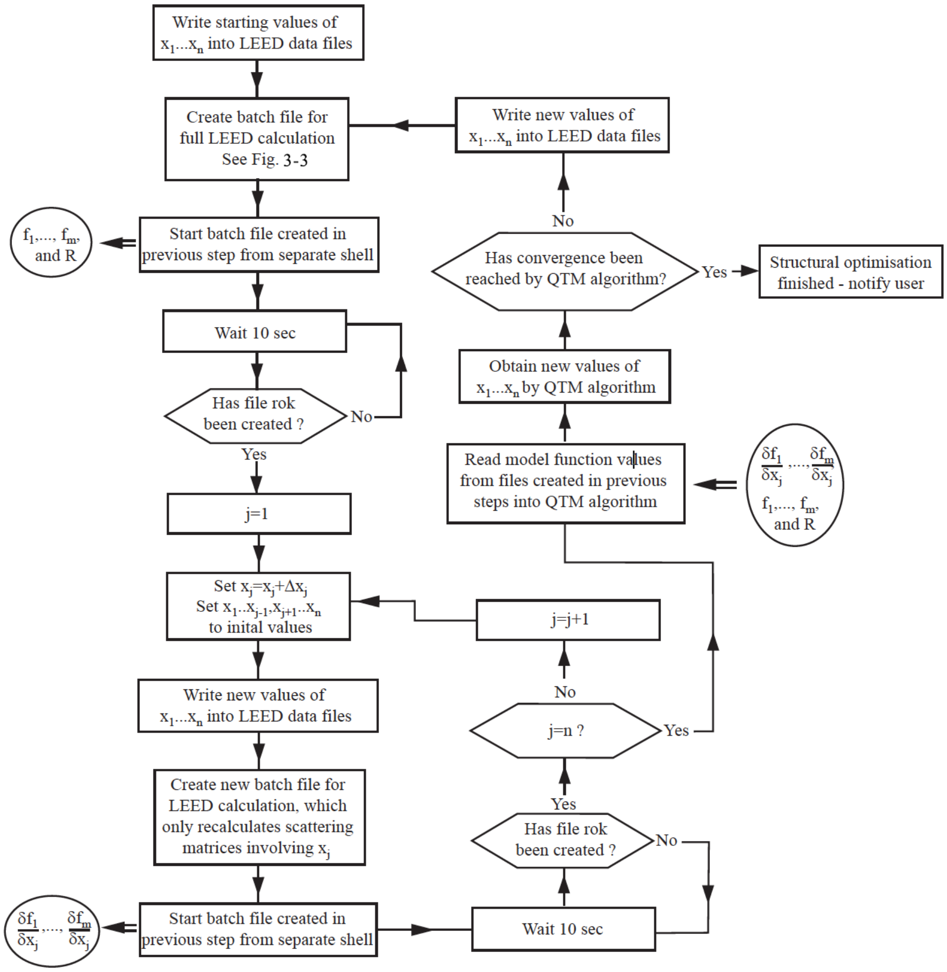

Figure 3-2: Flow diagram of LEEDopt optimization process. (Reproduced from Ref. [5])

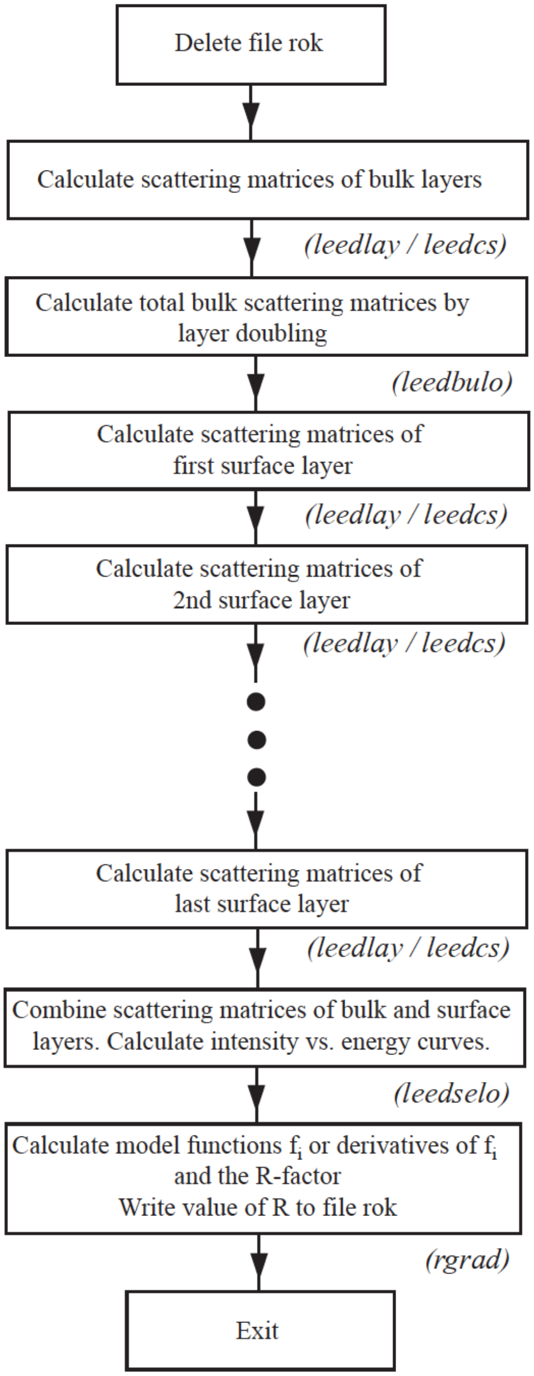

Figure 3-3: Flow diagram of full LEED-IV calculation. (Reproduced from Ref. [5])

3.2 Advancement of Dynamical LEED-IV Analysis

The LEEDopt package written by Adams *et. al.* has striking advantages over previous LEED codes. The package offers an automated search algorithm for the best-fit parameters. It has the ability to optimize multiple parameters at the same time and was proven to have a quicker convergence speed. Furthermore, the LEED-IV calculation codes included in the LEEDopt package were also rewritten in Fortran 90 using dynamical memory allocation, by Adams *et al.,* during the period from 1993 to 2000. This reduces the compiling complexity due to different matrix sizes of different calculations. However, LEEDopt was written in Visual Basic, a language discontinued by Microsoft, and it can be only run on Windows OS. This would introduce significant barrier for the programs' broader applications due to its difficulty of compiling and limited portability. One more critical issue is that the LEEDopt program could lose its power quickly when facing challenges for calculating composite layers with increasing number of subplanes, such as a large overlayer super lattice. The calculation time for the composite layers increases by a factor of N^3, where N is the number of subplanes in the composite layer. It becomes extremely time consuming and sometimes unrealistic to carry out the optimization for complex structures. Two challenges need to be conquered before enabling dynamical LEED theory's wider application in more complex surface structures. First, the composite layer calculation program, *leedcs*, need to be parallelized so that it can be carried out more efficiently and be able to handle bigger number of subplanes. Secondly, the LEEDopt program need to be rewritten in a more portable language across different operating systems so that the whole optimization scheme can be carried out on a super computer to make calculations for complex structures approachable. In the following two sections, I will present my approach to parallelizing *leedcs* using OpenMP and its performance improvement. Moreover, I will introduce my work of rewriting the parameter optimization part using Fortran and enabling easy compiling cross different operating systems, including its installation on the supercomputer Trillian (a single node of 32 cores is used), located at the University of New Hampshire. The optimization iteration process was also further simplified to improve its efficiency.

3.2.1 Parallelization of *leedcs*

The main calculation loop in the *leedcs* is the calculation for scattering matrix iterating through the range of incident electron energies, as shown in Fig. 3-4 (a). Each step of the matrix calculation that corresponds to an individual energy is relatively independent, thus is identified for parallelization. Although two main issues need to be addressed before the parallelization. First, the phase shift data needs to be read-in by *leedcs* for scattering matrix calculations. The phase shifts are calculated by programs developed by Van Hove [60], prior to *leedcs*. The phase shifts data are stored on the disk in the order of increasing energy steps, defined by the user. The phase shifts data are then read-in by *leedcs* within the energy loop. Corresponding phase shifts are read-in by *leedcs* at each energy step and used for scattering matrix calculation for the designated energy. When parallelized, different threads would have conflicts accessing the same input file at the same time. Second issue is the writing of the matrix file. The original *leedcs* code calculates the matrix data at each energy step and writes the matrix data into a single output file one line per energy step, in the same order as the energy. This would also introduce conflicts after parallelization when different threads try to write data into the same file at the same time. To realize the parallelization of the *leedcs* code, the part that reads in the phase shifts data is moved out of the energy loop to resolve the runtime conflicts. Then, the matrix writing part is decomposed and matrix data are written into different temporary matrix files for each energy step. All the temporary matrix files are read-in and assembled upon the completion of calculations for all of the energy steps. The final matrix file is compared to the matrix file

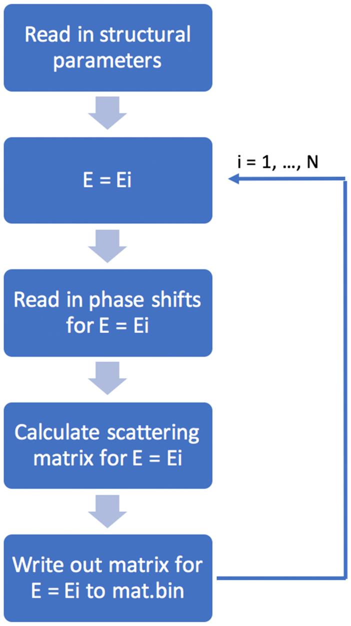

(a) Original *leedcs* calculation process

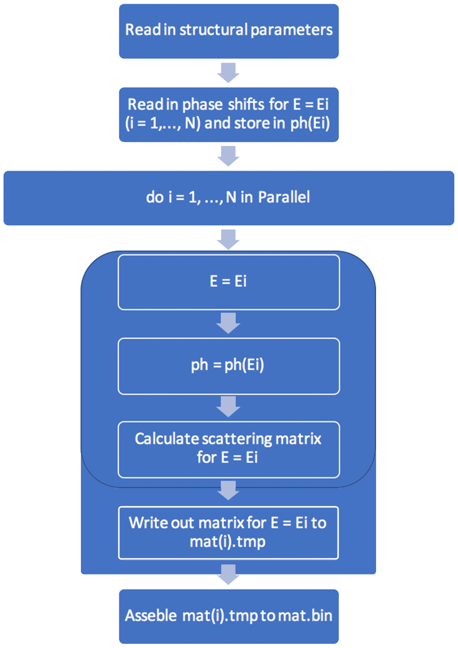

(b) Parallelized *leedcs* calculation process

Figure 3-4: Parallel *leedcs* calculation process compared with original process.

calculated by the original *leedcs* to ensure same results were achieved. The above explained difference of calculation process between original and parallelized *leedcs* is presented in Fig. 3-4.

The parallelized *leedcs* improved the efficiency by almost 14 times when run on the super computer, Trillian, using one node (32 cores). The improvement of speed using different number of cores is shown in Fig. 3-5. The improvement of performance is described using the ratio of calculation speed using N cores (v_N) versus calculation speed using just 1 core (v_1), as shown in Eq. 3.47. The improvement of performance is capped by the calculation time needed for the calculation for the highest energy. This is because the matrix calculation time increases with increasing incident energy as more diffracted beams are emerging at higher energies.

$$S = \frac{v_N}{v_1} \tag{3.47}$$

3.2.2 *pleedopt*: Enabling HPC for LEEDopt

pleedopt is a Fortran 90 program I developed based on the previously described Visual Basic code LEEDopt. The main function of *pleedopt* is similar to that of the original LEEDopt, but has a few advantages. *pleedopt* automatically optimizes multiple structural and non-structural parameters using the same rapid converging optimization algorithm, QTM. It is proven to converge and optimize to the same results if run on the same Operating System and compiler. Furthermore, *pleedopt* has much better portability compared to the original LEEDopt. Unlike the original LEEDopt, the new Fortran 90 program *pleedopt* is easy to be compiled with one click or one line command using the included $Makefile$ across different platforms. It can be installed on all Operating Systems. So far, it has been tested on Windows 7, Linux, and Mac OS. Due to its portability, it can be run on most modern

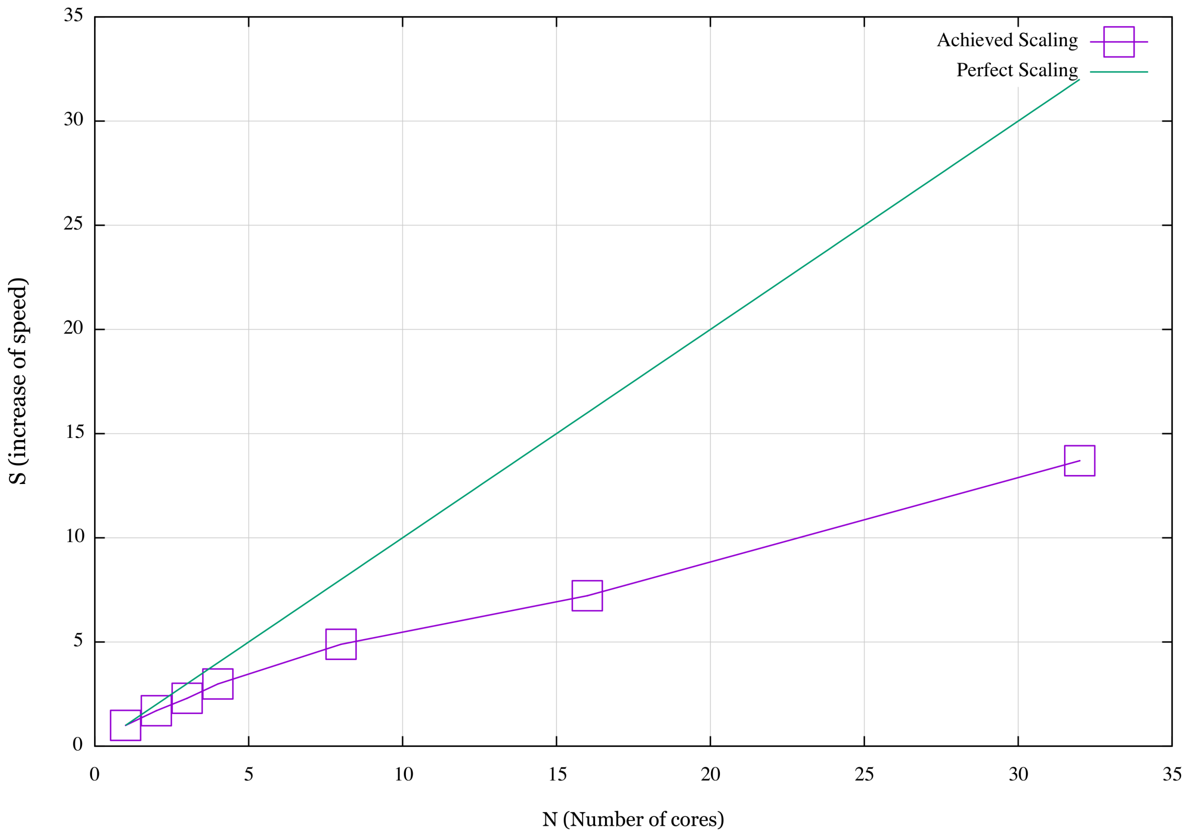

Figure 3-5: Improvement of performance after the parallelization of *leedcs*. X-axis is the number of cores used in the calculation and Y-axis is the ratio of calculation speed using different number of cores. Green line is the perfect scaling and purple line is the achieved performance improvement.

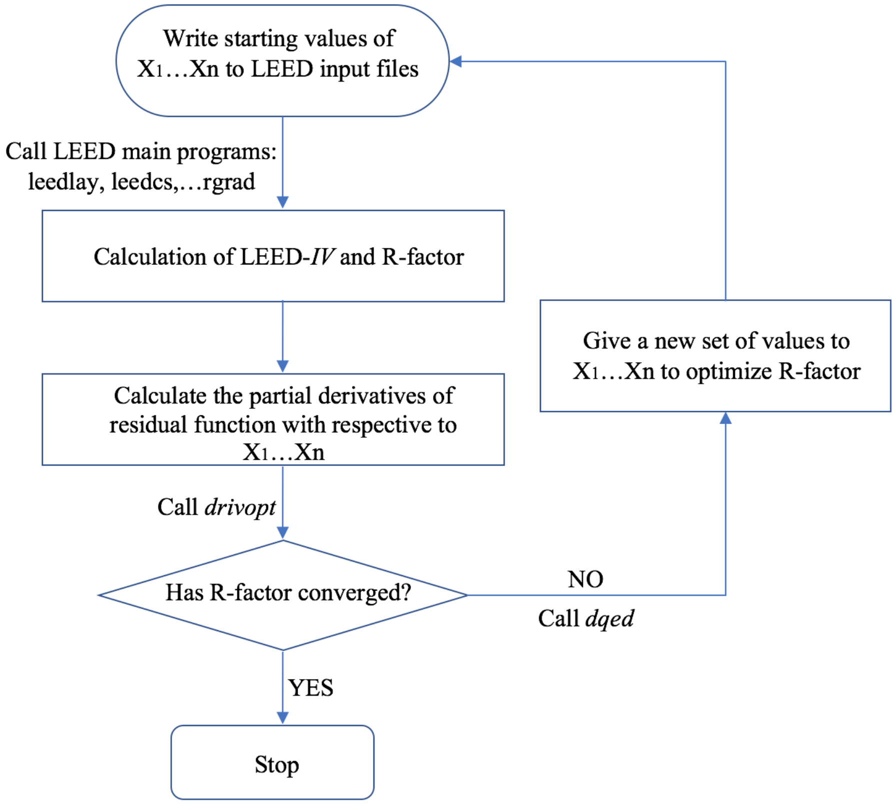

Figure 3-6: Flow diagram of *pleedopt*.

supercomputers to enable high performance computing (HPC) of the LEED-*IV* calculations. It has been tested successfully on the supercomputer Trillian at the University of New Hampshire. One more advantage of *pleedopt* is that it communicates with other Fortran 90 main LEED calculation programs more efficiently than the original Visual Basic code. The Visual Basic code uses a clocking function to wait for the result of the main programs and decides when to iterate or execute next step. It complicates the optimization process and it also wasted time on clocking and waiting. *pleedopt* does not need an outer loop clocking function to wait for the completion of the main programs. This helps to save more time in the optimization process.

A flow diagram describing *pleedopt* is shown in Fig. 3-6. At the start of the optimization, *pleedopt* reads in a set of structural and non-structural parameters that describes the proposed atomic model. The parameters are written into the input files for the main LEED calculation programs. *pleedopt* then launches a series of shell commands to run the main LEED calculation programs. *pleedopt* then reads in the R-factor, upon the completion of the full run of the LEED-IV and R-factor calculation. The gradient of the R-factor corresponding to small change around each parameter is then calculated and stored on the disk. The R-factor and the gradient information for each parameters are then all passed to program *drivopt*, which in turn calls *dqed*. *drivopt* judges if the R-factor has converged. If not converged, *drivopt* calls *dqed* to predict a new set of parameters for the next trial, using the calculated gradients of the R-factor information. Then new set of parameters are then written into the main input files again and a new iteration starts. *pleedopt* iterates automatically until a minimum of R-factor is achieved. The parameters at each iteration are all recored and written into a log file.

3.3 Multiple-angle Off-normal LEED-IV Experiment and Calculations of Cu(111)

The accuracy of structural determination through the dynamical LEED-IV relies heavily on the size of the experimental data set. The more energy points and more beams recorded in the experiment, the more accurate it is. However, the accessible energy range and beams are sometimes limited due to surface corrugation, limited sample size and strong inelastic scattering. LEED-IV data are usually taken under normal incidence condition. Taking LEED-IV data at multiple incident angles increases the size of the experimental data set and potentially increase the accuracy of the dynamical LEED-IV analysis. In this section, I present the surface structure determination using electron beam incident at different angles on the well known Cu(100) surface for testing of this method.

3.3.1 Experimental Procedure

The off-normal incident LEED experiments were carried out on IBM LEEM-II system, located at the IBM Watson Research Center. The data were collected by collaborators, Dr. Meifang Li and Dr. James B Hannon. Details about the experimental set up can be found in Ref. [2]. The intensity of the diffracted (00) beam was recorded for the energy range from 20 to 45 eV, with increment of 1 eV. The azimuthal angle ϕ was kept at 45°, while the polar angle θ was tuned to collect (00) beam intensity data along the $\overline{\Gamma \mathrm{M}}$ direction in the momentum space, as shown in Fig. 3-7. The (00) beam intensity versus the incoming electron energy (E) and parallel component of the electron momentum ($k_{||}$) is plotted in Fig. 3.8(a).

3.3.2 Calculation Details

The phase shifts were calculated with Van Hove's calculation package [60]. The lattice constant used in the calculation is $a = 3.621$ Å, which was acquired from the LEED experiment. The temperature used in the calculation is 478 K and the Debye temperature is 315 K [61]. The energy-dependent inner potential $V_0(E)$ is used in the calculation, as shown in Eq. (3.48) [61].

$$V_0(E) = \begin{cases} -13.4 & when \;\; E \leq 36 \; eV \\ -3.6 - 65.8/\sqrt{E + 10.0} & when \;\; E > 36 \; eV \end{cases} \tag{3.48}$$

The azimuthal angle ϕ was fixed at 45° while θ was varied from -50° to 50°, with 1° increment. The calculated data is transformed into momentum space using Eq. 3.49. The calculated results are then compared to the experimental data to optimize the surface structure.

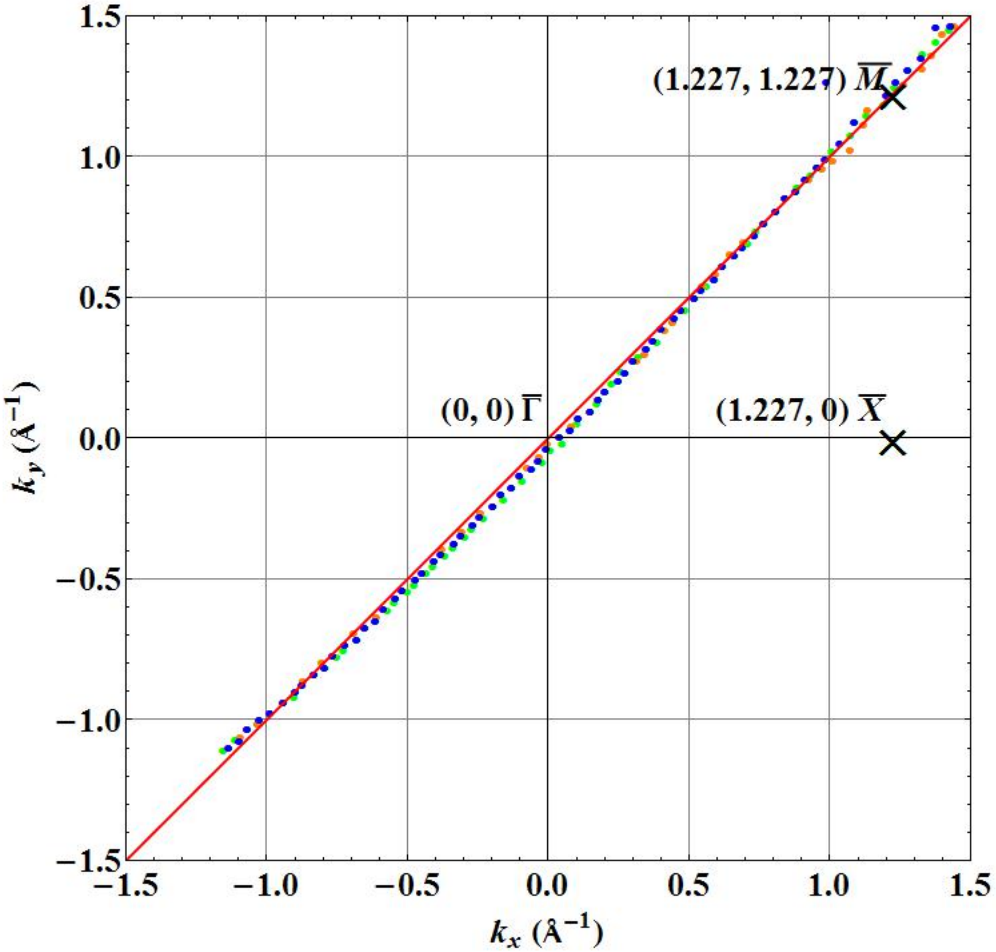

Figure 3-7: Distribution of experimental data k points. Green dots are the grid of k points for $E = 45$ eV, which was used in the calculation. The blue and orange dots are the grids for $E = 22$ eV and $E = 32$ eV respectively.

Parameters	Starting values	Optimized values	Sun's values	$\Delta d/d^b(\%)$				
				This work	Sun's work	Ref.2	Ref.3	Ref.4
d_{12} (Å)	1.811	1.781	1.78±0.016	-1.66	-1.6±0.9	-1.0±0.4	-1.2	-2.4
d_{23} (Å)	1.811	1.816	1.83±0.016	+0.28	+1.0±1.8	+1.7±0.6	+0.9	+0.9
u_1 (Å)	0.182	0.195	0.27±0.020					
u_2 (Å)	0.182	0.269	0.19±0.017					
V_{damp}	0.80	0.845	0.92±0.07					
ΔV_0 (eV)	0	0.979	1.02±0.31					
R factor	0.0784	0.054	0.066					

Table 3.1: Optimized Structural parameter Results.

$$k_{||} = \sqrt{2mE} \cdot \sin\theta \tag{3.49}$$

3.3.3 Results

As shown in Fig. 3.8(a) and Fig. 3.8(b), the calculation results with optimized structure match with experimental data very well. The agreement is better visualized in Fig. 3.8(c), which is the overlap of the experimental and calculation results. The experimental data with the range of $k_{||}$ = -1.32 Å^{-1} to 1.32 Å^{-1} are used for structural optimization. The optimized R-factor is 0.054. The optimized structural parameters are presented in Table 3.1 along with results from Sun's work [61] and other references [62] [63] [64]. The optimized structural results are in good consistency with previous results regarding the Cu(100) surface. The first layer spacing is contracted slightly by about 1.6% and the second layer spacing is expanded slightly by about 0.3%, comparing to the bulk values.

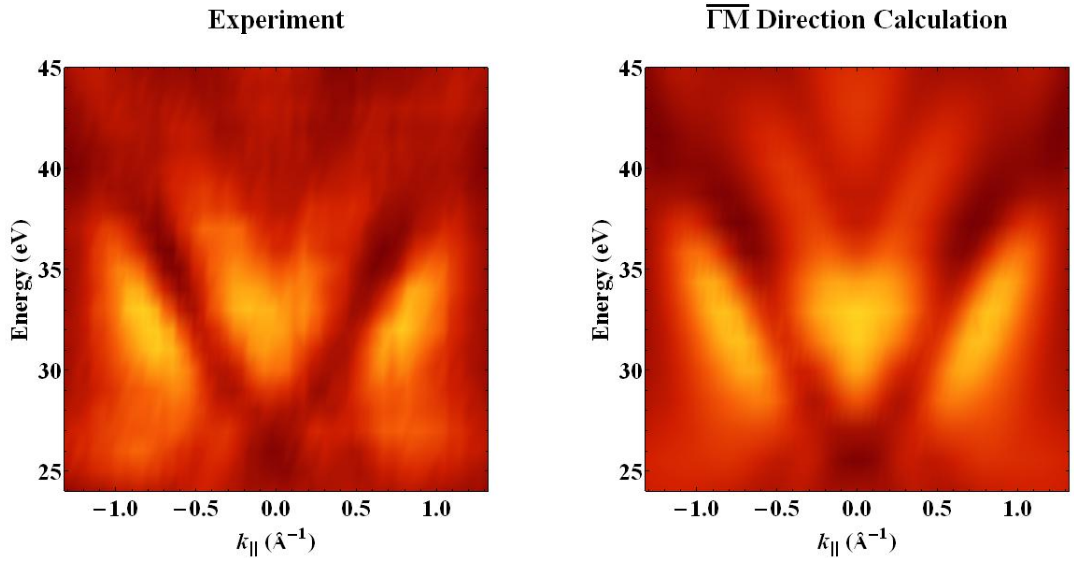

Experiment

$\overline{\Gamma M}$ Direction Calculation

(a) Experiment

(b) Calculation

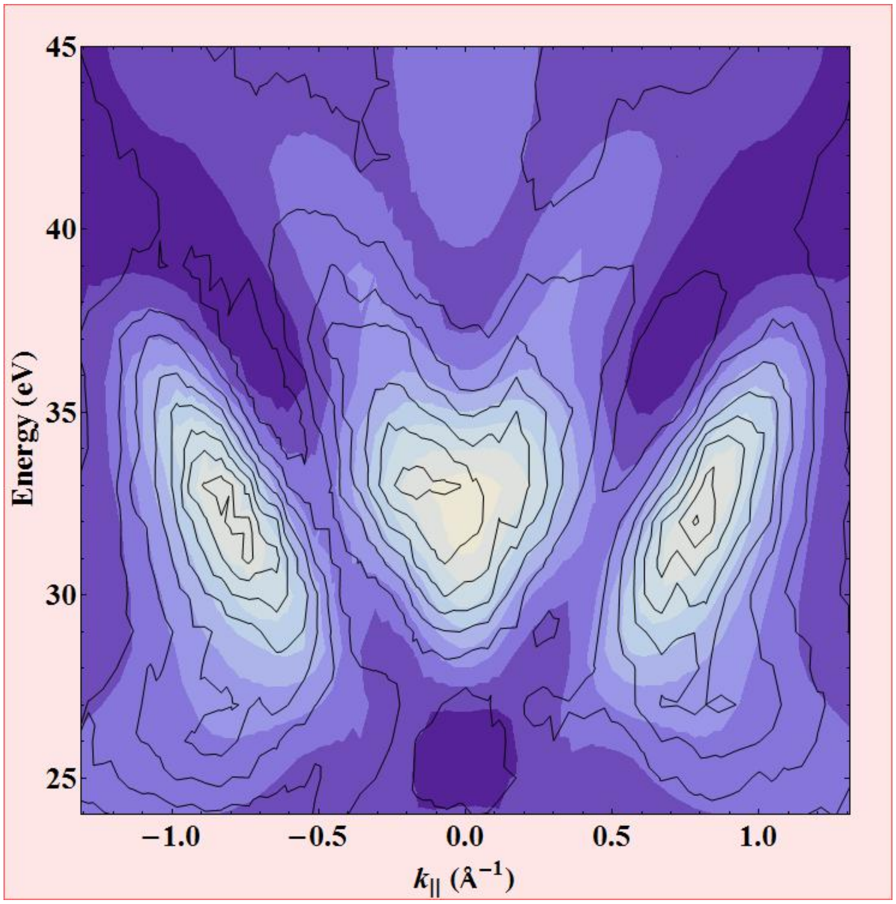

(c) Overlap of experimental and calculational results. Blue shaded area is based on the calculation, line contour on the experiment.

Figure 3-8: Experiment and $\overline{\Gamma M}$ direction calculation result.

3.3.4 Mapping of Electron Reflectivity within First Brillouin Zone

2D scanning of the diffraction intensity of (00) beam within the first Brillouin zone was carried out at fixed incident electron energy, E=36 eV. The calculation was carried out using previously optimized structural parameters. The calculated results match very well with the experimental data, as shown in Fig. 3-9.

3.3.5 Discussion

The proposed multiple-angle off-normal incident experiments and dynamical calculations were proven to produce similar optimized surface structural results as conventional LEED-IV analysis. Even with a much shorter energy range, the extra information provided by the data collected at a series of off-normal incident angle does ensure the optimization is converged correctly. However, the non-structural parameters, atomic thermal vibration amplitudes for the surface layers, (u_1, u_2) did not agree well with Sun's previous results [61]. This is likely due to the shorter energy range in this study. The collected data covers the energy range of 22 to 45 eV, comparing to conventional LEED-IV range of $\sim$ 20 eV to $\sim$ 400 eV and Sun's LEEM-IV range of 20 to 100 eV. Figure 3-10 shows the calculated (00) beam IV curves at normal incidence for using both Sun's structure and this work's, comparing with the experimental data in the corresponding studies. Both the peak position and shape match very well with the experimental data within the energy range of 24-40 eV. However, in this study, the collected energy range does not cover the whole second peak width, which is located at around 40 eV-50 eV. The difference in the optimized surface vibration amplitudes in Sun's study [61], are likely the results of fitting of the second peak at around 40-50 eV. Since the peak position is the dominant factor to quantify the agreement between the calculated and experiment, a minimum of two peaks might be needed for a more accurate determination of the non-structural parameters such

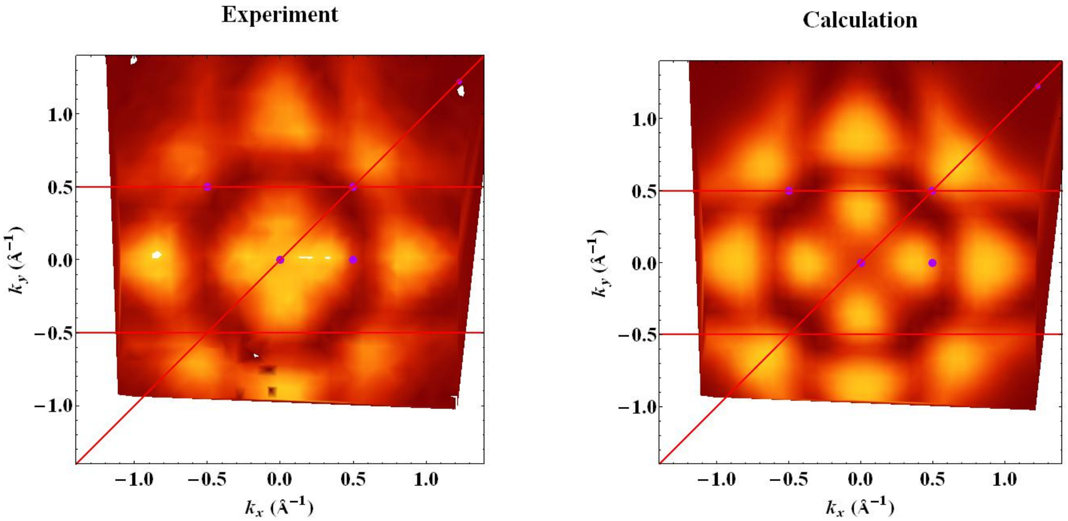

(a) Experiment

(b) Calculation

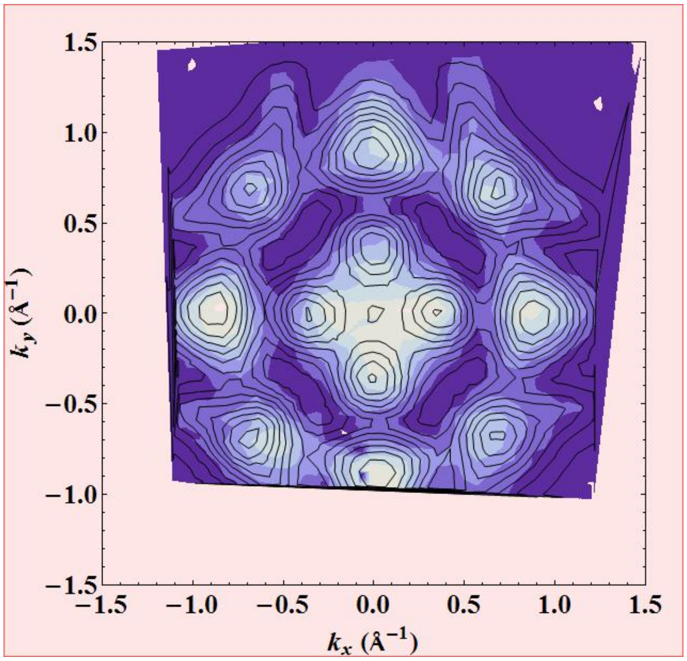

(c) Overlap of experimental and calculational results. Blue shaded area is calculation, line contour is experiment.

Figure 3-9: Single energy $E = 36$ eV experimental and calculational results.

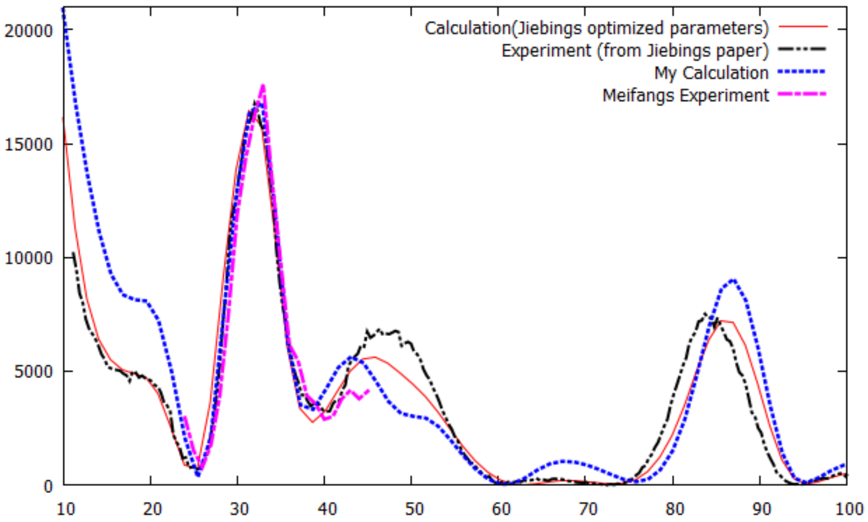

Figure 3-10: (00) beam I-V curves for normal incidence. Red is Sun's calculation, green is this work's and blue is Sun's experiment result.

as surface thermal vibrations. Specifically, for the presented study of Cu(100), it may need to extend the experimental energy range up to 55 eV or higher. Even though partial success is achieved, further investigation of this method is still needed.

CHAPTER 4

STRUCTURE OF BULK 2H-MoS$_2$(0001) SURFACE AND MONOLAYER MoS$_2$

4.1 Introduction

Molybdenum disulfide (MoS$_2$), a layered transition metal dichalcogenide, is an indirect-gap semiconductor with an optical band gap matching well with the solar spectrum [65]. Due to this important property, it may be used for electrodes in high efficiency photoelectrochemical (PEC) cells [33]. MoS$_2$ has three common polytypes: 1T-MoS$_2$, 2H-MoS$_2$ and 3R-MoS$_2$. The 2H-MoS$_2$ polytype is the most stable configuration [66]. The present study has investigated 2H-MoS$_2$; its crystal structure is shown in Fig. 4-1. MoS$_2$ consists of covalently bonded S-Mo-S sandwich layers. The unit cell of bulk 2H-MoS$_2$ contains of two symmetrically inequivalent S-Mo-S sandwich layers. Each sandwich layer is characterized by strong intralayer covalent bonding, whereas the sandwich layers bond to each other via weak interlayer van der Waals' forces. While the electronic structure [67, 68, 69] and crystal structure [70, 71] of bulk MoS$_2$ have been studied extensively, there have been very few studies on the surface structure. The only low energy electron diffraction (LEED-IV) study was conducted by Van Hove *et al.*, which reported that the surface remained mostly unchanged from its bulk structure except that the first interlayer spacing is contracted by 4.7% and the first sandwich interlayer spacing is contracted by 3% at the temperature of 95 K [6, 72]. This study assumed the second interlayer spacing remained unchanged from that of bulk MoS_2 [6]. A coaxial impact-collision ion scattering spectroscopy (CAICISS) study reported that the first interlayer spacing has a contraction of 3.6% while the second interlayer spacing has an estimated contraction of 0 to 2% at room temperature [73]. However the CAICISS study was only able to determine the first two interlayer spacings and the second interlayer spacing was not accurately determined [73]. The goal of the work presented in this chapter is to determine the surface structure of this important photovoltaic material at an elevated temperature of 320 K using μLEED-IV analysis.

Monolayer MoS_2 can be prepared through mechanical exfoliation from bulk MoS_2 [74] and it has very different electronic properties compared to crystalline MoS_2 [19]. Most striking is the transition from an indirect to direct band gap semiconductor behavior when going from bulk to monolayer [75]. Due to its unique properties, monolayer MoS_2 has been suggested to be an ideal candidate for applications in atomically thin, layered electronics [31, 76], optical [77, 78], and photovoltaic [32] devices. Thus it is essential to know the atomic structure of monolayer MoS_2 in order to better understand its properties and provide guidance to its applications. For monolayer MoS_2, the absence of interlayer interaction and the presence of substrate interaction may lead to crystalline structure distortion. The scotch-tape method for exfoliation of monolayer and transfer method may also cause surface morphology roughness. As a result, these changes on the surface may modify its important properties. Therefore, the preservation of its intrinsic properties is crucial to the potential applications of monolayer MoS_2. Various aspects of monolayer MoS_2, including electronics, optics, spintronics, and valleytronics, have been extensively investigated; however, the number of studies of the atomic structure, especially surface structure is quite limited. Here, we study the atomic structure of monolayer MoS_2 in two systems: the surface of bulk 2H-

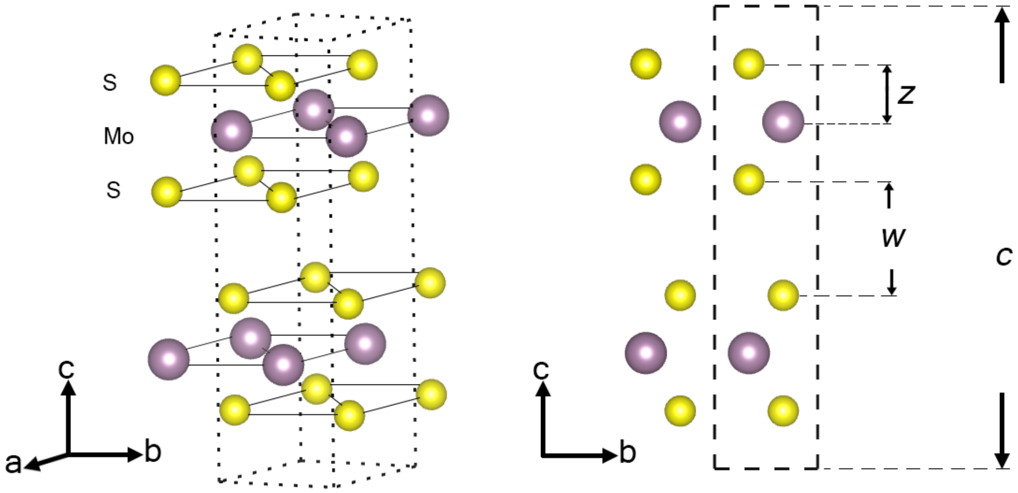

(a) Crystal structure (b) Side view

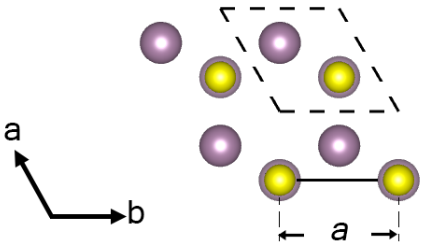

(c) Top view

Figure 4-1: Crystal structure of 2H-MoS_2, dashed quadrangular prism indicates the unit cell. $a = 3.16$ Å, $z = 1.593$ Å, $w = 2.959$ Å [6].

MoS_2, which is a good approximation of an isolated monolayer, due to the natural break in the perpendicular periodicity and the weak van der Waals interaction with the bulk underneath, and the suspended monolayer MoS_2. To date, there has been no detailed study of the atomic structure of the monolayer MoS_2. In the work presented in this chapter, I have used μLEED with a small sampling areas of 5 μm diameter, combined with dynamical LEED-IV analysis, to investigate the atomic structure of monolayer MoS_2. The bulk MoS_2 sample and suspended monolayer sample are prepared by collaborators from Columbia University and the LEEM/μLEED-IV data were collected by collaborators from Brookhaven National Lab.

4.2 Experimental Methods

Large multiple layer MoS_2 flakes (lateral dimension $> 10\mu$m) were mechanically exfoliated and transferred onto a Si wafer with poly(methyl methacrylate) (PMMA) and polyvinyl alcohol (PVA) overlayers using the methods detailed in [75, 79]. The MoS_2 flakes were characterized using optical microscopy and their thickness was also determined using Raman [80] and photoluminescence spectroscopy [81]. Thick MoS_2 flakes ($>$ 100 layers) of about 10 μm diameter were prepared, as shown in Fig. 4.2(a), and considered equivalent to bulk MoS_2. Prior to measurements, the samples were annealed at 350°C for 6 hours in ultrahigh vacuum to remove contaminants. Our experiment was carried out on the Spectroscopic Low Energy Electron Microscope (SPE-LEEM) system at the National Synchrotron Light Source beamline U5UA. LEEM was used to locate the sample area of interest, as shown in Fig. 4.2(a). Subsequently, the crystalline structure of the sample was investigated using μLEED with a 5 μm sampling area. μLEED of monolayer (1 ML), bilayer (2 ML), trilayer (3 ML) and bulk MoS_2 (more than 100 layers thick) flakes shows well-defined hexagonal patterns with 3-fold symmetry (see Fig. 4-2). The linewidth of the μLEED spots increases with decreasing sample thickness (see Fig. 4-3(a)). This phenomenon is attributed to the surface corrugation induced by the interaction with the substrate [74, 79]. The surface corrugation (roughness) can be further quantitatively characterized using the model $\Delta\theta=\Delta k_{||}/2k_0$ [82, 83], where $\Delta\theta$ is the standard deviation of the local surface normal, $\Delta k_{||}$ is the linewidth of the central diffraction spots (denoted as (00) beam), and $k_0=\sqrt{2m_e E_{kin}}$ is the incident electron momentum.

We performed *in situ* intensity *vs.* voltage measurements in reciprocal space (LEED-IV). Data were collected using a normal incident electron beam with energy ranging from 25-150 eV. As shown in Fig. 4-3(b), the linewidth of the diffraction spots increase linearly with k_0. In addition, the magnitude of surface roughness of 1 ML MoS_2 is strikingly large in comparison with 2-3 ML and bulk MoS_2, indicating a strong substrate interaction. Figure 4.2(c), 4.2(d) and 4.2(e) show the LEED patterns of bulk MoS_2 acquired at 40 eV, 78 eV, and 95 eV, respectively.

I combined μLEED-IV measurements with dynamical LEED calculations to determine the atomic surface structure. In our LEED-IV curves, the intensity of (01) and (10) beam is the average intensity of the three symmetrically equivalent diffraction spots denoted as A and B in Fig. 4.2(c), respectively. The averaging procedure seeks to minimize the intensity anisotropy of the diffraction beam due to small sample tilting ($< 0.1°$). The background intensity was subtracted from the scattered beam intensity.

To obtain suspended MoS_2, we fabricated the substrate by patterning cylindrical cavities (2 or 5 μm in diameter and 1 μm in depth) on an n-doped Si wafer with native oxide using lithography and etching. Subsequently, the monolayer MoS_2 flake was transferred onto the patterned substrate using the same transfer method as used for bulk MoS_2 flakes. As a result, we obtain suspended monolayer MoS_2 over the cavity regions. The different electron reflectivity of suspended and supported monolayer MoS_2 and the substrate exhibit clear

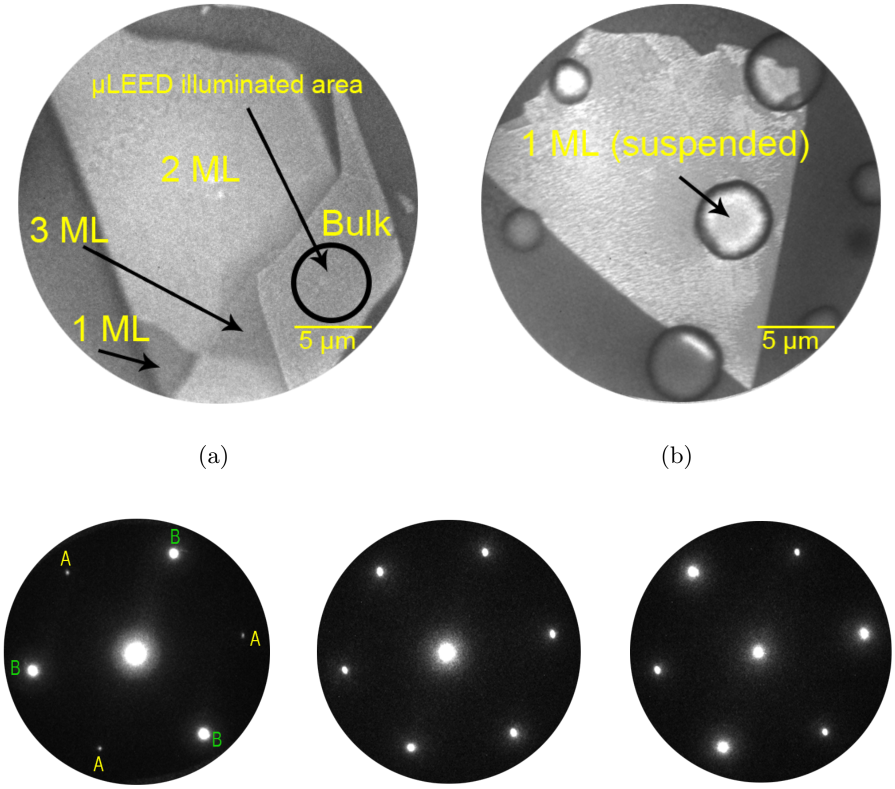

(a)

(b)

(c)

(d)

(e)

Figure 4-2: (a) LEEM image of bulk, 1 ML, 2 ML and 3 ML MoS_2 on Si substrate; (b) 1 ML suspended MoS_2; μLEED patterns of bulk MoS_2 acquired at (c) 40 eV, (d) 78 eV, and (e) 95 eV, respectively. Note that (c) and (e) clearly display 3-fold symmetry.

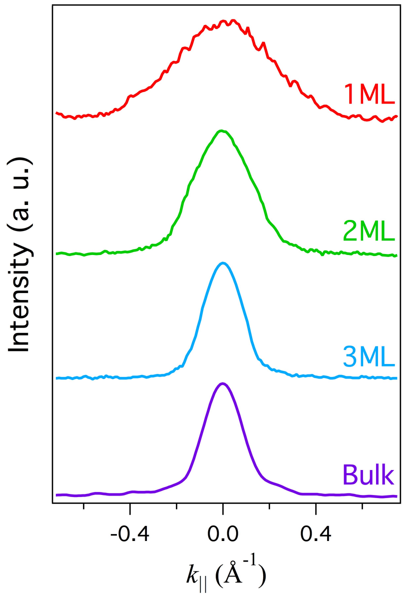

(a)

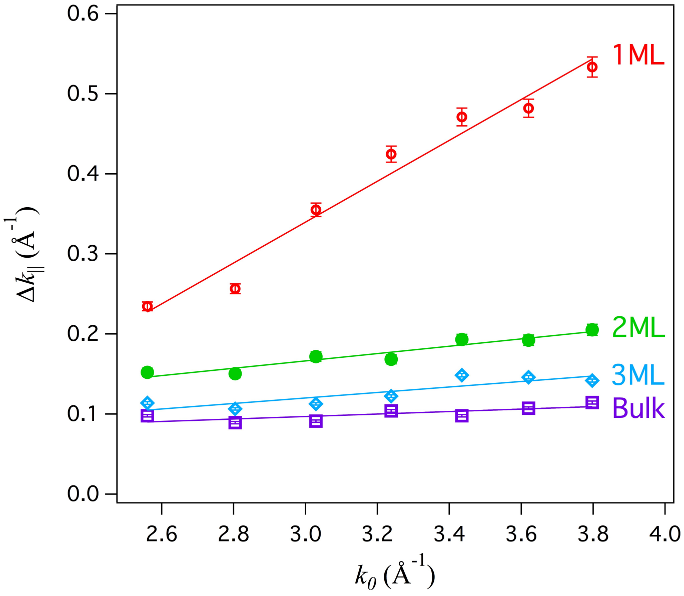

(b)

Figure 4-3: (a) Intensity profiles of the (00) diffraction beam of 1-3 ML and bulk MoS2. (b) Linewidth of the (00) diffraction beam as a function of k_0, k_0=$\sqrt{2m_e E_{kin}}$

.

contrast, as shown in Fig. 4.2(b). This allows us to carry out μLEED measurements at the regions of interest; LEED-IV of six first order diffracted beams (three (10) beams and three (01) beams) for the energy range of 25-100 eV were extracted from the experiment. The (00) beam was too diffuse to extract IV data; this is likely due to reflection from the edges of the cavity.

4.3 Calculation Details

I performed the dynamical LEED-IV analysis of our μLEED data collected by LEEM from the bulk MoS_2 flake and the suspended monolayer MoS_2. I used Adams' LEEDopt package described in Section 3.1 of Chapter 3 for structural optimization. The relative intensities of diffraction beams are preserved during the optimization. The phase shifts (a quantity describing the atomic scattering property [58]) were calculated using the Barbieri/Van Hove phase shift calculation package [60]. The muffin-tin radii for Mo atom and S atom are set to $r_{Mo}^{MT} = 2.4598$ a.u. and $r_{S}^{MT} = 2.1084$ a.u., respectively. 12 phase shifts (L = 11) were used for the LEED-IV calculation. The in-plane lattice constant was $a = 3.16$ Å, the Mo and S atomic layer distance was $z = 1.593$ Å and the layer distance between the S-Mo-S sandwich layers was $w = 2.959$ Å for the bulk, as indicated in Fig. 4.1(b) [6]. The interlayer spacing between the ith and jth surface atomic layer is indicated as d_{ij}. The optimized structural parameters are the first three interlayer spacings (d_{12}, d_{23} and d_{34}) for bulk MoS_2 and the first two interlayer spacings (d_{12} and d_{23}) for the suspended monolayer MoS_2. These spacings are adjusted to give the best agreement with the measured IV curves. The R_2 factor (see Eq. 3.42) is employed to quantify the agreement level between the experimental and theoretical data [84]. The error bars in the surface structure analysis are based on an increase of 4% in the R_2 factor [61].

The mean-square atomic vibrational displacements $\langle u^2 \rangle_T$ for Mo and S were calculated individually according to the relation between Debye temperature θ_D and $\langle u^2 \rangle_T$ at the sample temperature T (320 K) using Eq. 3.7 in Chapter 3. Two Debye temperatures θ_D were tested for MoS_2: 350 K [6] and 600 K [85]. The inner potential, $V_0 + iV_{im}$, was set to be independent of energy. The real part V_0 was initially set to be 8 eV and adjusted through ΔV_0 (the decrease in V_0) during the fitting process and the imaginary part V_{im} was set to be 6 eV.

4.4 Results and Discussions

Among the two Debye temperatures θ_D we examined (350 K and 600 K), $\theta_D = 600$ K shows a slightly better agreement between the calculated *IV* curves and the experiment, which agrees with a previous study [85] that found that the Debye temperature increases and approaches a constant as temperature increases for layered materials. Specifically, the Debye temperature of MoS_2 approaches 600 K when the temperature rises above room temperature. Another neutron scattering study reported that the high-temperature Debye temperature is almost twice as large as that of zero temperature [86]. This behavior seems to be common to materials that have large c-lattice constants and extremely weak interlayer interactions.

To refine the surface atomic structure, the structure was relaxed and a search for small variations compared to the bulk was carried out. Fig. 4-4 shows heat maps of the R_2 factor as a function of the surface structural parameters d_{12} and d_{13} for bulk MoS_2 surface (left) and suspended monolayer MoS_2 (right). It clearly shows a well-defined R_2 factor minimum for both cases. Best-fit structural parameter values are listed in Table 4.1 and compared with previously reported results [6, 72, 73]. Surface interlayer spacings are also compared with the bulk values and the difference between them is denoted as Δd_{ij}. Comparisons of experimental to calculated *IV* curves are shown in Fig. 4-5. Small R_2 factors [84] of 0.086

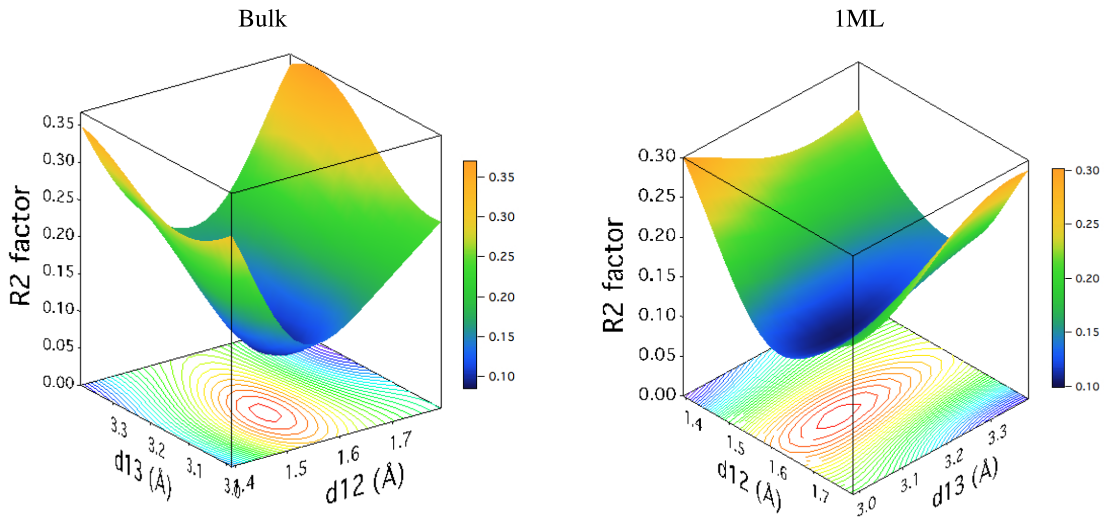

Figure 4-4: Heat maps of the R_2 factor as a function of surface structural parameters d_{12} and d_{13} for bulk MoS_2 (left) and suspended monolayer MoS_2 (right).

and 0.102 were achieved for bulk MoS_2 and monolayer, respectively. This indicates good agreement between the calculated and experimental IV curves for both samples, as shown in Fig. 4-5. The optimized bulk MoS_2 structural results show that the topmost interplanar spacing d_{12} has a smaller contraction of 2.5±1.9% from its bulk value at 320 K, compared with a contraction of 4.7% at 95 K [6, 72]. The second interplanar spacing d_{23} contracted by 1.3±2.5%. The first vdW (van der Waals) gap shows an expansion of 1.3±2.7% at 320 K from its bulk value instead of a contraction of 3% at 95 K [6, 72]. Since we fabricated MoS_2 flakes with high-quality surfaces, the differences of the surface structures between this work and previous studies [6, 72] is less likely due to the different preparation methods. We attempt to attribute the difference to thermal expansion of 2H-MoS_2 [87, 88] at elevated temperature in our measurement.

Based on the dynamical calculations and optimized results, the suspended monolayer MoS_2 has a slightly different structure compared to the S-Mo-S sandwich layer terminating the bulk surface. The first interlayer spacing d_{12} is slightly expanded by 1.3±1.9% compared to the bulk value while the second interlayer spacing d_{23} is contracted by 5.1±3.8% compared to the bulk value, as presented in Table 4.1. For an isolated monolayer of MoS_2, one would expect that the two layer spacings, d_{12} and d_{23} to be identical, since the molybdenum layer is centered between the two sulfur layers, as in the bulk crystalline structure. The slight asymmetry of the interlayer spacings might be caused by a small amount of warping or strain [74] of the suspended monolayer. Due to the limited sample size, shorter energy range of 25-100 eV and only six accessible beams for monolayer MoS_2, our conclusion for the atomic structure of the monolayer MoS_2 is potentially less reliable than the bulk MoS_2 surface structure results. The observed slight increase in the thickness of the topmost S-Mo-S sandwich layer of bulk MoS_2, d_{13}=3.13±0.04 Å, as well as suspended monolayer MoS_2, d_{13}=3.13±0.06 Å, at 320 K compared to previous result for the bulk surface at 95 K, d_{13}=3.11 Å, is not significant within our error bars.

There is a systematic disagreement between the calculated IV curves and the measured ones at the energy range between 50-60 eV while the calculations produced the main features of the measured IV curves over the rest of the energy range, see Fig. 4-5. We attribute this discrepancy to the strong back scattering of the electrons from the substrate and the sample flake boundary at this energy range. This was confirmed by observation of an unexpected peak at the range of 50-60 eV in the background IV curve.

Table 4.1: Optimum parameter values for the surface structure of 2H-MoS_2(0001)

Model	T	d_{12} (Å) ($\Delta d_{12}/z$)	d_{23} (Å) ($\Delta d_{23}/z$)	d_{13} (Å) ($\Delta d_{13}/2z$)	d_{34} (Å) ($\Delta d_{34}/w$)
Ref. [6, 72] (Bulk MoS_2)	95 K	1.518 (−4.7%)	1.593 (fixed bulk value)	3.111 (-2.4%)	2.877 (−2.8%)
Ref. [73] (Bulk MoS_2)	300 K	1.536 (−3.6%)	1.561 ∼ 1.593 (−2% ∼ 0%)	3.097 ∼ 3.129 (−2.8% ∼ −1.8%)	N. A.
This work (Bulk MoS_2)	320 K	1.553±0.03 (−2.5±1.9%)	1.573±0.04 (-1.3±2.5%)	3.126±0.04 (-1.9±1.3%)	2.99±0.08 (+1.3±2.7%)
This work (Monolayer)	320 K	1.613±0.03 (+1.3±1.9%)	1.513±0.06 (-5.1±3.8%)	3.126±0.06 (-1.9±1.9%)	N. A.

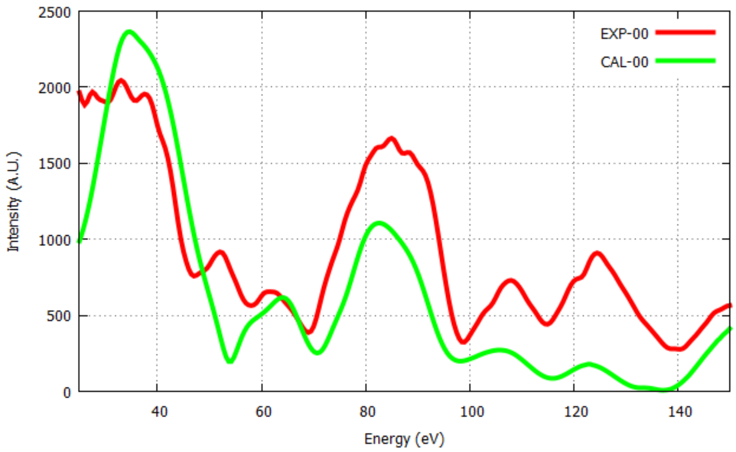

(a) (00) beam, bulk 2H-MoS$_2$

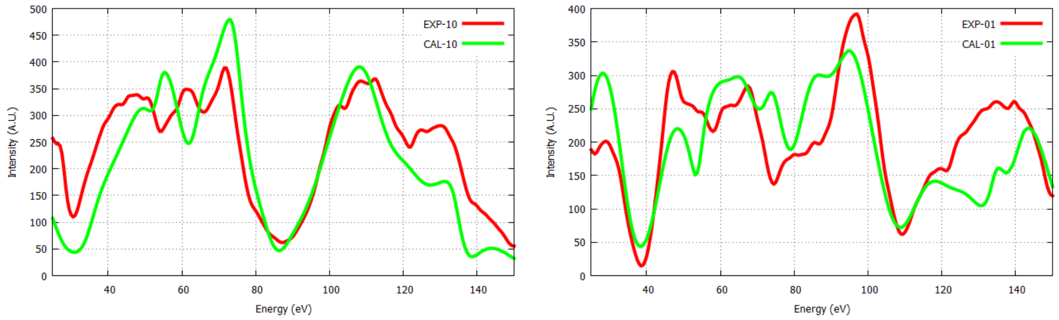

(b) (10) beam, bulk 2H-MoS$_2$

(c) (01) beam, bulk 2H-MoS$_2$

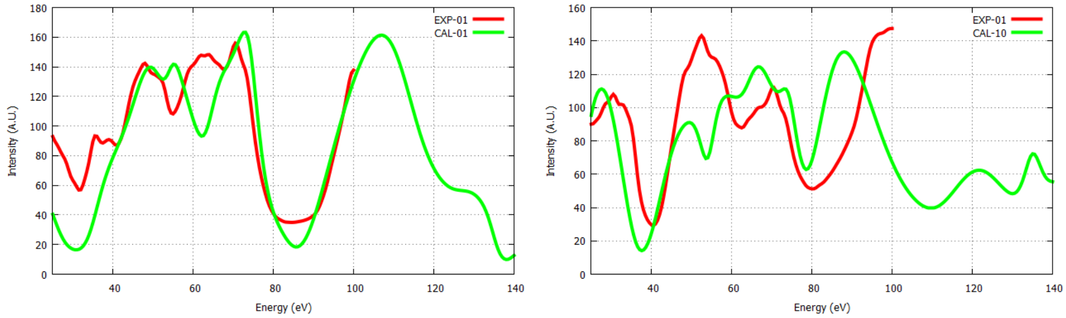

(d) (10) beam, monolayer MoS$_2$

(e) (01) beam, monolayer MoS$_2$

Figure 4-5: Comparison of experimental and calculated *I*-*V* curves for bulk 2H-MoS$_2$ and suspended monolayer MoS$_2$ for measured diffraction spots.

4.5 Conclusions

In conclusion, I showed that dynamical μLEED-IV analysis is a potentially powerful candidate for determination of the atomic structure of 2D materials. We concluded that at a sample temperature of 320 K, the Debye temperature of MoS_2 was about 600 K, which agrees with a previous study [85]. Good agreement was achieved between the measured IV curves and calculated IV curves for both the surface of the bulk MoS_2 and monolayer MoS_2. Our work also showed that the surface structure of bulk 2H-MoS_2 is distinct from its bulk crystalline structure and the surface structure is different at 320 K from its structure at 95 K due to thermal surface expansion. The interlayer spacing between the very top S atomic layer and the first Mo layer, d_{12}, has a smaller contraction of 2.5% at 320 K than at 95 K. The layer spacing between the first Mo atomic layer and the second S layer, d_{23}, has a small contraction of 1.3% from the bulk. We also showed that the layer spacing between the first S-Mo-S sandwich layer and the second sandwich layer, d_{34}, has an small expansion of 1.3% at 320 K compared to a contraction at 95 K. Finally we have concluded with less certainty, that the suspended monolayer MoS_2 has a large interlayer relaxation compared to the S-Mo-S sandwich layer terminating the bulk surface: d_{12} is expanded by 1.3% and d_{34} is contracted by 5.1% compared to the respective bulk value.

Chapter 5

Surface buckling of black phosphorus and few-layer phosphorene

5.1 Introduction

Black phosphorus (BP), together with its monolayer version known as phosphorene, has had a recent rebirth as a new member of the vigorously studied two-dimensional (2D) materials family. It has attracted much attention due to its intriguing potential applications for modern electronics [35, 36, 37, 38] and photonics [39, 40]. For example, BP exhibits an intrinsic layer-dependent bandgap ranging from 0.3 eV (bulk) to 2 eV (monolayer) [34], and thus bridges the energy gap between graphene and transition metal dichalcogenides (TMDs) [89]. This strong layer-dependence presents the potential for integrated devices on a single supporting platform. Despite the surge of research in the applications of BP, much remains to be learned of its basic physical properties both from a device and a fundamental physics perspective. For example, the origin of the previously measured intrinsic p-type nature of BP is unknown [35, 37]; and existing first-principles calculations could not completely explain measured band structures of BP [90, 91]. The electronic properties are inherently related to the atomic crystal structures; and when thinned down to few-layer form, the surface structures play an important role in the electronic properties of 2D materials.

However, to date, there is no consensus on the atomic structure of the surface region of BP. The crystal structure of BP, as shown in Fig. 5-1, has a puckered honeycomb structure similar to that of graphene [92]. Two previous STM studies of phosphorene [93, 94] have revealed important aspects of the BP surface topography and observed an apparent height difference between two symmetrically equivalent atoms P_1 and P_2, as illustrated in Fig. 5-1(d). While these STM measurements were not able to quantify the geometrical height difference between P_1 and P_2, denoted as surface buckling, these studies proposed very small surface buckling values, 0.02 Å [93] and 0.06 Å [94], based on their first-principles calculations. In order to experimentally resolve the surface atomic structure of BP, two main challenges for the characterization technique have to be overcome: it has to be (*i*) non-destructive and sensitive to the 3D atomic structure in the first few layers, and (*ii*) able to restrict the lateral sampling area to a few μm because many 2D materials including phosphorene are commonly prepared as small flakes. Here, selected area micro-spot low energy electron diffraction (μLEED) in a low energy electron microscope (LEEM), combined with dynamical intensity versus incoming electron energy (LEED-IV) calculations, is one of the very few practical techniques able to determine the 3D surface structure and composition of 2D materials with atomic resolution [41, 43, 95, 61, 96].

In this chapter, I present the first detailed experimental atomic surface structure determination of BP. We produce pristine BP surfaces by controlled evaporation of the surface oxide layers. LEEM and dynamical μLEED-IV analysis are employed to examine the in-situ cleaved bulk BP surface and mechanically exfoliated few-layer phosphorene (FLP) flakes of about 10 nm thickness. These measurements indicate that the surface buckling for the two studied systems are 0.22 Å and 0.30 Å, respectively, which are one order of magnitude larger

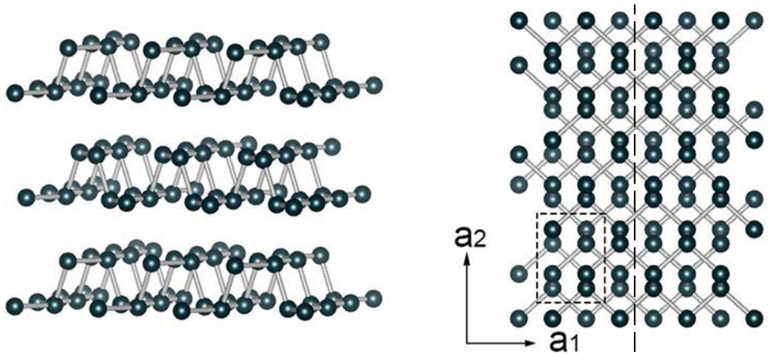

(a) Bulk BP, 3D rendering crystal stucture

(b) Bulk BP, top view

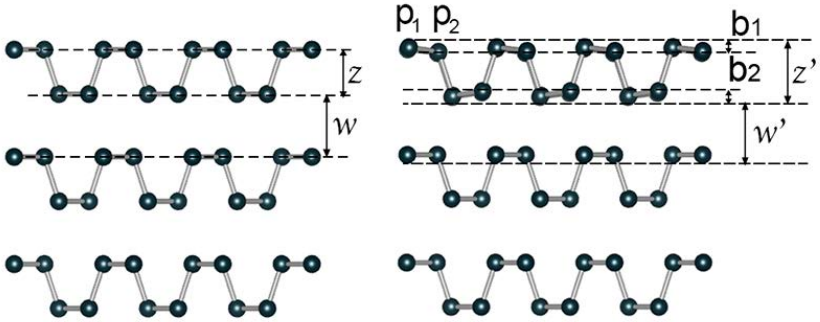

(c) Bulk BP, side view along the dashed line in (b)

(d) BP and FLP surface reconstruction, side view along the dashed line in (b)

Figure 5-1: (a)-(c) BP bulk crystal structure. (d) side view of BP and FLP relaxed surface structure, along dashed line in (b). Dotted square in (b) indicates the unit cell of BP, containing 8 P atoms.

than two previously reported theoretical values [93, 94]. Finally we use first-principles calculations to identify that the presence of surface vacancies is very likely the origin of not only the surface buckling in BP, but also the intrinsic hole-doping of phosphorene that was reported previously [37, 97].

5.2 LEEM/μLEED Experiments and Dynamical LEED-IV Analysis

Our experiments were carried out in the Elmitec AC-LEEM and LEEM V systems at the Center for Functional Nanomaterials in Brookhaven National Laboratory. The spatial resolution in LEEM mode is better than 3 nm and the electron beam spot size is 2 μm in diameter in the μLEED mode. Single-crystal bulk BP was cleaved in ultrahigh vacuum at room temperature. Fig. 5-2(a) shows the real-space bright field LEEM image of a freshly cleaved BP surface. μLEED data were acquired at the region denoted by the red 2 μm circle using a normal incident electron beam. Fig. 5-2(b) shows the well defined LEED pattern at 35 eV electron energy, indicating a very well-ordered surface. To prepare our FLP samples, black phosphorous flakes were mechanically exfoliated onto n-doped Si chips with native oxide, using a previously described method [66, 98]. The substrate was pre-patterned with gold marks, which allowed for locating and characterizing the flakes of interest using an optical microscope; see Fig. 5-2(c). This procedure was performed in a Ne atmosphere. Subsequently, the sample was encapsulated and transferred to the LEEM chamber. The total exposure time of the exfoliated sample to air was less than 5 minutes. Even with such a short exposure time, significant surface oxidization and contamination was observed using photo-emission electron microscopy (PEEM). In order to remove the surface oxide layers, we annealed the sample at 300°C in ultrahigh vacuum for 2 hours. As shown in PEEM and LEEM images, Fig. 5-2(d)-(e), the surface was pristine and uniform after successful

Table 5.1: Optimum parameter values for the surface structure of BP crystal and exfoliated BP flake

Model	T	b_1 (Å)	b_2 (Å)	z' (Å) ($\Delta z/z$)	w' (Å) ($\Delta w/w$)
Cleaved BP	300 K	0.225	0.269	2.287 (+5.3%)	2.825 (-8.0%)
FLP	573 K	0.300	0.290	2.381 (+9.9%)	2.877 (-6.3%)
DFT [93]	-	0.02	-	-	-
DFT [94]	-	0.06	-	-	-

annealing. Fig. 5-2(f) shows the sharp LEED pattern at 35 eV electron energy, indicating a very well-ordered layered structure. To fully investigate the surface atomic structure we collected μLEED-IV spectra for 7 recorded diffraction spots with an electron energy range of 25 to 135 eV for both sample varieties. The intensities of symmetrically equivalent beams were averaged to minimize intensity anisotropy of the diffraction beam due to possible small sample tilting ($< 0.1°$). Specifically, as shown in Fig. 5-2(b) and (f), intensities of spots A were averaged to assign the (01) diffraction beam and beam intensities of spots B were averaged to assign the (11) diffraction beam. The background intensity was then subtracted from the diffraction beam intensity.

Dynamical LEED-IV analysis, described in Chapter 3, was carried out to extract the surface atomic structural information for bulk BP and FLP from the corresponding μLEED-IV curves. The surface structural parameters are adjusted in search for the optimized surface structure that minimizes the R_2 factor. For electrons with an energy range of 25-135 eV, the mean free path is about 5 to 10 Å. Use of this energy range means that our μLEED-IV curves are most sensitive to the structural parameters of the top two phosphorene layers, i. e. the buckling of the top atomic layer b_1, the thickness of the first phosphorene layer z', the buckling of the bottom atomic layer b_2 and the Van der Waals gap between the top and second phosphorene layer w', as demonstrated in Fig. 5-1(d).

The utilization of the R_2 factor allows for the relative intensities of the diffraction beams

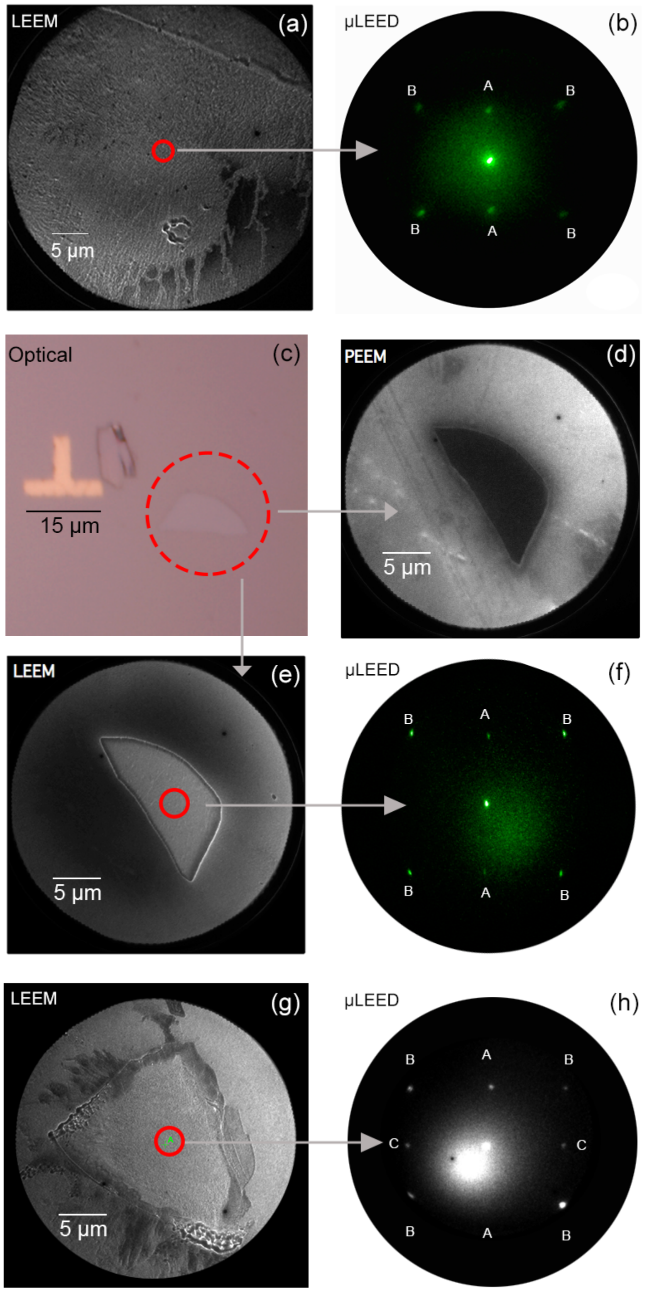

Figure 5-2: (a) LEEM image and (b) μLEED diffraction pattern of red-circled area in (a) taken at 30 eV electron energy of freshly cleaved bulk BP crystal surface. (c) Optical, (d) PEEM, (e) LEEM, and (f) μLEED image of red-circled area in (e) taken at 30 eV electron energy of mechanically exfoliated flake of FLP, of about 10 nm thickness. (g) LEEM image and (h) μLEED diffraction pattern of an exfoliated flake after annealing at 370°C, taken at 24 eV electron energy. Sharp diffraction pattern indicates that the surface is pristine and well ordered. An extra set of 'forbidden spots', the (10) beams denoted as C in (g), is clearly visible and unequivocal evidence of surface buckling on BP.

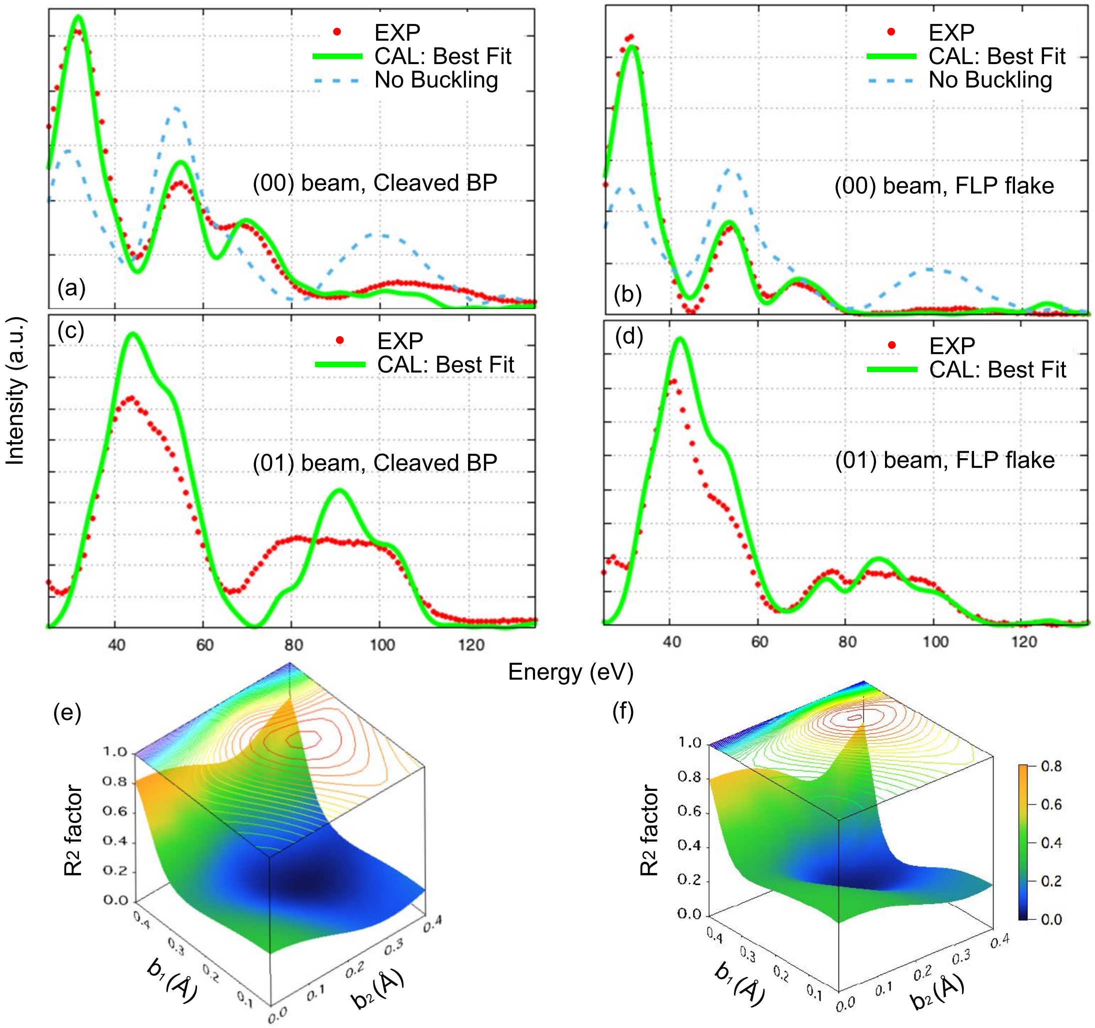

Figure 5-3: (a)-(d) (00) and (01) low-electron energy diffraction beam IV curves for cleaved BP crystal and exfoliated FLP flake, respectively. Green dotted curves are experimental and red line curves are calculated using optimized surface structural parameters. (e), (f) Reliability R_2-factor plotted vs. b_1 and b_2 for cleaved BP crystal and exfoliated FLP flake, respectively.

to be preserved during the optimization, which enhances the reliability of the surface structure determination. For the phase shifts calculation [60], the muffin-tin radii for phosphorus atoms was set to $r_P^{MT} = 2.099$ a.u. and 12 phase shifts ($L = 11$) were used for the LEED-IV calculation. The in-plane lattice constants were set to $a_1 = 3.313$ Å and $a_2 = 4.374$ Å, the thickness of the phosphorene layer to $z = 2.166$ Å, and the van der Waals distance between phosphorene layers to $w = 3.071$ Å for the bulk, as indicated in Fig. 5-1 [92].

The mean-square atomic vibrational displacements $<u^2>_T$ for the P atoms were calculated individually according to the relation between Debye temperature θ_D and $<u^2>_T$ at the sample temperature of T=300 K for bulk BP and T=573 K for the FLP flakes using Eq. 3.7 [56]. The Debye temperature θ_D was set to 550 K [99]. The inner potential, $V_0 + iV_{im}$, was set to be independent of energy. The real part V_0 was initially set to 8 eV and adjusted through ΔV_0 during the fitting process while the imaginary part V_{im} was fixed at 6 eV.

Best-fit structural parameter values are listed in Table 5.1 and compared with previously reported results [93, 94]. The calculated LEED-IV curves using optimized structural parameters match well with the experimental curves for both the BP crystal surface at 300 K and exfoliated FLP flake at 573 K, as shown in Fig. 5-3(a)-(d). The minimized R_2 factors are 0.03 and 0.02, respectively. For comparison, the calculated IV curves (blue dashed lines in Fig. 5-3(a)-(b)) using a flat, unbuckled surface, are distinctively different from our experimental results. For the freshly cleaved BP crystal surface, our results show that the top-layer surface buckling b_1 is 0.22 Å and the second phosphorus atomic layer buckling b_2 is 0.27 Å. The thickness of the top phosphorene layer z' is expanded by 5.3% from its bulk value of 2.166 Å. The van der Waals gap between the top and second phosphorene layer w' is contracted by 8% from its bulk value of 3.071 Å. For the mechanically exfoliated flake of FLP at 573 K, the top and second layer buckling are 0.30 Å and 0.29 Å, respectively. The surface bucklings are slightly larger at 573 K than the BP crystal surface at 300 K. We attribute this increase of surface buckling to thermal surface expansion at elevated temperature. For the same reason, the top phosphorene layer z' and the top van der Waals gap w' are also slightly increased at 573 K compared to 300 K. z' shows an expansion of 9.9% and w' a contraction of 6.3%, with respect to their corresponding bulk values. Due to the small data set and the very low R-factors (0.03 and 0.02) achieved, it is more difficult to assign meaningful uncertainties to the optimized individual structural parameters, using the previously employed method based on an increase of 4% of the R-factor. Figure 5-3(e)-(f) show plots of the reliability R_2 factor as a function of the surface buckling b_1 and the second atomic layer buckling b_2 for both of the investigated samples. Well defined minima were observed for both cases. The well defined minima and good agreement between experimental and calculated IV curves strongly support our surface structural results.

The most striking result is that the BP surface buckling b_1 is one order of magnitude larger than the previously proposed theoretical values [93, 94], for both BP and FLP samples investigated. Note that the buckling extends to second atomic layer. Similar significant surface buckling has also been predicted for other group V thin film materials such as Bi and other similar elemental 2D materials such as silicene, germanene, by various first-pricinples studies. Specifically, Cahangirov et al. predicted that the buckling height for silicene to be 0.44 Å and 0.64 Å [100]; Sadowski *et al.*, proposed the buckling of Bi thin film to be 0.5 Å [101, 102].

5.3 Evaporation of surface oxide layer on exfoliated BP flake observed by in-situ LEEM

In order to study the thermal stability of exfoliated BP flakes, I conducted another set of experiments for in-situ observation of the surface annealing at different temperatures using LEEM. BP flakes was mechanically exfoliated onto n-doped Si chips with native oxide situated under an optical microscope, using a previously described method [66, 98]. The flake thickness was estimated to be in the order of 100 nm based on optical contrast. Subsequently, the sample was transferred to the LEEM ultra-high vacuum (UHV) chamber. The total exposure time of the exfoliated sample to air was less than 10 min. LEEM was then used to locate the same flake, as shown in Fig. 5-4. μLEED pattern measured at 24 eV electron energy was then used to study the crystallinity of the as-exfoliated BP flake surface. No diffraction pattern was observed across the whole BP flake surface. It indicates that the freshly exfoliated flake surface is covered by an amorphous oxide layer, even after such a short exposure time. The BP flake was then annealed for 10 min at different temperatures from 150°C to 250°C. Representative temperatures are shown in Fig. 5-4(a)-(e), where no change on the surface was observed until 250°C when the edge of the top layer started to shrink. The flake was then further annealed at 250°C for about 1.5 hr until almost one third of the top layer evaporated, as shown in Fig. 5-4 (c). Again, no diffraction pattern was observed either in the exposed area, labeled in A or in the remaining oxide layer labeled in B. Only after an additional annealing around 370°C for 15 min., the top layer was completely gone, and a sharp diffraction pattern was observed, as shown in Fig. 5-4(i)-(j). A pristine BP surface was thus successfully prepared. Importantly, a set of for the unbuckled surface 'forbidden' diffraction spots, the (10) beams denoted by C in Fig. 5-4(j), are clearly visible. This is unequivocal evidence of the surface glide symmetry breaking due to the height difference of P_1 and P_2, i. e. the surface buckling.

5.4 Origin of the presence of 'forbidden' (10) diffraction spots

Black phosphorus belongs to the symmetry group *Cmca*. Intensities of two (10) beams are cancelled out due to the surface glide plane symmetry. The buckling, i. e. the different height between P_1 and P_2, breaks the glide plane symmetry and makes the 'forbidden'

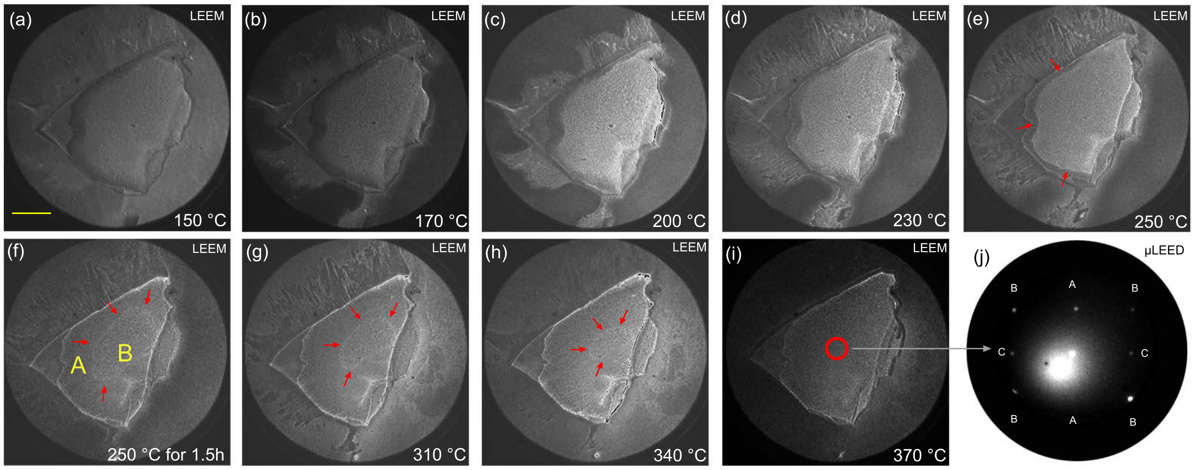

Figure 5-4: (a)-(e) LEEM images of a freshly exfoliated BP flake, after annealing in a LEEM UHV chamber at various temperatures. The sample was annealed at each temperature for 10 min from 150°C to 370°C, except for 250°C, where the sample was held for 1.5 hr. μLEED was used to monitor the surface crystallinity following each annealing step. (e) Starting from around 250°C, the top oxide layer began to evaporate and shrink from the edge. (i) Further annealing at around 370°C leads to a complete evaporation of the top oxide layer and produces a pristine BP surface as confirmed by a sharp μLEED pattern shown in (j), taken at 24 eV. The presence of an extra set of, for the flat surface forbidden, diffraction spots, the (10) beams and denoted as C in (j), is direct evidence of surface buckling. The scale bar in the LEEM images is 5 μm.

diffraction spots appear. The slight assymetry in the LEED spot intensities in Fig. 5-4(j) is an indication of a slight tilt of the incoming electron beam with respect to the surface normal of the order of one degree. To exclude this slight sample tilt as a possible origin of the observed extra diffraction spots, we performed off-normal LEED-IV calculations. As Fig. 5-5(a) shows, when no buckling is considered in the calculation, a small tilt angle (3°) would not significantly influence the relative intensity of either (01) or (10) beams. The intensity of the (10) diffraction spot remains undetectably small even when a small tilt angle of 3° is applied to the sample. In stark contrast, Fig. 5-5(b) shows that when the a buckled BP surface is considered, the small off-normal angle (3°) enhances the intensity of the (10) beam dramatically and makes it comparable to the intensity of the (01) beam in a small energy window around 24 eV. These calculation results agree well with our experimental observation and further confirms that the extra 'forbidden spots' are due to surface buckling.

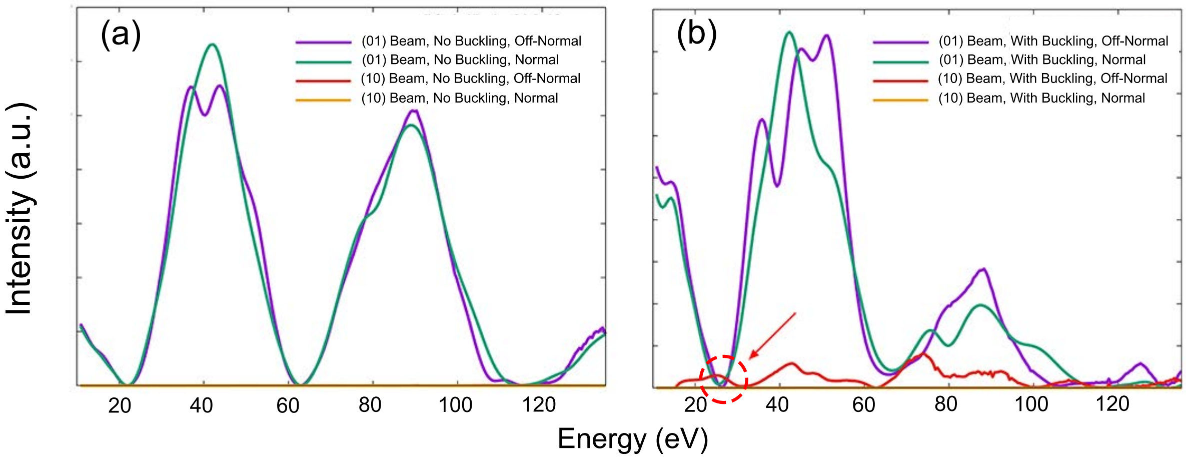

Figure 5-5: Influence of buckling and incident electron beam off-normal angle on the intensities of diffracted spots (01) and (10) beams. (a) When buckling is not included in the calculation, the (10) beam intensity remains zero across the whole energy range for both normal and 3° off-normal incidence. (b) When buckling is included in the calculation, the (10) beam intensity becomes comparable to the (01) intensity within a small energy window around 24 eV when the incident electron beam is 3° off-normal. Thus the (10) beam will be visible within the small energy window in the diffraction pattern which matches with experimental observation.

5.5 DFT Calculations

In order to support the measured significant buckling and reveal its origin, first-principles calculations were conducted by collaborators. Calculations were carried out based on the framework of density functional theory (DFT) with projector augmented (PAW) potential [103] as implemented in the Vienna ab initio simulation package (VASP) [104, 105, 106]. The plane-wave functions expanded with an energy cutoff of 400 eV were employed throughout calculations. The exchange-correlation energy was described by generalized gradient approximation (GGA) in Perdew, Burke, and Ernzerhof (PBE) form [107]. The k points in two-dimensional Brillouin zone (BZ) of the 1×1 unit cell of monolayer BP containing 4 phosphorous atoms were sampled on a 16×12 mesh. The van der Waals (vdW) interactions were also incorporated within the Tkatchenko-Scheffler method [108]. In addition, we employed the Heyd, Scuseria, and Ernzerhof (HSE06) hybrid functional [109, 110] for the band structure calculations.

The structure of monolayer phosphorene and the top phosphorene layer of bulk BP (a six-layer supercell) were calculated and compared. Only very small structural differences were observed, < 0.001 Å, between the atomic positions and bond lengths of the monolayer phosphene and that of the top layer of bulk. This is expected for layered materials with weak van der Waals bonding in between adjacent layers. In order to simplify our calculations, we focus on single-layer phosphorene. However, final model structures were compared against consistency calculations for two bi-layer phosphorene and no signs of interactions other than van der Waals were found. The thickness of the vacuum layer in each slab structure is more than 15 Å.

First, defect-free monolayer phosphorene with different supercell sizes were investigated. The lattice structure was optimized until the atomic force, both Hellmann-Feynman and vdW terms included, on each relaxed atom was less than 1 meV/Å. In an up to 8×4 supercell, no buckling was found within the accuracy of the calculation. This result is reasonable since both BP bulk and monolayer structures have the insulating electronic structures with bandgaps, and exposed surfaces do not bring about the electronic mismatch or additional dangling bonds. Surface reconstruction is thus not necessary in such a stable structure.

However, if an impurity, such as vacancy defect [94, 111] or doping [37, 97] is induced on the surface, the situation changes completely. In fact, Riffle *et al.* [111] and Liang *et al.* [94] have recently observed vacancy defects on their freshly cleaved surfaces of BP crystals using STM. Here, we introduced a single point defect into the monolayer phosphorene by removing one atom. Several supercells were calculated with their sizes ranging from 2×4 to 8×4. After the structure optimization, deviations of the atoms along out-of-plane direction were observed in all of these structures. As shown in the top view (middle panel) of Fig. 5-6, each supercell has 8 zig-zag rows, and the defect is located on the upper layer of row 3.

The magnitude of buckling in each row is summarized in the bottom panel of Fig. 5-6. by calculating the standard deviations of the phosphorus atoms' z components for each entire row. It is seen that the buckling is maximized in rows around the defect, and the maximum buckling ranges from 0.15 Å to 0.33 Å through all the supercell sizes under investigation. These calculations agree well with our experimental values of 0.22 Å to 0.30 Å. Although the buckling magnitude decays rapidly along the armchair direction, away from the row, on which the defect is located, no significant decay in the buckling magnitude was found in the zig-zag direction. Based on these results, it is concluded that the buckling is significantly enhanced near the point defect. It is anisotropic and long-range along the zig-zag direction while it is short-range along the armchair direction. The defect-induced buckling cannot be maintained in the armchair direction. This interesting insight agrees well with the previous experimental observation of an anisotropy in the surface density of state (DOS) on the BP surface by STM [94].

Intuitively, one would expect that such long-range buckling would be reflected in the band structures as well. Thus the electronic structure of the 4×4 supercell with a single vacancy was investigated and compared with that of a clean monolayer. According to the density of state results shown in Fig. 5-7 (a)-(b), the clean monolayer BP is insulating with a bandgap of 1.5 eV, while an impurity state is present in the defect containing supercell across the Fermi level close to the top of valence states. A similar state was also observed by Zhang et al. [93] in their STM dI/dV measurement. This indicates the existence of the defect-induced hole-doping electronic structure in these defect structure, i.e. each phosphorus vacancy generates three dangling bonds that need to be saturated by more electrons. This suggests that the distortion of the lattice, such as buckling, appears in order to eliminate this instability of the electronic structure.

To better understand the relation between hole-doping and the surface structure of BP,

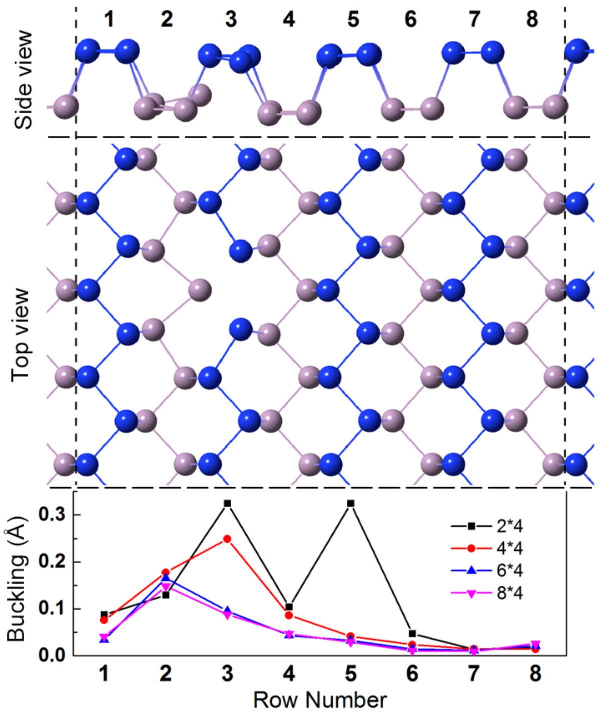

Figure 5-6: Phosphorene atomic structure with defect introduced. Upper panels: Side and top view of a n×4 (n=2, 4, 6, 8) supercell of the monolayer phosphorene with a point defect introduced at row 3. Blue and grey color of balls distinguish the top and second P atomic layers. Lower panel: Average magnitude of buckling in each row for various n×4 supercells.

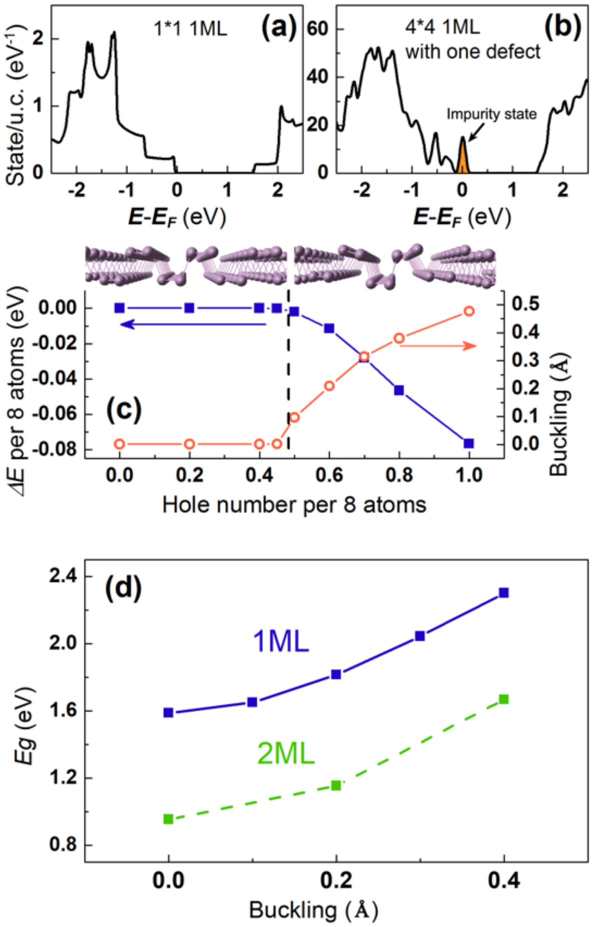

Figure 5-7: Buckling and hole-doping induced by defects. The DOS for (a) the ideal monolayer and (b) the 4×4 defect-included supercell BP. The Fermi level is set to zero. (c) Energy difference (blue solid squares) between the buckled and non-buckled configurations and the magnitude of buckling (red open circles) as the increasing hole-doping number. (d) Dependence of bandgap on the buckling magnitude in monolayer (blue solid line) and bi-layer (green dashed line) phosphorenes. The magnitude of the buckling is adjusted in single-layer phosphorene (1 ML) and the top bi-layer of two-layer phosphorene (2 ML) from the range of 0 Å to 0.4 Å. The bandgap of each structure is calculated accordingly and shown in (d).

the hole doped 2×1 clean supercell structures with a tunable total electron number was optimized. As shown in Fig. 5-7(c), buckling appears when the hole number exceeds 0.5 per 8 phosphorous atoms. The magnitude of the buckling as well as the energy difference between the buckled and ideal structures increases rapidly with the rise of the hole number. In particular, the buckling reaches 0.2 Å when the hole number is 0.6 per 8 atoms. Our first principle calculations thus show that the presence of defects induces hole doping on the clean BP surface, which in turn leads to lattice distortion and the surface buckling. It was confirmed experimentally that both undoped bulk BP [97] and FLP [37] are p-type semiconductors, but the origin of intrinsic p-type doping is unclear so far. Recently, Osada proposed that the edge state of finite bi-layer phosphorene might be the origin of the intrinsic hole-doping around the edge [112]. Our DFT calculations, together with the experimental observation of BP surface reconstruction, strongly indicate that the presence of surface defects is a likely explanation for the intrinsic hole-doping for both bulk BP and FLP.

DFT was also utilized to study the influence of surface buckling of BP on its band structure. Fig. 5-8 shows the calculated band structure of ideal monolayer phosphorene without layer buckling (black dotted curves) compared with the calculated band structure of monolayer phosphorene with 0.2 Å layer buckling (red solid curves). The buckling further opens up the bandgap of phosphorene at the Γ point. The dependence of band gap of monolayer and bi-layer phosphorene on the layer buckling magnitude was calculated and summarized in Fig. 5-7 (d).

5.6 Conclusions

To summarize, we observed that significant oxidization of exfoliated BP flakes occurs even after short exposure to air, but the oxide layer can be efficiently removed by annealing at

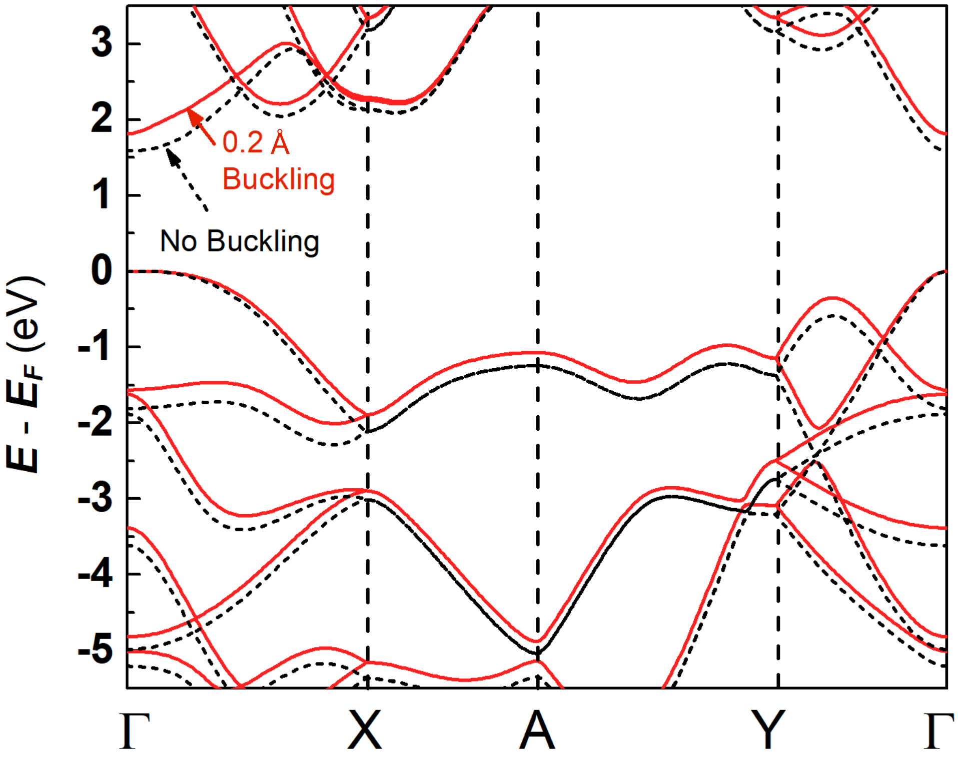

Figure 5-8: Calculated band structure of ideal monolayer phosphorenen without layer buckling (black dotted curves) compared with the calculated band structure of monolayer phosphorene with 0.2 Å layer buckling (red solid curves).

250°C to 370°C. Using high spatial resolution LEEM and unique μLEED-IV analysis, the significant surface buckling on the top pristine BP surface and the associated symmetry breaking are directly observed in the form of additional diffraction spots in the LEED pattern and the surface buckling is quantitatively measured. It is 0.22 Å for the cleaved bulk flake and 0.30 Å in the 10 nm thick FLP flake. A similar buckling for the second phosphorus layer was identified, which is accessible by high subsurface sensitive μLEED-IV. Using first-principles calculations, we further confirmed our surface structural results and proposed a vacancy defect driven mechanism for the surface buckling. The surface vacancy defect also introduces an impurity state in the band gap, and is consistent with previous reports of intrinsic p-type nature of phosphorene materials. During the preparation of this manuscript, vacancy defects in similarly cleaved BP surface were reported in STM/STS measurements [113, 111].

The surface buckling addressed in this work can be potentially used to modify the bandgap of thin BP flakes and may lead to future electronic applications. As shown in Fig. 5-7(d), based on the first-principles calculation, buckling indeed increases the bandgap at the Γ point for both monolayer and bi-layer phosphorenes. The bandgaps increase from 1.59 eV to 2.30 eV for monolayer and from 0.95 eV to 1.67 eV for two bi-layer phosphorene when a buckling of 0.4 Å is introduced in the top layer. Even with a limited data set of buckling magnitudes at different temperatures, our measurement indicates a possible temperature dependence of the surface buckling. While previous studies have shown anomalous temperature dependence of the bandgap in both phosphorene [114] and bulk black phosphorus [115, 116], which may lead to BP based thermoelectric devices, and more detailed studies are needed.

CHAPTER 6

TOPOLOGICAL CRYSTALLINE INSULATOR TIN SELENIDE AND 1T TIN DISELENIDE

6.1 Introduction

Recently the Sn-Se system has attracted immense attention due to the versatility of crystalline phases, each with properties important for device applications. $SnSe_2$ is of interest because of its high work function, making it an ideal material for tunneling based devices consisting of layered materials such as Esaki diodes [117], tunneling field effect transistors (TFETs) [118] and two-dimensional heterojunction interlayer tunneling field effect transistors (Thin-TFETs) [119]. Theoretical study on strain induced electronic and magnetic properties of SnSe2 nanostructures shows even more promise this system holds [120]. On the other hand, the monochalcogenide, SnSe, has a few allotropes. First, a GeS like staircase structure (Pnma space group, No. 62) that undergoes a transition into (Cmcm space group, No. 63) at 477°C and has a high thermoelectric figure of merit around and above this transition temperature [121]. Second, metastable rock-salt structure phase was predicted to be a topological crystalline insulator [43, 122]. Other experimental pursuits in this system have been towards realization of high-performance photodetectors [123], van der Waals superlattices [124, 125, 126] phase change memory [127], alloying with sulfur (S) for bandgap tuning [128] and with manganese (Mn) for room temperature weak ferromagnetism [129].

For the Sn-Se system molecular beam epitaxy (MBE) has evolved as a powerful technique [130, 131] for growth as it enables growth with monolayer precision [132], in-situ X-ray photoelectron spectroscopy measurements for determining band alignments [133, 134], controlled alloying [135], stabilizing metastable phases [43, 122] and low temperature growth of heterostructures [124, 125, 126]. By controlling the growth condition, different crystalline phases can be achieved for the Sn-Se system. Primarily, the following growth conditions have been varied by collaborators to understand their effects on the crystalline phases formed: the substrate temperature, Se:Sn ratio and the growth rate. Multiple characterization technique have been utilized by collaborators and I to probe the as grown films, including Reflection high-energy electron diffraction (RHEED), X-ray diffraction (XRD), Raman spectroscopy, Atomic force microscopy (AFM), Transmission electron microscopy (TEM), X-ray photoelectron spectroscopy (XPS), Low energy electron microscopy (LEEM) and Low energy electron diffraction (LEED).

A summary of the growth condition and corresponding results can be found in [136]. In this chapter, I will describe my work of using LEEM/LEED-IV to study the surface structure of the rock-salt SnSe and 1T-$SnSe_2$.

6.2 Topological Crystalline Insulator Tin Selenide

Topological insulators behave as electrical conductors on their surface but as insulators in their interior, which gives rise to intriguing phenomena that could be used in quantum computing and optoelectronics. Searches for new materials that could exhibit this behavior have led to a substance known as a topological crystalline insulator (TCI), whose properties arise from crystal symmetries. Unlike standard topological insulators, any modification to the surface properties of a TCI can critically compromise its unique behavior. In addition, in a typical TCI compound that comprises stacks of polar atomic planes, the divergence of electrostatic energy may destabilize the system and reconfigure the surface structure significantly. Our work makes use of the semiconductor tin selenide (SnSe), a structurally simple material that hosts rich material phases.

For topological materials, in general, the surface configuration is crucial for their Dirac surface states [137, 138]. In particular, the tin monochalcogenide TCI is an important platform for investigating the correlation between Dirac surface states and its surface configuration. Since the surface states of TCIs are crystal-symmetry protected, they depend sensitively on the surface orientation. In particular, the (001) surface states possess hybridized double Dirac-cones in close vicinity to the $\bar{X}$ point of the (001) SBZ, while the (111) surface states possess four Dirac cones centered at the $\bar{\Gamma}$ and $\bar{M}$ points of the (111) SBZ [139]. In previous experiments, the (001) surface states have been more intensively investigated because the (001) surface is a natural cleavage plane of rock-salt IV-VI semiconductors. In contrast, the (111) surface is a polar surface, which is typically difficult to prepare because of its unstable structure arising from the divergence of the electrostatic energy along the polar direction, i.e., the well-known polar catastrophe [140, 141]. This phenomenon may be ameliorated by structural reconfiguration of the surface, which strongly depends on the type of surface termination. Until now, a limited surface termination has been employed in the (111) surface of rock-salt TCI. For example, recent studies of $\mathrm{Pb}_{1-x}\mathrm{Sn}_x\mathrm{Te}$ have indicated Te termination of its (111) surface [142]. Very recently, the TCI phase in a metastable SnSe (111) thin film with rock-salt structure has been observed and was found to be Se terminated and hydrogen passivated using first-principles calculations [122]. Thus, previous experiments have shown the stability of anion-terminated

TCIs, either with Te or Se. The cation-terminated surface, i.e., the truncated-bulk Sn-terminated surface, however, was predicted to be unstable, and, as a result, it undergoes surface reconstruction to diminish its surface energy [143]. Despite its great importance to the full understanding of this family of TCIs and its role in the development of potential high-quality TCI devices, a comprehensive investigation of the correlation between surface configuration and topological surface states has thus far been lacking.

6.2.1 Sample Preparation

The Sn-Se system is structurally simple, but it contains very rich phases. The energetically stable phase of SnSe has an orthorhombic GeS structure, which is a topologically trivial phase. Molecular beam epitaxy (MBE) is used to grow a SnSe thin film in a rock-salt structure [see Fig. 6-1(a)], by our collaborators, Prof. Xing's group from Cornell University. This film has a thickness of 26 monolayers and is grown on a crystalline Bi_2Se_3 thin film on a GaAs (111) substrate. The lattice constant of Bi_2Se_3 is closely matched to the in-plane lattice constant of rock-salt SnSe and, as a result, the epitaxial SnSe (111) [see Fig. 6-1(b)] is constrained to a rock-salt structure. The growth conditions are detailed in Ref. [43]. The growth was carefully monitored and characterized in situ using reflection high-energy electron diffraction (RHEED) (see Ref. [43], Sec. I). The SnSe thin film is protected from ambient atmospheric exposure following growth with a Se cap in the growth chamber. Prior to our microscopy or spectroscopy measurements on each sample, the Se cap was removed by heating at 200°C for 30 min in ultrahigh vacuum.

6.2.2 XRD, ARPES and Electronic Structure

The bulk crystalline structure of the epitaxially grown thin film was first investigated using XRD. The XRD results confirmed the epitaxially grown thin film to be rock-salt SnSe. More details of the XRD results can be found in [43].

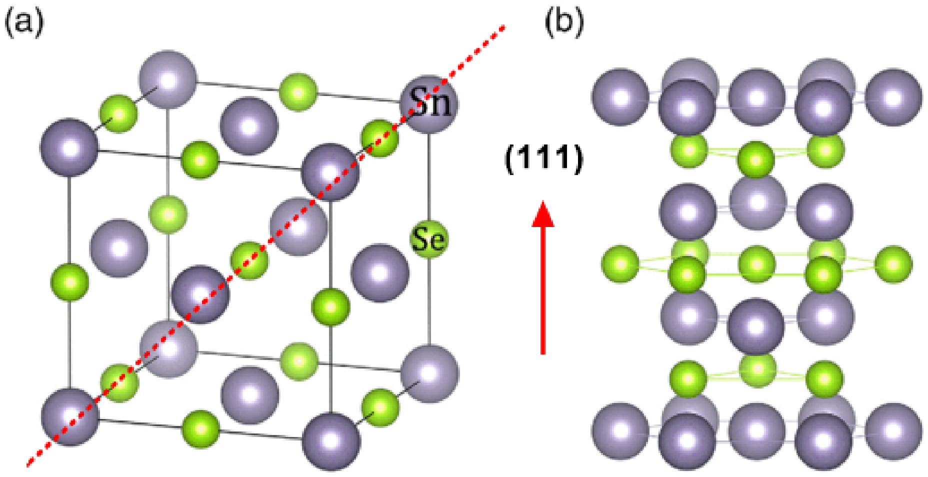

Figure 6-1: (a) Schematic of the lattice structure of rock-salt SnSe. (b) Layered rock-salt SnSe depicted along the (111) direction, shown as the dashed line in (a).

The electronic structure of the SnSe (111) sample was directly measured by collaborators using a synchrotron-based high-resolution ARPES system. Figure 6-2(a) shows the ARPES band map along the $\bar{M}$-$\bar{\Gamma}$-$\bar{M}$ high-symmetry direction acquired using a 25 eV incident photon energy. Figure 6-2(b) shows the momentum distribution curves (MDCs) plot of the band map of Fig. 6-2(a). In sharp contrast to the electronic structure of Se-terminated SnSe with hydrogen passivation, where a Dirac point at the $\bar{\Gamma}$ point is located at approximately 0.1 eV below Fermi level (E_F) [122], we observed Dirac-like linear dispersive bands crossing at about 0.4 eV below E_F. As shown in Fig. 6-2(c), linear fitting to the MDC peaks yields a Fermi wave vector of k_F=0.14±0.01 Å^{-1} and a high Fermi velocity of $v_F = (0.50 \pm 0.01) \times 10^6$ m/s. The Fermi velocity for the Sn-terminated SnSe sample is 3 times larger than for its Se-terminated counterpart [122].

To aid in interpreting the electronic structure and the topological character of rock-salt SnSe, first-principles calculations were carried out by collaborators (see [43] for calculation details). In contrast to the method reported in Ref. [122], in which dangling bonds were eliminated using hydrogen passivation of the Se termination, a truncated-bulk surface was used in our calculations. In fact, in our calculation, the Sn-terminated surface Fig. 6-2(d)

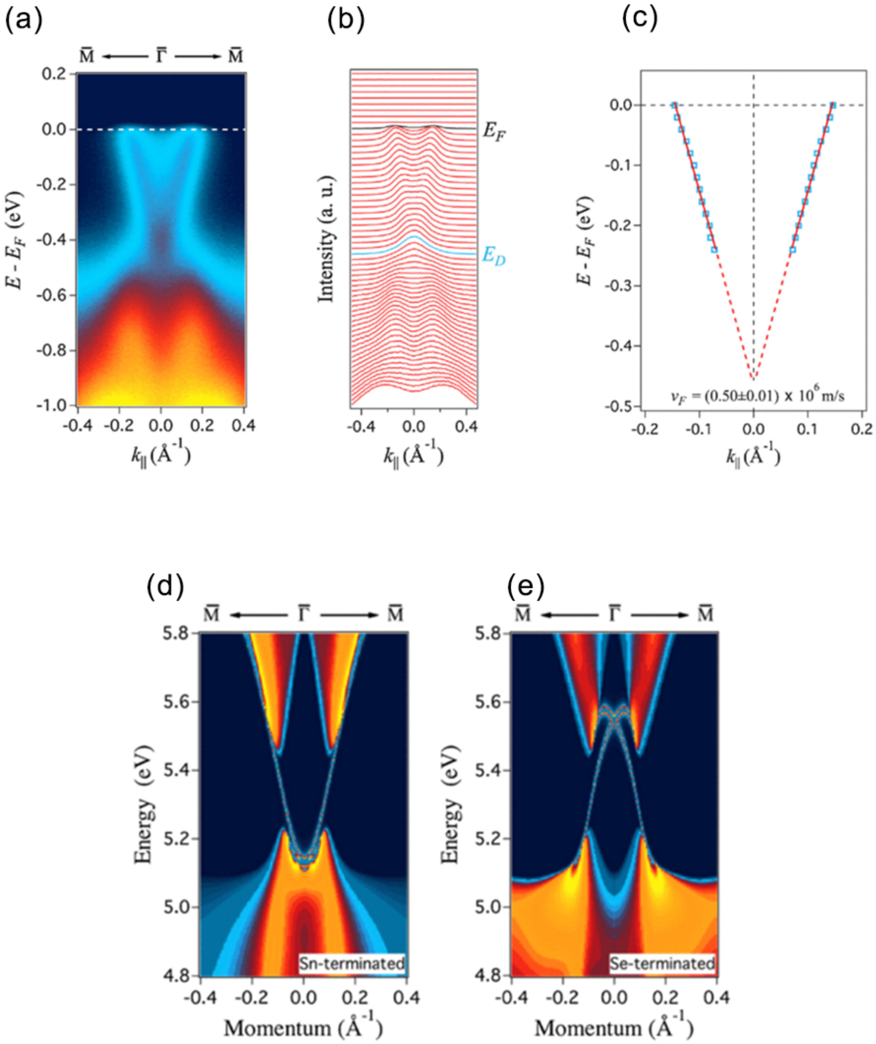

Figure 6-2: (a) ARPES band map ($h\gamma$=25 eV) along the $\bar{M}$-$\bar{\Gamma}$-$\bar{M}$ high-symmetry direction. (b) MDC plot of the band dispersion shown in panel (a). Energy positions of the Fermi level and Dirac point are denoted as $E_F$and E_D, respectively. (c) MDC peak positions (blue dots) and linear fitting (red dashed line). (d) and (e): First-principles calculations of the band structure for (d) Sn-terminated and (e) Se-terminated SnSe (111) thin films.

and the Se-terminated surface [see Fig. 6-2(e)] are found to yield strikingly different surface states. In the Sn-terminated case, the Dirac point is close to the bulk valence band, while in the Se-terminated case, the Dirac point is close to the bulk conduction band. This result implies that our SnSe(111) thin film has a Sn-terminated surface. In fact, a linear fitting to the calculated surface state of the Sn-terminated SnSe yields a Fermi velocity of 0.55×10^6 m/s, which is in good agreement with our measured value.

6.2.3 Dynamical LEED-IV Analysis

In order to investigate the surface structure of the grown rock-salt SnSe, measurements were carried out on our SnSe thin film using μLEED and dynamical LEED-IV analysis. The resulting SnSe μLEED pattern shows one set of sharp hexagonal diffraction spots along with a faint ringlike background, as shown in Fig. 6-3 (c). This result is consistent with our thin films having one dominant in-plane crystal orientation along with a small percentage of randomly misaligned small domains. This observation allows us to rule out the (2×1) or $(\sqrt{3}\times\sqrt{3})\mathrm{R}30^\circ$ reconstruction [143].

LEED-IV measurements were carried out to extract the energy dependence of the electron reflectivity of the (00) diffraction beam. I determined the surface structure using dynamical LEED-IV analysis. As shown in Fig. 6-4, the calculated IV curve of an optimized Sn-terminated surface accurately reproduces the major features of our measured IV curve, while the calculated IV curve of a Se-terminated surface is strikingly different from the experimental data. This result further supports the fact that a SnSe thin film with a Sn-terminated surface can best interpret our data.

An additional important question is the stability of the polar surface of SnSe. As shown in Fig. 6-1 (b), a SnSe (111) thin film has a stacking sequence of Sn^{2+} and Se^{2-} atomic planes, which gives rise to a surface dipole moment and surface charge [140]. Such a stacking

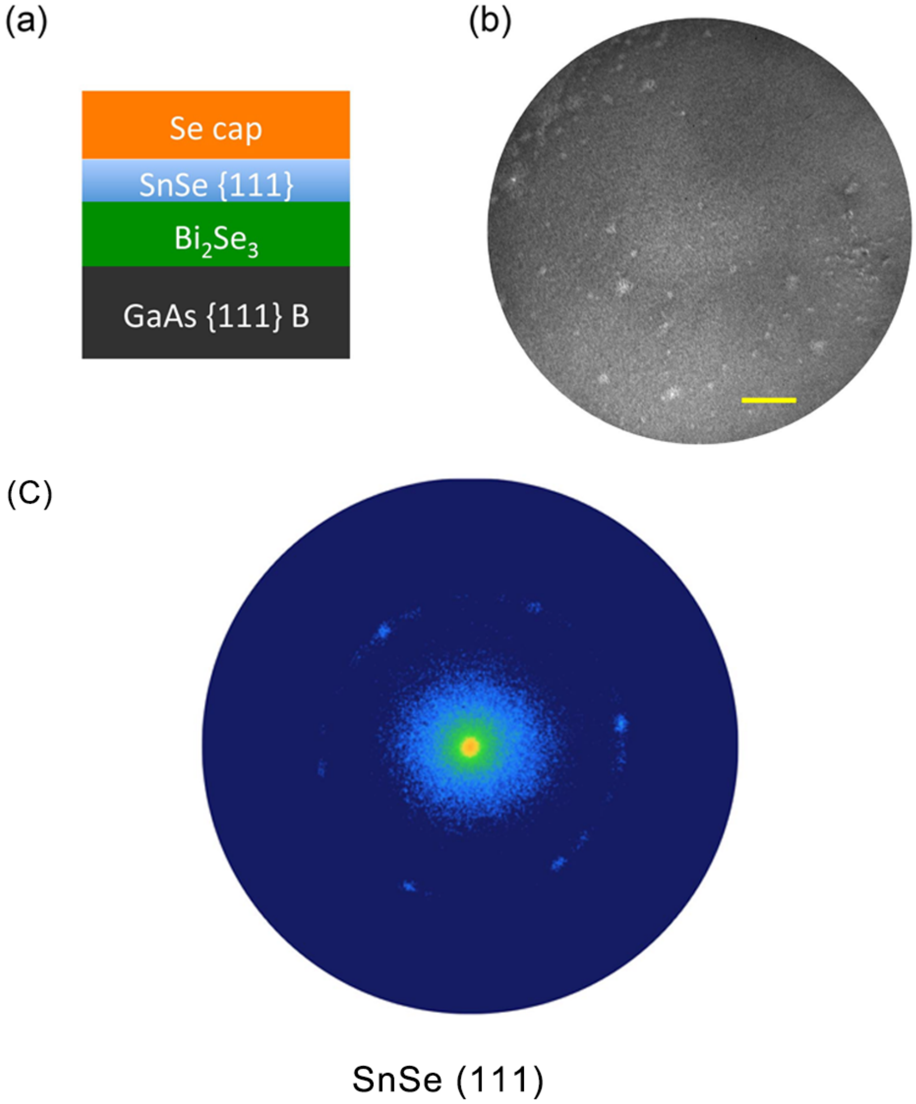

Figure 6-3: (a) Schematic of the MBE grown sample configuration. (b) LEEM image of the SnSe(111) surface, with Se cap removed, the scale bar is 5 μm. (c) μLEED pattern of the SnSe(111) surface.

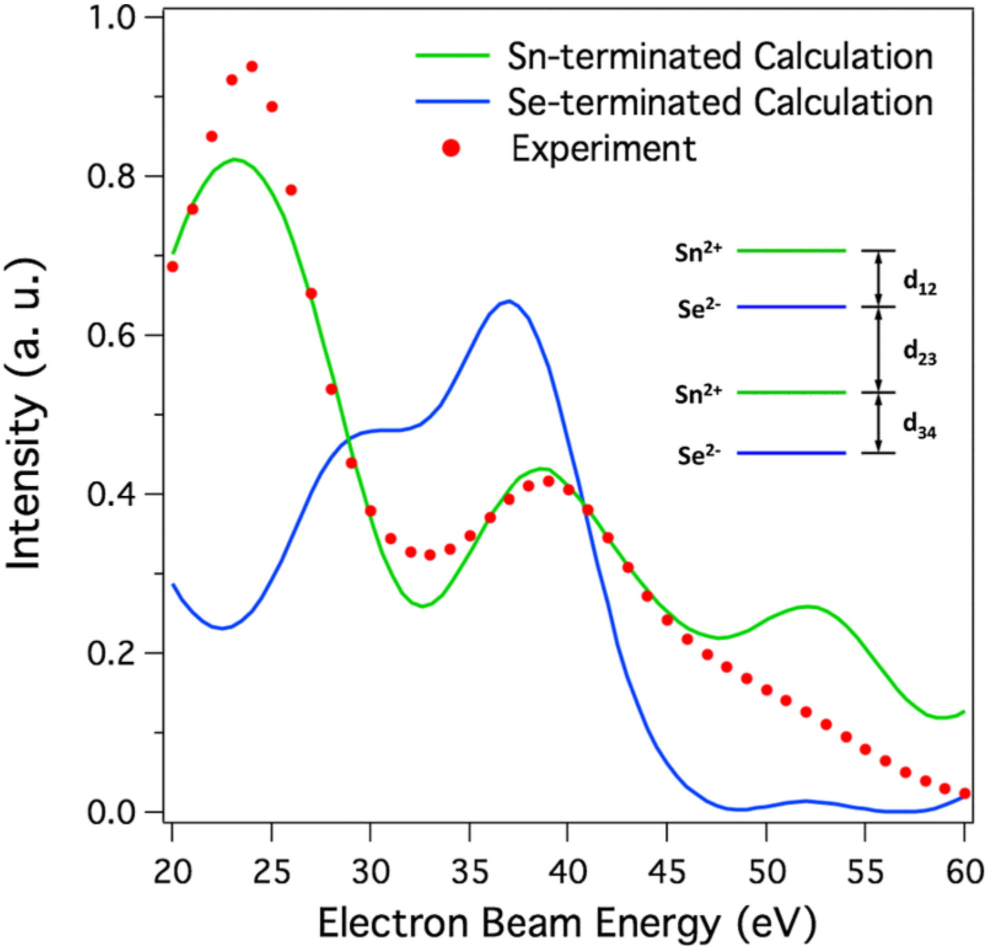

Figure 6-4: Calculated LEED-*IV* curves for the (00) diffraction beam for an optimized Sn-terminated surface (green solid curve) and a Se-terminated surface (blue solid curve) and the measured electron reflectivity curve (red dots).

Table 6.1: Calculated optimum top few layer spacings d_{ij} between the ith and jth atomic planes (the inset of Fig. 6-4) for a SnSe thin film with a Sn-terminated surface and the relative deviation with respect to the bulk layer spacing d_0

Parameters	Optimized values (Å)	$\Delta d_{ij}/d_0$
d_{12}	1.64	−6.2%
d_{23}	1.89	+8.1%
d_{34}	1.68	−4.1%

sequence can be compensated through the formation of a suitable surface reconstruction [143]; however, such a compensation mechanism has been ruled out in our case through our LEED measurement. Another possible charge-compensation mechanism is a spatial variation of the slabs along the dipole direction [141]. In my structural-optimization procedure, the top four layers of the SnSe (111) thin film with Sn termination are permitted to adjust their interlayer spacing around their initial value of 1.75 Å, thus enabling charge compensation (see [43], Supplementary Material, Sec. X, for a schematic of the charge-compensation mechanism). As a result of this calculation, best-fit parameters are obtained and summarized in Table 6.1, revealing an oscillatory, contraction-expansion-contraction pattern for the structural relaxation in the top few layers of SnSe. This is the first direct evidence of the oscillatory structural relaxation predicted by DFT calculation [143]. Note that a good agreement between calculated and experimental IV curves is achieved in the energy range of 20-60 eV (electron penetration depth in this range is estimated to be less than 8 Å), suggesting that the structural relaxation is occurring in the top few layers. However, because of the limited accessible energy range (20-100 eV), a meaningful final R factor was not quantified here.

6.2.4 Conclusions

In conclusion, I have conducted dynamical LEED-IV analysis to study the surface structure of an epitaxial rock-salt SnSe (111). This investigation demonstrates that our SnSe (111) thin film has a pristine Sn-terminated surface, which is stabilized via an oscillatory variation of the spacings between the top few layers. In the ARPES experiments, robust surface states with ultrahigh Fermi velocity are observed at the SBZ center. Such distinct properties may lead to potential applications in electronic and spintronic devices, and open a possible route to the manipulation of surface states via tuning of the surface termination in metastable epitaxial topological materials.

6.3 Tin Diselenide ($SnSe_2$)

The difference in enthalpy of formation of bulk $SnSe_2$ is just 0.1 eV lower than that of SnSe, thus phase transition could potentially be induced by high energy or intrusive probing of a characterization technique, such as focused ion beam (FIB) thinning or e-beam in a TEM. Similar material, SnS_2 has been reported to have an e-beam induced phase transformation to SnS [144]. An inverse phase transformation from SnSe to $SnSe_2$ has also been observed in our previous study [43]. For this kind of sensitive material, the non-intrusive low energy probing LEEM and μLEED are the perfect candidates for its surface crystal structure study.

$SnSe_2$ is also easily oxidized in air. A Se cap layer is used to protect the sample from oxidization, after the deposition of 1.7ML of $SnSe_2$ on top of the GaAs substrate. The Se cap was then removed in the LEEM UHV chamber ($<10^{-9}$ Torr) through annealing at around 200°C for 30 mins. Selected area low energy electron diffraction intensity versus electron energy (μLEED-IV) data were collected for normal incident electron with energy ranging from 28 to 133 eV. I carried out dynamical LEED-IV analysis in order to extract the atomic crystal structure information of the 1T-$SnSe_2$ thin film.

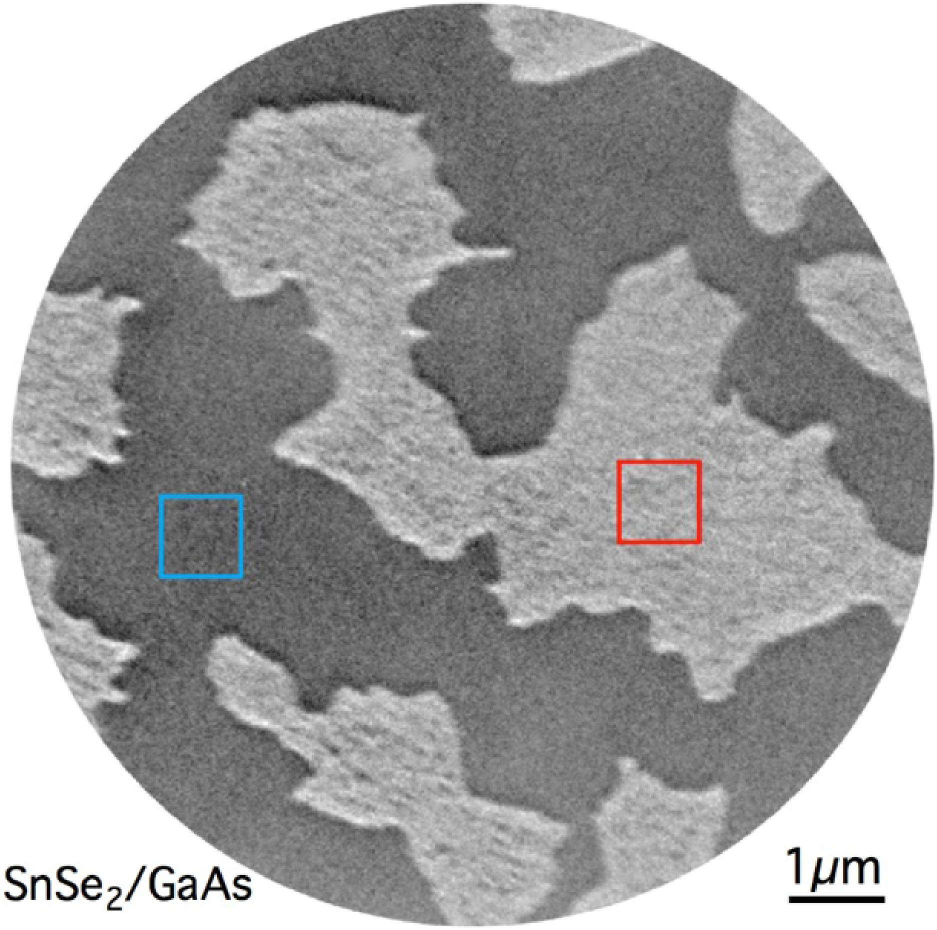

Figure 6-5: LEEM image after Se de-capping. The area labeled with red square is $SnSe_2$ and the area labled with blue square is the GaAs substrate.

6.3.1 LEEM Image and LEED Pattern

Figure 6-5 shows the LEEM image of the sample after annealing and removing the Se cap layer. The LEEM image shows a uniform $SnSe_2$ surface formed in an island style on a uniform GaAs substrate. It indicates that the MBE grown SnSe2 thin film is uniform and grows in a Volmer-Weber or island growth mode. The sharp LEED pattern, Fig. 6-6, acquired on the $SnSe_2$ area further confirms the well-ordered crystal structure of the grown 1T phase of the $SnSe_2$ thin film.

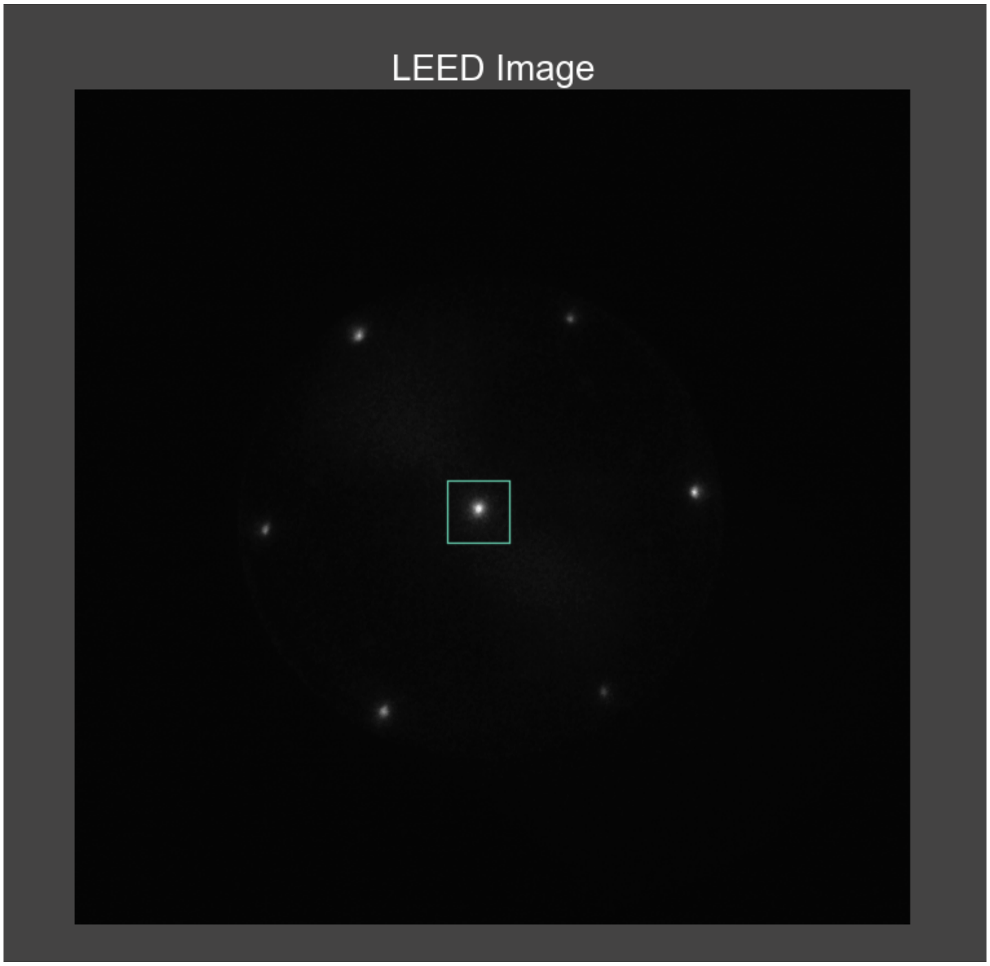

Figure 6-6: LEED pattern acquired on the $SnSe_2$ area.

6.3.2 Dynamical μLEED-IV Analysis

Calculation package LEEDopt, described in Chapter 3, was used for dynamical μLEED-IV analysis. The in-plane lattice constant was set to a=3.811 Å and c=6.017 Å [145]; Debye temperature was set to 280 K [146] and the muffin-tin radius was set to R_{Sn}=2.984 a.u., R_{Se}=2.120 a.u., for Sn and Se, respectively. 12 phase shifts (L = 11) were used for the LEED-IV calculation. As shown in 6-8, the interlayer spacing between the top Se atomic layer and the Sn atomic layer d_{12}, the spacing between the first Sn atomic layer and the second Se atomic layer d_{23} and the spacing between the first and the second Se-Sn-Se sandwich layer d_{34} were varied as free input parameters for the calculation codes to achieve the best agreement between the calculated and the experimental LEED-IV curves. As shown in Fig. 6-7, the calculated IV curve for the (00) beam accurately reproduces the major features of our measured IV curve. The calculated IV curve is shifted upwards for better visual comparison. The optimized surface atomic structural parameters are summarized in Tab. 6.2. The surface atomic crystal structure of the MBE grown thin film of 1T-$SnSe_2$ was found to remain mostly the same as its bulk while undergo a slight surface interlayer relaxation. This is expected for layered materials with weak van der Waals interaction between the surface layer and its bulk. Specifically, the interlayer spacing between the top Se atomic layer and the Sn atomic layer, d_{12}, was found to have a slight contraction of about 3%, comparing to the bulk value. Similar surface relaxation was found in other layered 2D materials such as MoS_2 [41]. The interlayer spacing between the Sn atomic layer and the second Se atomic layer, d_{23}, was found to expand slightly by about 4% from its bulk value. The thickness of the first Se-Sn-Se sandwich layer $d_{13}=d_{12}+d_{23}$, is only dilated by less than 1% from its bulk value. The van der Waals gap between the first and second Se-Sn-Se sandwich layer, d_{34}, remains almost the same as its bulk. However, due to the limited accessible energy range (28-133 eV), a meaningful final R-factor was not quantified

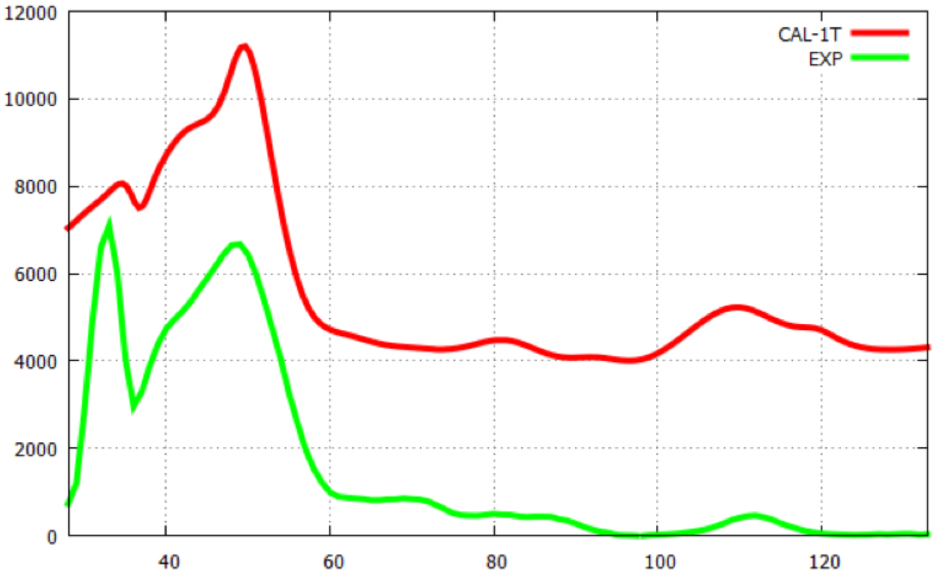

Figure 6-7: Calculated LEED-*IV* curves for the (00) diffraction beam for an optimized 1T phase $SnSe_2$ surface (red solid curve) and the measured electron reflectivity curve (green solid curve).

Table 6.2: Calculated optimum top few layer spacings d_{ij} between the ith and jth atomic planes (see Fig. 6-8) for a $SnSe_2$ thin film surface and the relative deviation with respect to the bulk layer spacing d_0

Parameters	Optimized values (Å)	$\Delta d_{ij}/d_0$
d_{12}	1.52	−3.1%
d_{23}	1.62	+3.7%
d_{34}	3.00	−0.1%

here.

6.3.3 Conclusion

In summary, I have determined that the grown bi-layer $SnSe_2$ thin film is 1T phase using the non-destructive LEED-*IV* technique. The atomic crystal structure was determined using the dynamical LEED-*IV* analysis. It is found that the surface of $SnSe_2$ remains mostly the same as its bulk while the surface also undergoes slight interlayer relaxation. This is expected for layered materials with weak van der Waals interaction between the surface

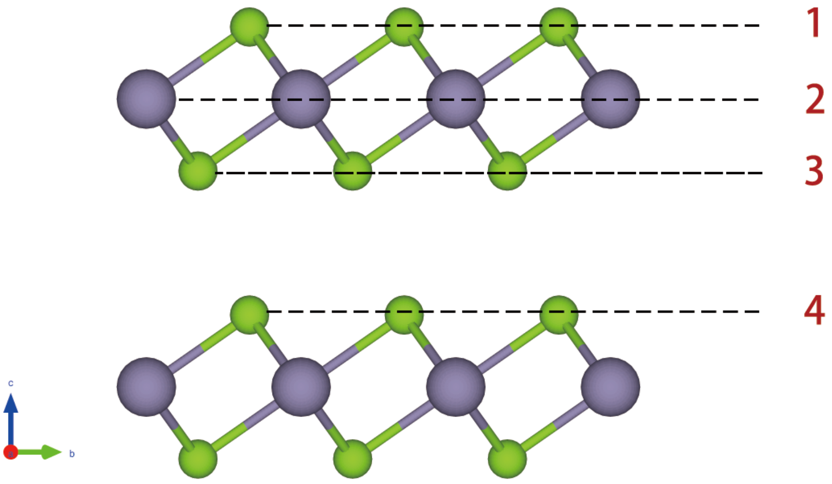

Figure 6-8: Side view of surface structure 1T-$SnSe_2$.

layer and its bulk, which is similar to our previous find in MoS_2 [41].

CHAPTER 7

W-DOPING INDUCED 2H-$\mathrm{MoTe_2}$ TO T_d-$\mathrm{MoTe_2}$ PHASE TRANSITION

7.1 Introduction

Besides the common 2H and 1T-phase, TMDs also host various less common phases such as an 1T' and T_d-phase. Slightly different from the 1T-phase, the 1T'-phase has a distorted octahedral structure with an inclined stacking angle of $\sim$93.9°, which retains a centrosymmetric P21/m space group. The T_d-phase is very similar to the 1T'-phase except a slightly different stacking angle of 90°, which breaks the inversion symmetry (space group Pmn21) [147]. The extremely large magnetoresistance found in T_d-$\mathrm{WTe_2}$ [148, 149] has triggered major interest in magnetic field sensors in atomically thin dimensions. From the fundamental physics perspective, the T_d phase of $\mathrm{WTe_2}$ and $\mathrm{MoTe_2}$ materials have been predicted to be promising candidates for realizing a new type-II of Weyl fermions. Weyl fermions were first realized in the Weyl semimetals of the TaAs family [150, 151]. The signature of these type-I Weyl fermions is the existence of two separated Weyl points with opposite chirality, which are connected by topological Fermi arcs on the surface. Unlike type-I Weyl fermions, the type-II Weyl fermions are characterized by the existence of touching points between the electron- and hole-pocket with strongly tilted Weyl cones [152]. Besides the potential device applications and presence of novel physics phenomena, the precise control and engineering of different phases are of great interests. Previously, our collaborators have reported that by doping W in 2H-$MoTe_2$, it can induce a phase transition to the T_d phase at a doping level of above x_c=10%. Presented in this chapter, I use the dynamical LEED-IV technique to investigate structural change in the phase transition. The evolution of the $MoTe_2$ electronic structure due to different W-doping level is also studied using ARPES measurements, conducted by collaborators, and the interplay between the structural change and electronic structure difference will be discussed.

7.2 LEED-*IV* Analysis

μLEED measurements were performed at the Center for Functional Nanomaterials, Brookhaven National Laboratory using the ELMITEC AC-LEEM system. In this system, the sample was cleaved in-situ at room temperature. The lattice constants of WTe_2 are a=6.282 Å, b=3.496 Å and c=14.07 Å [153]. The lattice constants of $MoTe_2$ are a=6.335 Å, b=3.477 Å and c=13.883 Å [154]. As the lattice constant differences between $MoTe_2$ and WTe_2 are less than 1.5%, and the atomic scattering feature are close to each other, I used the weighted average as the lattice constants for the $Mo_{1-x}W_xTe_2$ alloys. The Debye temperature for $Mo_{1-x}W_xTe_2$ was set as 210 K. The inner potential of $Mo_{1-x}W_xTe_2$ was set as 10.1 eV. Twelve (L=11) phase shifts were used in the calculation. The well-defined hexagonal μLEED pattern (see Fig. 7-1(b)) acquired from $x = 0.08$ alloy demonstrates that the alloys with $x < x_c$ crystallize in the 2H-phase. In contrast, the rectangular μLEED pattern (Fig. 7-1(e)) for a composition of x= 0.16 show that moderate W substitution ($x > x_c$) stabilized the T_d-phase at room temperature. Note that multiple locations were surveyed across the sample surface, and no evidence of phase coexistence was observed. Furthermore, dynamical LEED-IV analysis was used to study the surface relaxations of different

Table 7.1: Calculated optimum top few layer spacings d_{ij} between the ith and jth atomic planes (see Fig. 7-2 (a)) for a 2H-$Mo_{0.92}W_{0.08}Te_2$ and the relative deviation with respect to the bulk layer spacing d_0

Parameters	Optimized values (Å)	$\Delta d_{ij}/d_0$
d_{12}	1.816	+1.6%
d_{23}	1.899	+6.0%
d_{34}	3.374	+0.4%

$Mo_{1-x}W_xTe_2$ alloys. The optimized surface structure for the 2H and T_d-phases samples were presented in Tab. 7.1 and 7.2. Specifically, for 2H-$Mo_{0.94}W_{0.06}Te_2$, the top sandwich layer undergoes a slight expansion comparing to the bulk. Specifically, the first Te-Mo layer spacing, d_{12}, is expanded by about 1.6% and the second Mo-Te layer spacing, d_{23}, is expanded by about 6%. The total thickness of the first Te-Mo-Te sandwich layer, d_{13}, is expanded by approximately 7.6% comparing to the bulk. The layer spacing between the first and second Te-Mo-Te sandwich layer, d_{34}, is expanded slightly by about 0.4%. For the T_d-$Mo_{0.84}W_{0.16}Te_2$, each sandwich layer is consists of six inequivalent atomic planes. The layer spacing between each atomic planes, d_{ij}, and the spacing between the first and second sandwich layer d_{67} were optimized. As presented in Tab. 7.2, d_{12} is contracted by about 0.05 Å; d_{23} is expanded by about 0.07 Å; d_{34} is expanded by about 0.11 Å; d_{45} is contracted by about 0.17 Å; d_{56} is contracted by about 0.14 Å. The layer spacing between the top two sandwich layers, d_{67} is expanded by about 10% comparing to the bulk value. Note that the T_d-phase possesses less symmetry and is energitically less stable than the 2H-phase, the lattice distortion and relaxation on the surface is as expected to be more dramatic than the 2H-phase surface. As shown in Fig. 7-1 (c) and (e), the calculated IV curves with optimized structure match well with experimental curves, for both 2H and T_d-phase of $Mo_{1-x}W_xTe_2$. The good agreement of the IV curves further confirms the respective phase of the samples with different doping level.

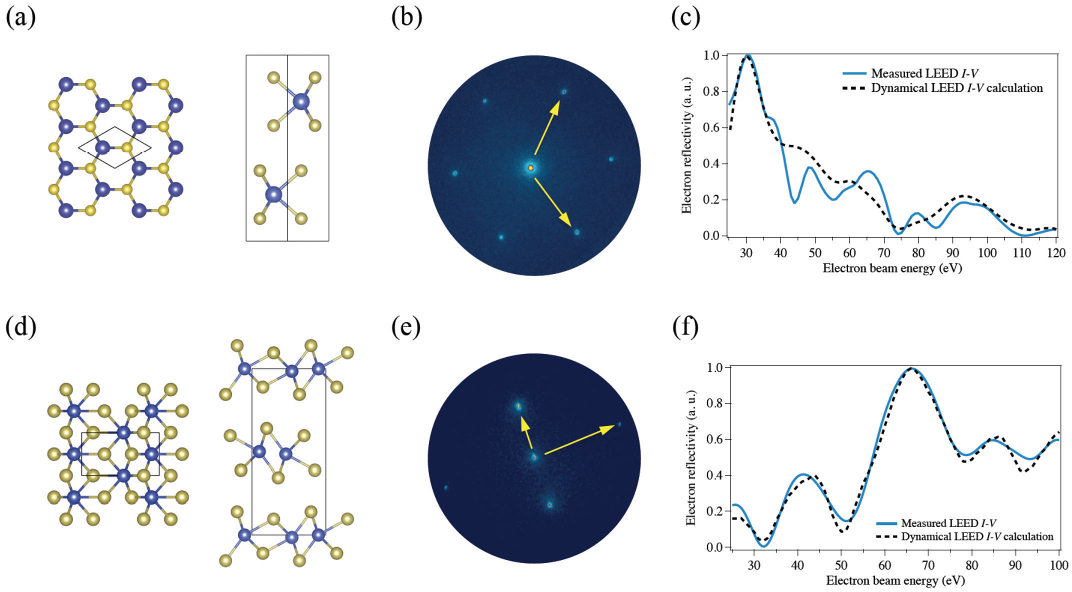

Figure 7-1: Crystalline structure of 2H- and T$_d$- Mo$_{1-x}$W$_x$Te$_2$ crystals. (a) Schematic of 2H-phase atomic structure in top view (left) and sideview (right), (b) LEED pattern, and (c) μLEED-IV curve for 2H-Mo$_{0.92}$W$_{0.08}$Te$_2$. (d) Top view (left) and a side view (right) schematic of T$_d$-phase atomic structure, (e) LEED pattern, and (f) μLEED-IV curve for T$_d$-Mo$_{0.84}$W$_{0.16}$Te$_2$. Blue spheres: Mo/W atoms; yellow spheres: Te atoms.

Table 7.2: Calculated optimum top few layer spacings d$_{ij}$ between the ith and jth atomic planes (see Fig. 7-2 (b)) for the T$_d$-T$_d$-Mo$_{0.84}$W$_{0.16}$Te$_2$ surface and the relative optimized parameter deviation with respect to the bulk layer spacing. d_0

Parameters	Optimized values (Å)	Bulk values	$\Delta d_{ij}/d_0$
d$_{12}$	0.55	0.60	−8.3%
d$_{23}$	1.43	1.36	+5.1%
d$_{34}$	0.33	0.20	+65%
d$_{45}$	1.19	1.36	−12.5%
d$_{56}$	0.46	0.60	−23.3%
d$_{67}$	3.12	2.83	+10.2%

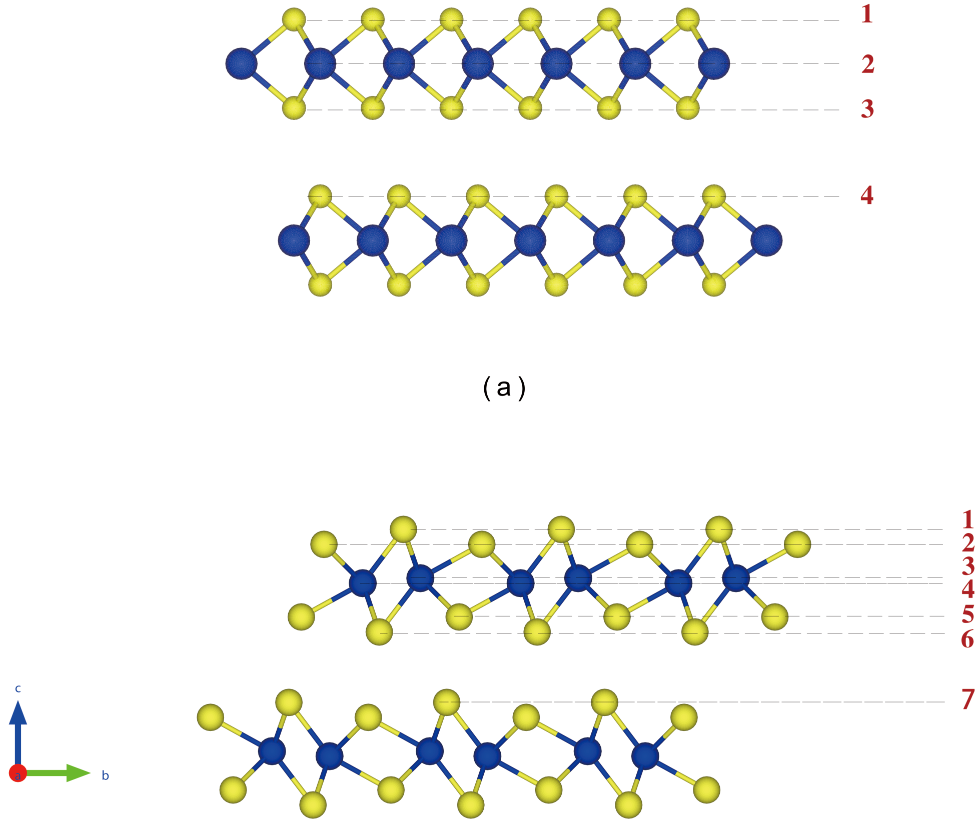

(a)

(b)

Figure 7-2: Side view of surface crystalline structure of (a) 2H- and (b)T_d- $MoTe_2$. (Blue spheres: Mo atoms; yellow spheres: Te atoms.

7.3 Electronic Structures

ARPES measurements were then used to investigate the electronic structure of $\mathrm{Mo}_{1-x}\mathrm{W}_x\mathrm{Te}_2$ alloys. The ARPES measurements were carried out by our collaborators Dr. Wencan Jin, at the Dreamline beamline of the Shanghai Synchrotron Radiation Facility (SSRF). The measurements were made at low temperature, typically 50 K. Figure. 7-3 (a) shows the ARPES bandmap of 2H-$\mathrm{Mo}_{0.94}\mathrm{W}_{0.06}\mathrm{Te}_2$ alloy along $\overline{K} - \overline{\Gamma} - \overline{K}$ high-symmetry direction of the surface Brillouin zone (see inset). The maxima in the corresponding integrated spectrum (Fig. 7-3 (b)) shows that the main band features are derived from the Mo d_{z^2} and the Te p_z orbitals. Conduction bands were not observed at energies within 1 eV above the valence-band maximum (VBM), confirming that the 2H-phase is semiconducting with a gap size $>$ 1 eV. The band features are further displayed in the corresponding energy distribution curves (EDCs) plots in Fig. 7-3 (c). In the T_d-phase ($x = 0.2$), the ARPES bandmap (Fig. 7-3 (e)) along the $\overline{Y} - \overline{\Gamma} - \overline{Y}$ (Fig. 7-3 (d)) high symmetry direction shows a metallic nature, in which a hole band (yellow arrow, α) and electron pocket (white arrow, β) across Fermi level. Figure 7-3 (g) shows the stack of constant-energy maps. Note that a palmier-shaped hole pocket and an almond-shaped electron pocket are observed in the Fermi surface ($E = E_F$) map.

In addition, the electronic structure evolution of the T_d phase was studied as a function of W concentration. A side-by-side comparison of the electronic structure was made between $x = 0.16$, $x = 0.20$, and $x = 0.27$. As shown in the ARPES bandmaps and the corresponding second derivative plots in Fig. 7-4 (a)-(c), the overlap in energy between the valence and conduction bands decreases with increasing W concentration. Such overlap is characterized by the energy position of the conduction band minimum (CBM), as shown in the EDC plots (Fig. 7-4 (d)). The CBM of $x = 0.16$ is located at $\sim$ 50 meV, which is comparable with that in pure T_d-MoTe_2 (60meV) [155]. It is striking that the overlap in the $x = 0.27$ alloy

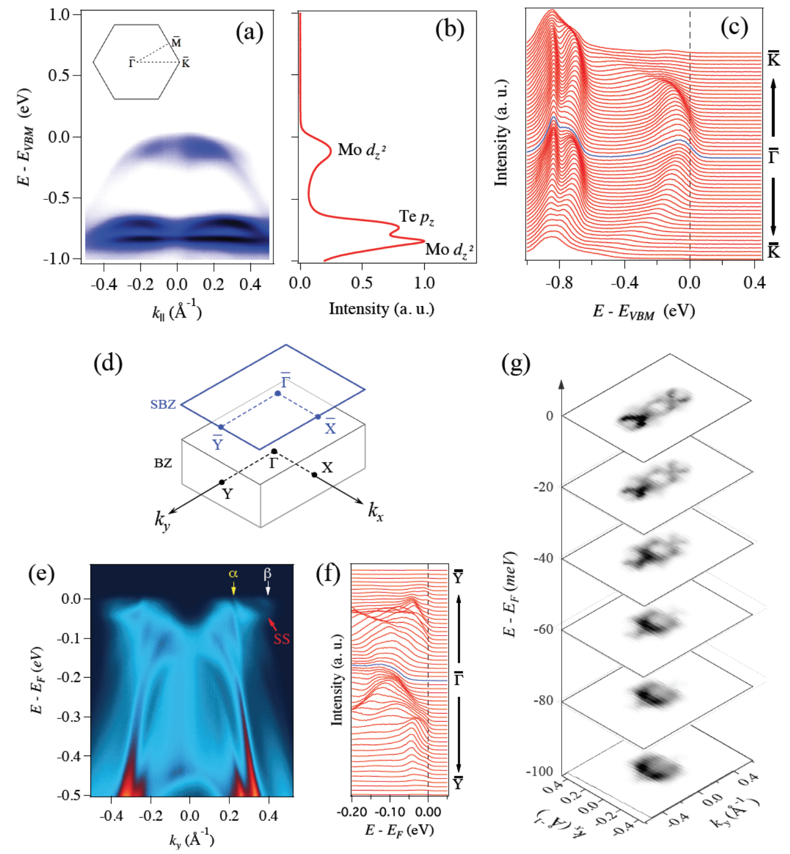

Figure 7-3: Electronic structure of Mo$_{1-x}$W$_x$Te$_2$ alloys for certain critical W concentrations. Electronic structure of 2H-Mo$_{0.94}$W$_{0.06}$Te$_2$ alloy (a) ARPES bandmap along the $\overline{K} - \overline{\Gamma} - \overline{K}$ high symmetry direction, the inset shows the surface Brillouin zone (b) Integrated spectrum and (c) EDCs plot of ARPES bandmap shown in (a). Electronic structure of T$_d$-Mo$_{0.84}$W$_{0.16}$Te$_2$ alloy (d) the bulk Brillouin zone (BZ) and projected (001) surface Brillouin zone (SBZ), (e) ARPES bandmap (hγ= 24 eV) along $\overline{Y} - \overline{\Gamma} - \overline{Y}$ high symmetry direction, (e) EDCs plot of band features near Fermi level (E$_F$), and (g) a stack of constant energy maps.

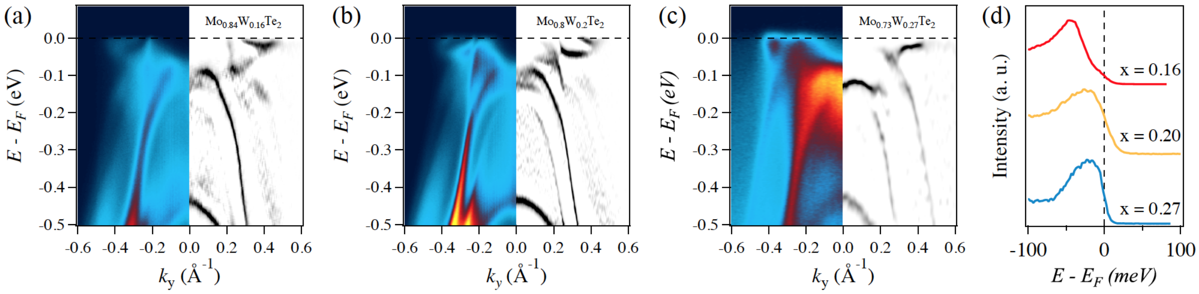

Figure 7-4: Electronic structure evolution of T$_d$- Mo$_{1-x}$W$_x$Te$_2$ alloys with W concentration. ARPES bandmap (left) and the corresponding second-derivative intensity plot (right) of T$_d$-Mo$_{1-x}$W$_x$Te$_2$ alloys along $\overline{Y}-\overline{\Gamma}-\overline{Y}$ high symmetry direction with (a) $x = 0.16$, (b) $x = 0.20$, and (c) $x = 0.27$. (d) The corresponding EDCs across the conduction band minimum.

is significantly suppressed, given the large content of Mo relative to W that is present.

7.4 Conclusion

I characterized the surface crystal structure for Mo$_{1-x}$W$_x$Te$_2$ at different doping levels. Below the critical doping level, Mo$_{0.94}$W$_{0.08}$Te$_2$ is determined to crystallize in 2H-phase. The surface undergoes a slight expansion comparing to the bulk. This is likely due to the surface symmetry breaking, which introduced more freedom to the lattice structure. Above the critical doping level, Mo$_{0.84}$W$_{0.16}$Te$_2$ is found to crystallize in the T$_d$-phase at room temperature. Below the critical doping level, 2H-Mo$_{0.94}$W$_{0.06}$Te$_2$ surface was found to remain mostly the same as bulk crystal structure while undergoes a slight surface sandwich layer expansion. On the other hand, the T$_d$-phase surface undergoes a more dramatic layer relaxation and structure distortion than the 2H-phase, likely due to less symmetry and less structure stability. The characteristic feature of type-II semimetal, which are the electron and hole pockets across Fermi level, are observed in the T$_d$-Mo$_{1-x}$W$_x$Te$_2$ (x=0.2) alloy using ARPES measurements. The evolution of the electronic structure of the T$_d$-phase was studied using samples with various W-doping level. At doping level of x=0.16, the measured conduction band minimum is found to be comparable to that in the pure T$_d$-

$MoTe_2$. The CBM is found to shift upward which results in the reduce of overlapping of the conduction band and valence band. The detailed surface structural information regarding the 2H and T_d-phase $Mo_{1-x}W_xTe_2$ alloy, along with electronic structure measurements provide important fundamental input for a better understanding of the exotic properties observed in these materials.

CHAPTER 8

CONCLUSIONS

To summarize, I have used dynamical μLEED-IV analysis to study the surface crystal structure of various 2D materials. 2D materials are commonly prepared through mechanical exfoliation, which limits the available sample size down to a few micron. A surface structural characterization is very challenging due to this limited sampling area. I have shown in this thesis that the unique μLEED technique, with its local μm-size sampling and high surface sensitivity, is a powerful tool for the structural characterization of exfoliated 2D materials. Furthermore, due to the low energy and non-destructive nature of the probing electrons in LEED, I was able to determine the detailed surface structure of some of these meta-stable materials for the first time, *i.e.* black phosphorus and MBE grown rock-salt structure SnSe. The main results of the presented studies are summarized in the following:

- Surface of Bulk MoS_2 [41]

The surface structure of bulk 2H-MoS_2 remains mostly the same as bulk structure with a slight contraction of the thickness of the top S-Mo-S sandwich layer and an slight expansion of the first van der Waals gap. And the structure was found to be slightly different at elevated experimental temperature of 320 K, comparing to the previously reported surface structure at 95 K. Specifically, the interlayer spacing between the very top S atomic layer and the first Mo layer, d_{12}, has a smaller contraction of 2.5% at 320 K than at 95 K. The layer spacing between the first Mo atomic layer and the second S layer, d_{23}, has a small contraction of 1.3% from the bulk. I also showed that the layer spacing between the first S-Mo-S sandwich layer and the second sandwich layer, d_{34}, has an small expansion of 1.3% at 320 K compared to a contraction at 95 K.

- Suspended Monolayer MoS_2 Flake [41]

The monolayer MoS_2 flake was exfoliated onto a Si substrate with drilled holes of 5 μm, to create a suspended monolayer MoS_2 flake. For an isolated monolayer of MoS_2, one would expect that the two layer spacings, first S-Mo interlayer spacing (d_{12}) and second Mo-S interlayer spacing (d_{23}) to be identical, since the molybdenum layer is centered between the two sulfur layers, as in the bulk crystalline structure. On the contrary, the suspended monolayer MoS_2 was found to have asymmetry atomic layer spacing. Specifically, the first interlayer spacing d_{12} is slightly expanded by 1.3% compared to the bulk value while the second interlayer spacing d_{23} is contracted by 5.1% compared to the bulk value. The slight asymmetry of the interlayer spacings might be due to a small amount of warping or strain of the suspended monolayer caused by the edge of the hole on the substrate.

- Surface of Black Phosphorus [42]

A major issue that hinders the further advancement of black phosphorus research is its fast oxidization in air. Previously, it was considered to have a 30 mins oxidization window, within which, the surface of BP can be considered as pristine and suit for further studies. However, in our LEED studies, we found that the surface of exfoliated BP flakes are quickly oxidized even within 5 mins exposure in air. Careful thermal annealing investigation was conducted for exfoliated BP samples. It was found that, by annealing at 250°C to 370°C, the oxide layer can be efficiently removed. The surface structure of the pristine BP was then studied using the dynamical μLEED-IV analysis. A significant surface buckling was found on the pristine BP surface. Specifically, it was found to be 0.22 Å for the cleaved bulk flake and 0.30 Å for the 10 nm thick few layer phosphorene flake. A similar buckling for the second phosphorus layer was identified, which is accessible by high subsurface sensitive μLEED-*IV*. These surface buckling values are all one order of magnitude higher than previously proposed value by theory. Further DFT calculations was carried out by collaborator, Dr. Jie-Xiang Yu, to study the origin of this surface buckling and its influence on the electronic properties of BP. DFT calculations indicate that, the significant buckling is likely induced by the surface vacancy defects. The surface buckling was also found to introduce an increase in the bandgap of both monolayer and bi-layer phosphorene. Specifically, the bandgaps increase from 1.59 eV to 2.30 eV for monolayer and from 0.95 eV to 1.67 eV for bi-layer phosphorene when a buckling of 0.4 Å is introduced in the top layer.

- Surface of rock-Salt SnSe and 1T $SnSe_2$ [43, 44]

The MBE grown Rock-salt SnSe is a meta-stable material. It was reported that, high energy probing technique, such as TEM would induce a phase transition and are thus not suitable for its structure studies. Furthermore the topological properties of this material is strongly dependent on the surface termination element. While the other surface characterization technique failed to identify the element of the very top layer, the μLEED-*IV* analysis was able to differentiate the different surface termination elements. Using this technique, it was shown that the grown SnSe(111) surface has a pristine Sn-terminated surface. It was further identified that the surface undergoes an oscillatory, contraction-expansion-contraction structural relaxation. This oscillatory surface relaxation also provides a mechanism to balance the surface dipole and thus stabilize the structure.

Similar to SnSe, 1T $SnSe_2$ could potentially undergo a beam-induced phase transformation if probed using high energy characterization techniques. Using the non-destructive μLEED-*IV* technique, the surface of the 1T $SnSe_2$ thin film was found to remain mostly the same as its bulk while undergo a slight surface interlayer relaxation. This is expected for layered materials with weak van der Waals interaction between the surface layer and its bulk. Specifically, the interlayer spacing between the top Se atomic layer and the Sn atomic layer, d_{12}, was found to have a slight contraction of about 3%, comparing to the bulk value. The interlayer spacing between the Sn atomic layer and the second Se atomic layer, d_{23}, was found to expand slightly by about 4% from its bulk value. The thickness of the first Se-Sn-Se sandwich layer $d_{13}=d_{12}+d_{23}$, is only dilated by less than 1% from its bulk value. The van der Waals gap between the first and second Se-Sn-Se sandwich layer, d_{34}, remains almost the same as its bulk.

- W-doping Induced 2H-$MoTe_2$ to T_d-$MoTe_2$ Phase Transition [45]

It was reported previously that, by doping W in 2H-$MoTe_2$ above a critical level of about 8%, it induces a phase transition to the T_d phase. T_d-$MoTe_2$ was predicted to be a Type-II Weyl semimetal, which hosts various exotic physics phenomena. Using μLEED, $Mo_{0.94}W_{0.06}Te_2$ alloy was identified to crystallize in 2H phase and $Mo_{0.84}W_{0.16}Te_2$ was identified to crystallize in T_d phase. The 2H-$Mo_{0.94}W_{0.06}Te_2$ was found to remain mostly the same as bulk crystal structure while undergoes a slight surface sandwich layer expansion. On the other hand, the T_d phase surface undergoes a more dramatic layer relaxation and structure distortion than the 2H phase, likely due to less symmetry and less structure stability.

- Advancement of LEED-*IV* Technique: Parallelization of *leedcs* and Enabling HPC

In order to take advantage of the calculation power of modern supercomputers, the outdated original Visual Basic package LEEDopt was rewritten in Fortran 90 to enable the high performance computing on supercomputers. The new optimization program *pleedopt* was proven to converge to the results as the original package. *leedcs*, which calculates the composite layer scattering matrix, would become time-consuming and sometimes unrealistic when calculating structures with large super cell. In this thesis, *leedcs* was successfully parallelized using OpenMP and was shown to improve the calculation speed by approximately 14 times when run on supercomputer Trillian, at the University of New Hampshire.

Bibliography

[1] A. H. C. Neto, F. Guinea, N. M. R. Peres, K. S. Novoselov, A. K. Geim, The electronic properties of graphene, Rev. Mod. Phys. 81 (2009) 109.

[2] J. Sun, Surface Structure and Composition Determination by Low-Energy Electron Scattering and Monte Carlo Simulations, Ph.D Thesis, University of New Hampshire, 2008.

[3] M. P. Seah, W. A. Dench, Quantitative electron spectroscopy of surfaces: A standard data base for electron inelastic mean free paths in solids, Surf. Interface Anal. 1 (1979) 2–11.

[4] E. A. Soares, C. M. C. de Castilho, V. E. de Carvalho, Advances on surface structural determination by LEED, J. Phys.: Condens. Matter 23 (2011) 303001.

[5] D. L. Adams, A simple and effective procedure for the refinement of surface structure in leed, Surf. Sci. 519 (2002) 157–172.

[6] B. J. Mrstik, R. Kaplan, T. L. Reinecke, M. V. Hove, S. Y. Tong, Surface−structure determination of the layered compounds MoS_2 and $NbSe_2$ by low−energy electron diffraction, Phys. Rev. B 15 (1977) 897.

[7] R. P. Feynman, There is plenty of room at the bottom, Lecture at APS Meeting at Caltech.

[8] P. R. Wallace, The band theory of graphite, Phys. Rev. 71 (1947) 622.

[9] R. E. Peierls, Ann. I. H. Poincare 5 (1935) 177.

[10] L. D. Landau, The theory of phase transformations, Phys. Z. Sowjetunion 11 (1937) 26.

[11] N. D. Mermin, Crystalline order in two dimensions, Phys. Rev. 176 (1968) 250.

[12] M. S. Dresselhaus, G. Dresselhaus, Intercalation compounds of graphite, Adv. Phys. 51 (2002) 1.

[13] T. A. Land, T. Michely, R. J. Behm, J. C. Hemminger, G. Coms, STM investigation of single layer graphite structures produced on Pt(111) by hydrocarbon decomposition, Surf. Sci. 264 (1992) 261.

[14] A. Nagashima, K. Nuka, H. Itoh, T. Ichinokawa, C. Oshima, S. Otani, Electronic states of monolayer graphite formed on TiC(111) surface, Surf. Sci. 291 (1993) 93.

[15] A. J. Van Bommel, J. E. Crombeen, A. Van Tooren, LEED and Auger electron observations of the SiC(0001) surface, Surf. Sci. 48 (1975) 463.

[16] I. Forbeaux, J.-M. Themlin, J.-M. Debever, Heteroepitaxial graphite on 6H−SiC(0001) interface formation through conduction-band electronic structure, Phys. Rev. B 58 (1998) 16396.

[17] A. K. Geim, Nobel lecture: Random walk to graphene, Rev. Mod. Phys. 83 (2011) 851.

[18] K. S. Novoselov, A. K. Geim, S. V. Morozov, D. Jiang, Y. Zhang, S. V. Dubonos, I. V. Grigorieva, A. A. Firsov, Electric field effect in atomically thin carbon films, Science 306 (2004) 666.

[19] S. Z. Butler, S. M. Hollen, L. Cao, Y. Cui, J. A. Gupta, H. R. Gutiérrez, T. F. Heinz, S. S. Hong, J. Huang, A. F. Ismach, E. Johnston-Halperin, M. Kuno, V. V. Plashnitsa, R. D. Robinson, R. S. Ruoff, S. Salahuddin, J. Shan, L. Shi, M. G. Spencer, M. Terrones, W. Windl, J. E. Goldberger, Progress, challenges, and opportunities in two−dimensional materials beyond graphene, ACS Nano 7 (4) (2013) 2898–2926.

[20] A. S. Mayorov, R. V. Gorbachev, S. V. Morozov, L. Britnell, R. Jalil, L. A. Ponomarenko, P. Blake, K. S. Novoselov, K. Watanabe, T. Taniguchi, A. K. Geim, Micrometer-scale ballistic transport in encapsulated graphene at room temperature, Nano Lett. 11(6) (2011) 2396.

[21] E. Stolyarova, K. T. Rim, S. Ryu, J. Maultzsch, P. Kim, L. E. Brus, T. F. Heinz, M. S. Hybertsen, G. W. Flynn, High−resolution scanning tunneling microscopy imaging of mesoscopic graphene sheets on an insulating surface, Proc. Natl. Acad. Sci. U.S.A. 104 (2007) 9209.

[22] C. Lee, X. Wei, J. W. Kysar, J. Hone, Measurement of the elastic properties and intrinsic strength of monolayer graphene, Science 321 (2008) 5887.

[23] K. S. Novoselov, V. I. Falko, L. Colombo, P. R. Gellert, M. G. Schwab, K. Kim, A roadmap for graphene, Nature 490 (2012) 192.

[24] J. S. Bunch, S. S. Verbridge, J. S. Alden, A. M. van der Zande, J. M. Parpia, H. G. Craighead, P. L. McEuen, Impermeable atomic membranes from graphene sheets, Nano Lett. 8(8) (2008) 2458.

[25] Y. Shao, J. Wang, H. Wu, J. Liu, I. Aksay, Y. Lin, Graphene based electrochemical sensors and biosensors: A review, Electroanalysis 22 (2010) 1027.

[26] X. Wang, L. Zhi, K. Müllen, Transparent, conductive graphene electrodes for dye-sensitized solar cells, Nano Lett. 8(1) (2008) 323.

[27] S.-S. Li, K.-H. Tu, C.-C. Lin, C.-W. Chen, M. Chhowalla, Solution−processable graphene oxide as an efficient hole transport layer in polymer solar cells, ACS Nano 4(6) (2010) 3169.

[28] S. Yang, X. Feng, S. Ivanovici, K. Müllen, Fabrication of grapheneencapsulated oxide nanoparticles: Towards highperformance anode materials for lithium storage, Angew. Chem. Int. Edn. 49 (2010) 8408.

[29] E. Yoo, J. Kim, E. Hosono, H. shen Zhou, T. Kudo, I. Honma, Large reversible Li storage of graphene nanosheet families for use in rechargeable lithium ion batteries, Nano Lett. 8(8) (2008) 2277.

[30] T.-H. Han, Y. Lee, M.-R. Choi, S.-H. Woo, S.-H. Bae, B. H. Hong, J.-H. Ahn, T.-W. Lee, Extremely efficient flexible organic light-emitting diodes with modified graphene anode, Nature Photon. 6 (2012) 105.

[31] B. Radisavljevic, A. Radenovic, J. Brivio, V. Giacometti, A. Kis, Single−layer MoS_2 transistors, Nat. Nanotechnol. 6 (2011) 147–150.

[32] M. Fontana, T. Deppe, A. K. Boyd, M. Rinzan, A. Y. Liu, M. Paranjape, P. Barbara, Electron−hole transport and photovoltaic effect in gated MoS_2 Schottky junctions, Sci. Report. 3 (2013) 1634.

[33] X. Xu, J. Hu, Z. Yin, C. Xu, Photoanode current of large-area MoS_2 ultrathin nanosheets with vertically meshshaped structure on indium tin oxide, ACS Appl. Mater. Interfaces 6(8) (2014) 5983–5987.

[34] V. Tran, R. Soklaski, Y. Liang, L. Yang, Layer-controlled band gap and anisotropic excitons in few-layer black phosphorus, Phys. Rev. B 89 (2014) 235319.

[35] L. Li, Y. Yu, G. J. Ye, Q. Ge, X. Ou, H. Wu, D. Feng, X. H. Chen, Y. Zhang, Black phosphorus field-effect transistors, Nat. Nanotechnol. 9 (2014) 372.

[36] F. Xia, H. Wang, Y. Jia, Rediscovering black phosphorus as an anisotropic layered material for optoelectronics and electronics, Nat. Commun. 5 (2014) 4458.

[37] H. Liu, A. T. Neal, Z. Zhu, Z. Luo, X. Xu, D. Tománek, P. D. Ye, Phosphorene: An unexplored 2D semiconductor with a high hole mobility, ACS Nano 8 (2014) 4033.

[38] H. Wang, X. Wang, F. Xia, L. Wang, H. Jiang, Q. Xia, M. L. Chin, M. Dubey, S. Han, Black phosphorus radio-frequency transistors, Nano Lett. 14 (2014) 6424.

[39] Y. Deng, Z. Luo, N. J. Conrad, H. Liu, Y. Gong, S. Najmaei, P. M. Ajayan, J. Lou, X. Xu, P. D. Ye, Black phosphorus monolayer MoS_2 van der Waals heterojunction pn diode, ACS Nano 8 (2014) 8292.

[40] M. Buscema, D. J. Groenendijk, G. A. Steele, Herre S.J. van der Zant, A. Castellanos-Gomez, Photovoltaic effect in few-layer black phosphorus PN junctions defined by local electrostatic gating, Nat. Commun. 5 (2014) 4651.

[41] Z. Dai, W. Jin, M. Grady, J. T. Sadowski, J. I. Dadap, R. M. Osgood, Jr, K. Pohl, Surface structure of bulk $2H-MoS_2(0001)$ and exfoliated suspended monolayer MoS_2: a selected area low energy electron diffraction study, Surf. Sci. 660 (2017) 16.

[42] Z. Dai, W. Jin, J.-X. Yu, M. Grady, J. T. Sadowski, Y. D. Kim, J. Hone, J. I. Dadap, J. Zang, R. M. Osgood, K. Pohl, Surface buckling of black phosphorus: Determination, origin, and influence on electronic structure, Phys. Rev. Mater. 1 (2017) 074003.

[43] W. Jin, S. Vishwanath, J. Liu, L. Kong, R. Lou, Z. Dai, J. T. Sadowski, X. Liu, H.-H. Lien, J. Ma, T. Qian, J. I. Dadap, K. Pohl, S. Wang, J. Furdyna, H. Ding, H. G. Xing, R. M. Osgood, Jr, Electronic structure of the metastable epitaxial rock-salt SnSe(111) topological crystalline insulator, Physical Reivew X 7 (2017) 041020.

[44] Z. Dai, W. Jin, M. Grady, J. T. Sadowski, S. Vishwanath, H. G. Xing, R. M. Osgood, K. Pohl, Surface structure of $1T-SnSe_2$, In Preparation.

[45] W. Jin, T. Schiros, Y. Lin, J. Ma, Z. Dai, , J. Yu, D. Rhodes, J. T. Sadowski, X. Tong, T. Qian, J. I. Dadap, S. Wang, J. Zang, K. Pohl, H. Ding, J. Hone, L. Balicas, A. N. Pasupathy, R. M. Osgood, Phase transition and electron structure evolution of $\mathrm{MoTe_2}$ induced by W substitution, In Preparation.

[46] L. de Broglie, Ondes de quanta, C. R. Acad. Sci. 177 (1923) 517, 548, 630.

[47] C. Davisson, L. H. Germer, The scattering of electrons by a single crystal of Nickel, Nature 119 (1927) 558.

[48] C. Davisson, L. H. Germer, Diffraction of electrons by a crystal of Nickel, Phys. Rev. 30 (1927) 705.

[49] G. P. Thomson, A. Reid, Diffraction of cathode rays by a thin film, Nature 119 (1927) 890.

[50] E. Bauer, Electron Microscopy, Academic Press, Inc. (New York), 1962.

[51] E. Bauer, Low energy electron microscopy, Rep. Prog. Phys. 57 (1994) 895.

[52] E. Bauer, LEEM basics, Surf. Rev. Lett. 5 (1998) 1275.

[53] R. M. Tromp, Low-energy electron microscopy, IBM J. Res. Dev. 44 (2000) 503.

[54] A. K. Schmid, R. J. Phaneuf, Low-energy electron microscopy: Imaging surface dynamics, Phys. Today 56(3) (2003) 50.

[55] W. Telieps, E. Bauer, An analytical reflection and emission UHV surface electron microscope, Ultramicroscopy 17 (1985) 57.

[56] J. B. Pendry, Low-Energy Electron Diffraction, Academic (London), 1974.

[57] M. A. Van Hove, W. H. Weinberg, C.-M. Chan, Low-Energy Electron Diffraction, Springer-Verlag, 1986.

[58] M. A. Van Hove, S. Y. Tong, Surface Crystallography by LEED, Springer-Verlag (Berlin), 1979.

[59] R. J. Hanson, F. T. Krogh, A quadratic-tensor model algorithm for nonlinear least-squares problems with linear constraints, ACM Trans. Math. Softw. 18 (1992) 115–133.

[60] A. Barbieri, M. A. V. Hove, private communication (Last Accessed May 2018) http://www.icts.hkbu.edu.hk/vanhove/.

[61] J. Sun, J. B. Hannon, G. L. Kellogg, K. Pohl, Local structural and compositional determination via electron scattering: Heterogeneous Cu(001)−Pd surface alloy, Phys. Rev. B 76 (2007) 205414.

[62] H. L. Davis, J. R. Noonan, Cu(100) multilayer relaxation, J. Vac. Sci. Technol. 20 (1982) 842.

[63] D. M. Lind, F. B. Dunning, G. K. Walters, H. L. Davis, Surface-structural analysis by use of spin-polarized low-energy electron diffraction: An investigation of the Cu(100) surface, Phys. Rev. B 35 (1987) 9037.

[64] Q. T. Jiang, P. Fenter, T. Gustafsson, Geometric structure and surface vibrations of Cu(001) determined by medium-energy ion scattering, Phys. Rev. B 44 (1991) 5773.

[65] T. Böker, R. Severin, A. Müller, C. Janowitz, R. Manzke, D. Voß, P. Krüger, A. Mazur, J. Pollmann, Band structure of MoS_2, $MoSe_2$, and $\alpha MoTe_2$: Angle-resolved photoelectron spectroscopy and *ab initio* calculations, Phys. Rev. B 64 (2001) 235305.

[66] Y. Fu, X. Feng, M. Yan, K. Wang, S. Wang, First principle study on electronic structure and optical phonon properties of $2H-MoS_2$, Physica B: Condensed Matter 426 (2013) 103–107.

[67] R. Coehoorn, C. Haas, J. Dijkstra, C. Flipse, R. de Groot, A. Wold, Electronic structure of $MoSe_2$, MoS_2, and WSe_2. I. Band−structure calculations and photoelectron spectroscopy, Phys. Rev. B 35 (1987) 6195.

[68] S. W. Han, G.-B. Cha, E. Frantzeskakis, I. Razado-Colambo, J. Avila, Y. S. Park, D. Kim, J. Hwang, J. S. Kang, S. Ryu, W. S. Yun, S. C. Hong, M. C. Asensio, Band−gap expansion in the surface−localized electronic structure of $MoS_2(0002)$, Phys. Rev. B 86 (2012) 115105.

[69] S. K. Mahatha, K. S. Menon, Inhomogeneous band bending on $MoS_2(0001)$ arising from surface steps and dislocations, J. Phys. Condens. Matter 24 (2012) 305502.

[70] R. G. Dickinson, L. Pauling, The crystal structure of molybdenite, J. Am. Chem. Soc. 45(6) (1923) 1466–1471.

[71] J. Wilson, A. Yoffe, The transition metal dichalcogenides discussion and interpretation of the observed optical, electrical and structural properties, Adv. Phys. 18 (73) (1969) 193–335.

[72] M. V. Hove, S. Tong, M. Elconin, Surface structure refinements of $2H-MoS_2$, $2H-NbSe_2$ and $W(100)p(2\times1)-O$ via new reliability factors for surface crystallography, Surf. Sci. 64 (1977) 85–95.

[73] Y. Kadowaki, K. Aika, H. Kondoh, H. Nozoye, Surface structure of $MoS_2(001)$ determined by coaxial impact−collision ion scattering spectroscopy (CAICISS), Surf. Sci. 287 (1993) 396.

[74] W. Jin, P.-C. Yeh, N. Zaki, D. Zhang, J. T. Liou, J. T. Sadowski, A. Barinov, M. Yablonskikh, J. I. Dadap, P. Sutter, I. P. Herman, R. M. Osgood, Substrate interactions with suspended and supported monolayer MoS_2: Angle−resolved photoemission spectroscopy, Phys. Rev. B 91 (2015) 121409.

[75] W. Jin, P.-C. Yeh, N. Zaki, D. Zhang, J. T. Sadowski, A. Al-Mahboob, A. M. van der Zande, D. A. Chenet, J. I. Dadap, I. P. Herman, P. Sutter, J. Hone, R. M. Osgood, Direct measurement of the thickness−dependent electronic band structure of MoS_2 using angle−resolved photoemission spectroscopy, Phys. Rev. Lett. 111 (2013) 106801.

[76] L. Britnell, R. V. Gorbachev, R. Jalil, B. D. Belle, F. Schedin, A. Mishchenko, T. Georgiou, M. I. Katsnelson, L. Eaves, S. V. Morozov, N. M. R. Peres, J. Leist, A. K. Geim, K. S. Novoselov, L. A. Ponomarenko, Field−effect tunneling transistor based on vertical graphene heterostructures, Science 24 (2012) 947–950.

[77] K. F. Mak, C. Lee, J. Hone, J. Shan, T. F. Heinz, Atomically thin MoS_2: A new direct−gap semiconductor, Phys. Rev. Lett. 105 (2010) 136805.

[78] Z. Yin, H. Li, H. Li, L. Jiang, Y. Shi, Y. Sun, G. Lu, Q. Zhang, X. Chen, H. Zhang, Single−layer MoS_2 phototransistors, ACS Nano 6(1) (2012) 74–80.

[79] P.-C. Yeh, W. Jin, N. Zaki, D. Zhang, J. T. Sadowski, A. Al-Mahboob, A. M. van der Zande, D. A. Chenet, J. I. Dadap, I. P. Herman, P. Sutter, J. Hone, R. M. Osgood, Probing substrate-dependent long-range surface structure of single-layer and multilayer MoS_2 by low−energy electron microscopy and microprobe diffraction, Phys. Rev. B 89 (2014) 155408.

[80] C. Lee, H. Yan, L. E. Brus, T. F. Heinz, J. Hone, S. Ryu, Anomalous lattice vibrations of single− and few−layer MoS_2, ACS Nano 4 (2010) 2695.

[81] A. Splendiani, L. Sun, Y. Zhang, T. Li, J. Kim, C.-Y. Chim, G. Galli, F. Wang, Emerging photoluminescence in monolayer MoS_2, Nano Lett. 10 (2010) 1271.

[82] M. Ishigami, J. H. Chen, W. G. Cullen, M. S. Fuhrer, E. D. Williams, Atomic structure of graphene on SiO_2, Nano Lett. 7 (2007) 1643.

[83] K. R. Knox, S. Wang, A. Morgante, D. Cvetko, A. Locatelli, T. O. Mentes, M. A. Nio, P. Kim, J. R. M. Osgood, Spectromicroscopy of single and multilayer graphene supported by a weakly interacting substrate, Phys. Rev. B 78 (2008) 201408.

[84] D. L. Adams, A simple and effective procedure for the refinement of surface structure in leed, Surf. Sci. 519 (2002) 157–172.

[85] J. Su, Z.-T. Liu, L.-P. Feng, N. Li, Effect of temperature on thermal properties of monolayer MoS_2 sheet, J. Alloys Compd. 622 (2015) 777–782.

[86] N. Wakabayashi, H. G. Smith, R. M. Nicklow, Lattice dynamics of hexagonal MoS_2 studied by neutron scattering, Phys. Rev. B 12 (1975) 659.

[87] S. H. El-Mahalawy, B. L. Evans, The thermal expansion of 2H−MoS_2, 2H−$MoSe_2$ and 2H−WSe_2 between 20 and 800°C, J. Appl. Cryst. 9 (1976) 403.

[88] R. Murray, B. L. Evans, The thermal expansion of 2H−MoS_2 and 2H−WSe_2 between 10 and 320 K, J. Appl. Cryst. 12 (1979) 312.

[89] X. Ling, H. Wang, S. Huang, F. Xia, M. S. Dresselhaus, The renaissance of black phosphorus, Proc. Natl. Acad. Sci. USA 12 (2015) 4523.

[90] C. Q. Han, M. Y. Yao, X. X. Bai, L. Miao, F. Zhu, D. D. Guan, S. Wang, C. L. Gao, C. Liu, D. Qian, Y. Liu, J.-F. Jia, Electronic structure of black phosphorus studied by angle−resolved photoemission spectroscopy, Phys. Rev. B 90 (2014) 085101.

[91] A. Carvalho, M. Wang, X. Zhu, A. S. Rodin, H. Su, A. H. C. Neto, Phosphorene: from theory to applications, Nat. Rev. Mater. 1 (2016) 16061.

[92] A. Morita, Semiconducting black phosphorus, Appl. Phys. A 39 (1986) 227.

[93] C. D. Zhang, J. C. Lian, W. Yi, Y. H. Jiang, L. W. Liu, H. Hu, W. D. Xiao, S. X. Du, L. L. Sun, H. J. Gao, Surface structures of black phosphorus investigated with scanning tunneling microscopy, J. Phys. Chem. C 113 (2014) 18823.

[94] L. Liang, J. Wang, W. Lin, B. G. Sumpter, V. Meunier, M. Pan, Electronic bandgap and edge reconstruction in phosphorene materials, Nano Lett. 14 (2014) 6400.

[95] J. de la Figuera, J. Puerta, J. Cerda, F. E. Gabaly, K. McCarty, Determining the structure of Ru(0001) from low−energy electron diffraction of a single terrace, Surf. Sci. 600 (2006) L105.

[96] J. B. Hannon, J. Sun, K. Pohl, G. L. Kellogg, Origins of nanoscale heterogeneity in ultrathin films, Phys. Rev. Lett. 96 (2006) 246103.

[97] Y. Akahama, S. Endo, S. Narita, Electrical properties of black phosphorus single crystals, J. Phys. Soc. Jpn. 52 (1983) 2148.

[98] W. Jin, P.-C. Yeh, N. Zaki, D. Zhang, J. T. Liou, J. T. Sadowski, A. Barinov, M. Yablonskikh, J. I. Dadap, P. Sutter, I. P. Hermanand, R. M. Osgood, Jr, Substrate interactions with suspended and supported monolayer MoS_2: angle−resolved photoemission spectroscopy, Phys. Rev. B 91 (2015) 121409.

[99] C. Kaneta, H. Katayama-Yoshida, A. Morita, Lattice dynamics of black phosphorus, Solid State Commun. 44 (5) (1982) 613.

[100] S. Cahangirov, M. Topsakal, E. Aktürk, H. Şahin, S. Ciraci, Two- and one-dimensional honeycomb structures of silicon and germanium, Phys. Rev. Lett. 102 (2009) 236804.

[101] J. T. Sadowski, T. Nagao, S. Yaginuma, Y. Fujikawa, T. Sakurai, Stability of the quasicubic phase in the initial stage of the growth of bismuth films on Si(111)-7×7, J. Appl. Phys. 99 (2006) 014904.

[102] T. Nagao, J. T. Sadowski, M. Saito, S. Yaginuma, Y. Fujikawa, T. Kogure, T. Ohno, Y. Hasegawa, S. Hasegawa, T. Sakurai, Nanofilm allotrope and phase transformation of ultrathin bi film on Si(111)-7×7, Phys. Rev. Lett. 93 (2004) 105501.

[103] P. E. Blöchl, Projector augmented−wave method, Phys. Rev. B 50 (1994) 17953.

[104] G. Kresse, J. Furthm*ü*ller, Efficiency of ab−initio total energy calculations for metals and semiconductors using a plane−wave basis set, Comput. Mater. Sci. 6 (1996) 15.

[105] G. Kresse, J. Furthm*ü*ller, Efficient iterative schemes for *ab initio* total-energy calculations using a plane-wave basis set, Phys. Rev. B 54 (1996) 11169.

[106] G. Kresse, D. Joubert, From ultrasoft pseudopotentials to the projector augmented−wave method, Phys. Rev. B 59 (1999) 1758.

[107] J. P. Perdew, K. Burke, M. Ernzerhof, Generalized gradient approximation made simple, Phys. Rev. Lett. 77 (1996) 3865.

[108] A. Tkatchenko, M. Scheffler, Accurate molecular van der waals interactions from ground−state electron density and free−atom reference data, Phys. Rev. Lett. 102 (2009) 073005.

[109] J. Heyd, G. E. Scuseria, M. Ernzerhof, Hybrid functionals based on a screened coulomb potential, J. Chem. Phys. 118 (2003) 8207.

[110] J. Heyd, G. E. Scuseria, M. Ernzerhof, Erratum: 'Hybrid functionals based on a screened Coulomb potential' [J. Chem. Phys. 118, 8207 (2003)], J. Chem. Phys. 124 (2006) 219906.

[111] J. V. Riffle, C. Flynn, B. S. Laurent, C. A. Ayotte, C. A. Caputo, S. M. Hollen, Impact of vacancies on electronic properties of black phosphorus probed by STM, J. Appl. Phys. 123 (2018) 044301.

[112] T. Osada, Edge state and intrinsic hole doping in bilayer phosphorene, J. Phys. Soc. Jpn. 84 (2015) 013703.

[113] B. Kiraly, N. Hauptmann, A. N. Rudenko, M. I. Katsnelson, A. A. Khajetoorians, Probing single vacancies in black phosphorus at the atomic level, Nano Lett. 17 (2017) 3607.

[114] A. Surrente, A. A. Mitioglu, K. Galkowski, W. Tabis, D. K. Maude, P. Plochocka, Excitons in atomically thin black phosphorus, Phys. Rev. B 93 (2016) 121405.

[115] D. Warschauer, Electrical and optical properties of crystalline black phosphorus, J. Appl. Phys. 34 (1963) 1853.

[116] M. Baba, Y. Nakamura, K. Shibata, A. Morita, Photoconduction of black phosphorus in the infrared region, Jpn. J. Appl. Phys. 30 (1991) L1178.

[117] R. Yan, S. Fathipour, Y. Han, B. Song, S. Xiao, M. Li, N. Ma, V. Protasenko, D. A. Muller, D. Jena, H. G. Xing, Esaki diodes in van der Waals heterojunctions with broken-gap energy band alignment, Nano Lett. 15 (2015) 5791.

[118] T. Roy, M. Tosun, M. Hettick, G. H. Ahn, C. Hu, A. Javey, 2D-2D tunneling field-effect transistors using $WSe_2/SnSe_2$ heterostructures, Appl. Phys. Lett. 108 (2016) 083111.

[119] M. O. Li, D. Esseni, J. J. Nahas, D. Jena, H. G. Xing, Two-dimensional heterojunction interlayer tunneling field effect transistors (Thin-TFETs), IEEE J. Electron Devices Soc. 3 (2015) 200–207.

[120] Y. Huang, C. Ling, H. Liu, S. Wang, B. Geng, Versatile electronic and magnetic properties of $SnSe_2$ nanostructures induced by the strain, J. Phys. Chem. C 118 (2014) 9251.

[121] L.-D. Zhao, S.-H. Lo, Y. Zhang, H. Sun, G. Tan, C. Uher, C. Wolverton, V. P. Dravid, M. G. Kanatzidis, Ultralow thermal conductivity and high thermoelectric figure of merit in SnSe crystals, Nature 508 (2014) 373.

[122] Z. Wang, J. Wang, Y. Zang, Q. Zhang, J.-A. Shi, T. Jiang, Y. Gong, C.-L. Song, S.-H, Ji, L.-L. Wang, L. Gu, K. He, W. Duan, X. Ma, X. Chen, Q.-K. Xue, Molecular beam epitaxygrown snse in the rocksalt structure: An artificial topological crystalline insulator material, Adv. Mater. 27 (2015) 4150.

[123] X. Zhou, L. Gan, W. Tian, Q. Zhang, S. Jin, H. Li, Y. Bando, D. Golberg, T. Zhai, Ultrathin $SnSe_2$ flakes grown by chemical vapor deposition for highperformance photodetectors, Adv. Mater. 27 (2015) 8035.

[124] S. Vishwanath, X. Liu, S. Rouvimov, L. Basile, N. Lu, A. Azcatl, K. Magno, R. M. Wallace, M. Kim, J.-C. Idrobo, J. K. Furdyna, D. Jena, H. G. Xing, Controllable growth of layered selenide and telluride heterostructures and superlattices using molecular beam epitaxy, J. Mater. Res. 31 (2016) 900.

[125] A. Matetskiy, I. Kibirev, A. Zotov, A. Saranin, Growth and characterization of van der Waals heterostuctures formed by the topological insulator Bi_2Se_3 and the trivial insulator $SnSe_2$, Appl. Phys. Lett. 109 (2016) 021606.

[126] M. Zhao, M. Liu, Y. Dong, C. Zou, K. Yang, Y. Yang, L. Zhang, S. Huang, Epitaxial growth of two-dimensional $SnSe_2/MoS_2$ misfit heterostructures, J. Mater. Chem. C 4 (2016) 10215.

[127] K.-M. Chung, D.Wamwangi, M.Woda, M.Wuttig, W. Bensch, $SnSe_2$ field-effect transistors with high drive current, J. Appl. Phys. 103 (2008) 083523.

[128] Y. Wang, L. Huang, B. Li, J. Shang, C. Xia, C. Fan, H.-X. Deng, Z. Wei, J. Li, Composition-tunable 2D $SnSe_{2(1x)}S_{2x}$ alloys towards efficient bandgap engineering and high performance (opto)electronics, J. Mater. Chem. C 5 (2017) 84–90.

[129] S. Dong, X. Liu, X. Li, V. Kanzyuba, T. Yoo, S. Rouvimov, S. Vishwanath, H. G. Xing, D. Jena, M. Dobrowolska, J. K. Furdyna, Room temperature weak ferromagnetism in $Sn_{1x}Mn_xSe_2$ 2D films grown by molecular beam epitaxy, Appl. Phys. Lett. Mater. 4 (2016) 032601.

[130] R. Schlaf, D. Louder, O. Lang, C. Pettenkofer, W. Jaegermann, K. Nebesny, P. Lee, B. Parkinson, N. R. Armstrong, Molecular beam epitaxy growth of thin films of SnS_2 and $SnSe_2$ on cleaved mica and the basal planes of singlecrystal layered semiconductors: Reflection highenergy electron diffraction, lowenergy electron diffraction, photoemission, and scanning tunneling microscopy/atomic force microscopy characterization, J. Vac. Sci. Technol. A 13 (1995) 1761.

[131] R. Schlaf, N. R. Armstrong, B. Parkinson, C. Pettenkofer, W. Jaegermann, Van der Waals epitaxy of the layered semiconductors $SnSe_2$ and SnS_2: morphology and growth modes, Surf. Sci. 385 (1997) 1–14.

[132] Y. W. Park, S.-K. Jerng, J. H. Jeon, S. B. Roy, K. Akbar, J. Kim, Y. Sim, M.-J. Seong, J. H. Kim, Z. Lee, M. Kim, Y. Yi, J. Kim, D. Y. Noh, S.-H. Chun, Molecular beam epitaxy of large-area $SnSe_2$ with monolayer thickness fluctuation, 2D Mater. 4 (2016) 014006.

[133] K. E. Aretouli, D. Tsoutsou, P. Tsipas, J. Marquez-Velasco, S. A. Giamini, N. Kelaidis, V. Psycharis, A. Dimoulas, Epitaxial 2D $SnSe_2$/ 2D WSe_2 van der waals heterostructures, ACS Appl. Mater. Interfaces 8 (2016) 23222.

[134] R. Schlaf, O. Lang, C. Pettenkofer, W. Jaegermann, Band lineup of layered semiconductor heterointerfaces prepared by van der Waals epitaxy: Charge transfer correction term for the electron affinity rule, J. Appl. Phys. 85 (1999) 2732.

[135] V. Kanzyuba, S. Dong, X. Liu, X. Li, S. Rouvimov, H. Okuno, H. Mariette, X. Zhang, S. Ptasinska, B. D. Tracy, D. J. Smith, M. Dobrowolska, J. K. Furdyna, Structural evolution of dilute magnetic (Sn,Mn)Se films grown by molecular beam epitaxy, J. Appl. Phys. 121 (2017) 075301.

[136] S. Vishwanath, Epitaxy of layered materials and their heterostructures, Ph.D Thesis, Cornell University, 2017.

[137] X. Wang, T.-C. Chiang, Topological states in Bi_2Se_3 surfaces created by cleavage within a quintuple layer: Analysis in terms of the shockley criterion, Phys. Rev. B 89 (2014) 125109.

[138] Y. Shi, M. Wu, F. Zhang, J. Feng, (111) surface states of SnTe, Phys. Rev. B 90 (2014) 235114.

[139] Y. Tanaka, T. Shoman, K. Nakayama, S. Souma, T. Sato, T. Takahashi, M. Novak, K. Segawa, Y. Ando, Two types of Dirac-cone surface states on the (111) surface of the topological crystalline insulator SnTe, Phys. Rev. B 88 (2013) 235126.

[140] P. Tasker, The stability of ionic crystal surfaces, J. Phys. C 12 (1979) 4977.

[141] C. Noguera, Polar oxide surfaces, J. Phys. Condens. Matter 12 (2000) R367.

[142] C. Yan, J. Liu, Y. Zang, J. Wang, Z. Wang, P. Wang, Z.-D. Zhang, L. Wang, X. Ma, S. Ji, K. He, L. Fu, W. Duan, Q.-K. Xue, X. Chen, Experimental observation of Dirac-like surface states and topological phase transition in $Pb_{1-x}Sn_xTe(111)$ films, Phys. Rev. Lett. 112 (2014) 186801.

[143] J. Wang, J. Liu, Y. Xu, J. Wu, B.-L. Gu, W. Duan, Structural stability and topological surface states of the SnTe(111) surface, Phys. Rev. B 89 (2014) 125308.

[144] E. Sutter, Y. Huang, H. P. Komsa, M. Ghorbani-Asl, A. V. Krasheninnikov, P. Sutter, Electron−beam induced transformations of layered tin dichalcogenides, Nano Lett. 16 (2016) 4410.

[145] Z. Borges, C. Poffo, J. de Lima, S. de souza, D. Trichês, T. Nogueira, L. Manzato, R. de Biasi, Study of structural, optical and thermal properties of nanostructured $SnSe_2$ prepared by mechanical alloying, Mater. Chem. Phys. 169 (2016) 47.

[146] H. Wiedemeier, G. Pultz, U. Gaur, B. Wunderlich, Heat capacity measurements of SnSe and $SnSe_2$, Thermochim. Acta 43 (1981) 297.

[147] K. Zhang, C. Bao, Q. Gu, X. Ren, H. Zhang, K. Deng, Y. Wu, Y. Li, J. Feng, S. Zhou, Raman signatures of inversion symmetry breaking and structural phase transition in type-II Weyl semimetal $MoTe_2$, Nat. Commun. 7 (2016) 13552.

[148] M. N. Ali, J. Xiong, S. Flynn, J. Tao, Q. D. Gibson, L. M. Schoop, T. Liang, N. Haldolaarachchige, M. Hirschberger, N. P. Ong, R. J. Cava, Large, non-saturating magnetoresistance in WTe_2, Nature 514 (2014) 205.

[149] L. Thoutam, Y. Wang, Z. Xiao, S. Das, A. Luican-Mayer, R. Divan, G. Crabtree, W. Kwok, Temperature-dependent three-dimensional anisotropy of the magnetoresistance in WTe_2, Phys. Rev. Lett. 115 (2015) 046602.

[150] S.-Y. Xu, I. Belopolski, N. Alidoust, M. Neupane, G. Bian, C. Zhang, R. Sankar, G. Chang, Z. Yuan, C.-C. Lee, Discovery of a Weyl fermion semimetal and topological Fermi arcs, Science 349 (2015) 613.

[151] L. Yang, Z. Liu, Y. Sun, H. Peng, H. Yang, T. Zhang, B. Zhou, Y. Zhang, Y. Guo, M. Rahn, Weyl semimetal phase in the non-centrosymmetric compound TaAs, Nat. Phys. 11 (2015) 728.

[152] A. A. Soluyanov, D. Gresch, Z. Wang, Q. Wu, M. Troyer, X. Dai, B. A. Bernevig, Type-II Weyl semimetals, Nature 527 (2015) 495.

[153] B. E. Brown, The crystal structures of WTe_2 and high-temperature $MoTe_2$, Acta. Cryst. 20 (1966) 268.

[154] Y. Sun, S.-C. Wu, M. N. Ali, C. Felser, B. Yan, Prediction of Weyl semimetal in orthorhombic $MoTe_2$, Phys. Rev. B 92 (2015) 161107.

[155] K. Deng, G. Wan, P. Deng, K. Zhang, S. Ding, E. Wang, M. Yan, H. Huang, H. Zhang, Z. Xu, J. Denlinger, A. Fedorov, H. Yang, W. Duan, H. Yao, Y. Wu, S. Fan, H. Zhang, X. Chen, S. Zhou, Experimental observation of topological Fermi arcs in type-II Weyl semimetal $MoTe_2$, Nat. Phys. 12 (2016) 1105.